OXYGEN ION CONDUCTION IN LAYERED INTERGROWTH

STRUCTURES WITH INTRINSIC OXYGEN VACANCIES

by

JULIE K. THOMAS

B.A., Carleton College, Northfield, Minnesota
(1988)

SUBMITTED TO THE DEPARTMENT OF CHEMISTRY
IN PARTIAL FULFILLMENT OF THE REQUIREMENTS
FOR THE DEGREE OF DOCTOR OF PHILOSOPHY

at the

MASSACHUSETTS INSTITUTE OF TECHNOLOGY
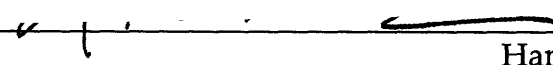
September 1994

Signature of Author _____

Department of Chemistry
June 22, 1994

Certified by _____

Hans-Conrad zur Loye
Thesis Supervisor

Accepted by _____

Dietmar Seyferth
Chairman, Departmental Committee on Graduate Students

This doctoral thesis has been examined by a Committee of the Department of Chemistry as follows:

Professor Dietmar Seyferth
_____
Chairman

Professor Hans-Conrad zur Loye
_____
Thesis Supervisor

Professor Andrew Barron
_____

Acknowledgements

I would like to thank my advisor, Hanno zur Loye, for supporting my research with funding and ideas, and for giving me the opportunity to build and fix things. I would like to thank Uli Wildgruber and Dave Cox at Brookhaven for help with neutron data collection. I would also like to thank everyone who helped me along the way. I would like to thank my high school chemistry teacher, Don Murphy, for getting me interested in chemistry. I would like to thank all of my professors at Carleton for keeping it interesting, but especially Dick Ramette and Jim Finholt for showing me how much fun they had with chemistry. I would like to thank AT&T Bell Laboratories for some financial support and the opportunity to meet a lot of very supportive people. I especially thank Lynn Schneemeyer for continued support and encouragement. I would like to thank all of the members of the zur Loye group for support and suggestions, and, perhaps more importantly, for the endless hours of amusement.

I would also like to thank my family for all of their support. I thank Will for always being there for me: getting me up in the morning, cooking my dinner way too many times, and waiting for me to get home.

To Will,
for all your support:
past, present, and future

OXYGEN ION CONDUCTION IN LAYERED INTERGROWTH STRUCTURES WITH INTRINSIC OXYGEN VACANCIES

by

Julie K. Thomas

Submitted to the Department of Chemistry on June 22, 1994

in partial fulfillment of the requirements

for the Degree of Doctor of Philosophy in Chemistry

ABSTRACT
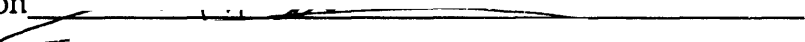
The preparation of new oxygen ion conductors through the use of layered intergrowth structures has been investigated. An oxygen-deficient, brownmillerite-like material ($AMO_{2.5}$, A = Sr or Ba, M = Sc, In, or Ga) was always used as one component to provide the vacancies necessary for oxygen ion conduction. The other component was either a perovskite material ($AM'O_3$, A = Sr or Ba, M' = Ti, Zr, or Hf) or the Aurivillius phase, $Bi_4Ti_3O_{12}$. All samples were characterized by powder X-ray diffraction for structural determination and ac impedance measurements for determination of the oxygen ion conductivity.

The brownmillerite-perovskite intergrowths, $(AMO_{2.5})_x(AM'O_3)_y$, showed moderate oxygen ion conductivity, with the best samples ($Ba_3In_2TiO_8$ and $Ba_3In_2HfO_8$) having conductivities of 10^{-3} S cm^{-1} at 900 °C. These materials generally did not show an ordered structure, but rather the cubic perovskite structure with disordered oxygen vacancies. Many of these materials exhibit non-linear behavior in Arrhenius plots of conductivity, and this is most

likely due to protonic conduction at low temperatures. High temperature powder X-ray diffraction on $Ba_3In_2TiO_8$ showed only an increase in the lattice parameters with temperature with no change in symmetry. The high temperature conductivities were found to correlate well with free volume in the lattice, while the activation energies were primarily dependent on the elements used, regardless of the ratio between brownmillerite and perovskite units.

The Aurivillius-brownmillerite intergrowths, $(Bi_4Ti_3O_{12})_x(BaMO_{2.5})_y$, exhibited high oxygen ion conductivity ($\sim 1 \times 10^{-1}$ S cm^{-1} at 900 °C) above an order-disorder transition. The order-disorder transitions, as observed in DTA measurements, occurred between 700 and 800 °C. Conductivity jumps of nearly three orders of magnitude were observed at temperatures corresponding to the transitions identified by DTA measurements. These materials have sufficient conductivities to merit further studies and device testing.

Thesis Supervisor: Dr. Hans-Conrad zur Loye
Title: Paul Cook Career Development Professor of Chemistry

TABLE OF CONTENTS

List of Figures

Chapter 2

Chapter 3

Chapter 4

List of Tables

List of Abbreviations

1 eV	96485 J/mole
1 S/cm	100 S/m
Ea	activation energy
SOFC	Solid oxide fuel cell
YSZ	Yttria-stabilized zirconia ($Y_{0.1}Zr_{0.9}O_{0.95}$)
DTA	differential thermal analysis
TGA	thermogravimetric analysis

Chapter 1
Introduction

1. INTRODUCTION

Oxygen ion conductors have been widely studied for applications as components in fuel cells, oxygen sensors, and oxygen membrane catalysts.[1] To achieve the relatively high oxygen fluxes required,[1] most of these systems must be operated at high temperatures. Solid oxide fuel cells (SOFCs) based on yttria-stabilized zirconia (YSZ), for instance, must be operated near 1000 °C.[2,3] There are many problems associated with such high temperatures, including high cost, electrode incompatibility, and ultimately, degradation of the electrolyte itself. It is, therefore, desirable to develop new materials with high oxygen ion conductivities (10^{-2} - 10^{-1} S cm^{-1}) at lower temperatures (600 - 800 °C).[4,5] To design such a material, however, we must first determine how oxygen ion conductivity is affected by various factors, such as structure, vacancy concentration, and free volume. Some previous attempts have been made to predict new materials;[5,6] however, these predictions apply only to a small class of materials, so it is useful to explore other classes of materials. The purpose of this thesis is to explore such factors in a new series of materials with intrinsic vacancies.

Traditionally, the study of materials with intrinsic vacancies has been limited because few are known. It has also been difficult to modify these materials to improve upon the base conductivity. This thesis demonstrates a new method for designing materials with intrinsic vacancies, namely the incorporation of a material with intrinsic vacancies as a component of an intergrowth structure. In this case, all oxygen deficient units are based on the brownmillerite structure and variants ($A_2M_2O_5$, A = Ca, Sr, Ba; M = Ga, Sc, In). The other components in the intergrowth structure are either perovskite based materials ($AM'O_3$, A = Ca, Sr, Ba; M = Ti, Zr, Hf) or Aurivillius phases

(layered bismuth oxides, $Bi_2A_{n-1}M_nO_{3n+3}$, specifically, $Bi_4Ti_3O_{12}$). The intergrowths are of the form $(AMO_{2.5})_x(AM'O_3)_y$ or $(AMO_{2.5})_x(Bi_4Ti_3O_{12})_y$. By using the intergrowth approach we have control over the number of oxygen vacancies in the structure. Other parameters such as structure and free volume may also be affected by the intergrowths.

Brownmillerite structure materials were chosen as the source of vacancies since several have recently been studied for oxygen ion conductivity,[1,7-11] and brownmillerite-perovskite intergrowths have been successfully prepared previously.[8,12-14] Intergrowths between brownmillerite and Aurivillius phases were previously unknown, but Aurivillius-perovskite intergrowths are common,[15-17] and the brownmillerite and perovskite structures are very similar.[18] Additionally, Aurivillius phases such as Bi_2WO_6 and $Bi_4V_2O_{11}$ are known to have very high oxygen ion conductivity.[19,20] The elements within the components were chosen to minimize electrical conductivity. All elements other than bismuth are in their highest oxidation state, and elements with multiple easily accessible oxidation states were generally avoided.

Experimentally the primary focus of this thesis is the synthesis of a new series of materials and the measurement of their ionic conductivity by ac impedance spectroscopy. The materials were structurally characterized by powder X-ray diffraction and some by powder neutron diffraction. Simultaneous differential thermal analysis and thermogravimetric analysis (DTA-TGA) were used to find phase transitions and to determine if there was any weight loss in the samples during heating. Conductivity measurements were taken as a function of temperature to obtain activation energies for all samples. The conductivities of some samples were measured under different

atmospheres to determine carrier types.   The conductivity results are

correlated to vacancy concentrations, compositions, and lattice parameters.

References

(1)   Steele, B. C. H., Oxygen Ion Conductors and Their Technological
        Applications, **Mater. Sci. Eng. B-Solid State M.** (1992) **13**, 79-87.

(2)   Kontoulis, I.; Ftikos, C. P.; Steele, B. C. H., Oxygen Ion Conductivity in
        $Ba_3In_{3-x}Zr_xO_{7.5+x/2}$ (x = 0.7 - 1.3), **Mater. Sci. Eng. B-Solid State M.** (1994)
        22, 313-316.

(3)   Kudo, T.; Fueki, K., *Solid State Ionics*; VCH: New York, NY, 1990.

(4)   Kilner, J. A.; Brook, R. J., A Study of Oxygen Ion Conductivity in Doped
        Non-stoichiometric Oxides, **Solid State Ionics** (1982) **6**, 237-252.

(5)   Sammells, A. F.; Cook, R. L.; White, J. H.; Osborne, J. J.; MacDuff, R. C.,
        Rational Selection of Advanced Solid Electrolytes for Intermediate
        Temperature Fuel Cells, **Solid State Ionics** (1992) **52**, 111-123.

(6)   Cook, R. L.; Sammells, A. F., On the Systematic Selection of Perovskite
        Solid Electrolytes for Intermediate Temperature Fuel Cells, **Solid State
        Ionics** (1991) **45**, 311-321.

(7)   Adler, S. B.; Reimer, J. A.; Baltisberger, J.; Werner, U., Chemical
        Structure and Oxygen Dynamics in $Ba_2In_2O_5$, **J. Am. Chem. Soc.** (1994)
        116, 675-681.

(8)   Goodenough, J. B.; Ruiz-Diaz, J. E.; Zhen, Y. S., Oxide-ion conduction in
        $Ba_2In_2O_5$ and $Ba_3In_2MO_8$ (M = Ce, Hf, or Zr), **Solid State Ionics** (1990) **44**,
        21-31.

(9)   Kontoulis, I.; Steele, B. C. H., Fabrication and Conductivity of a New
        Compound Calcium Chromium Oxide ($Ca_2Cr_2O_5$), **J. Eur. Ceram.
        Mater.** (1992) **9**, 459-62.

(10)   Schwartz, M.; Link, B. F.; Sammells, A. F., New Brownmillerite Solid
        Electrolytes, **J. Electrochem. Soc.** (1993) **140**, L62-L63.

(11)   Shin, S.; Yonemura, M.; Ikawa, H., Order-Disorder Transition of $Sr_2Fe_2O_5$ from Brownmillerite to Perovskite Structure at an Elevated Temperature, **Mater. Res. Bull.** (1978) **13**, 1017-1021.

(12)   González-Calbet, J. M.; Vallet-Regí, M.; Alario-Franco, M. A., Structural Intergrowths in the Calcium Lanthanum Ferrites: $Ca_xLa_{1-x}FeO_{3-y}$ (2/3 < x < 1), **Mater. Res. Bull.** (1983) **18**, 285-292.

(13)   Vallet-Regí, M.; Gonzalez-Calbet, J.; Alario-Franco, M. A.; Grenier, J.-C.; Hagenmuller, P., Structural Intergrowths in the $Ca_xLa_{1-x}FeO_{3-x/2}$ System ($O \leq x \leq 1$): An Electron Microscopy Study, **J. Solid State Chem.** (1984) **55**, 251-261.

(14)   Grenier, J.-C.; Ménil, F.; Pouchard, M.; Hagenmuller, P., Caractérisation Physico-Chimique du Ferrite de Calcium et de Lanthane $Ca_2LaFe_3O_8$, **Mater. Res. Bull.** (1977) **12**, 79-86.

(15)   Subbarao, E. C., A Family of Ferroelectric Bismuth Compounds, **J. Phys. Chem. Solids** (1962) **23**, 665-676.

(16)   Subbanna, G. N.; Guru Row, T. N.; Rao, C. N. R., Structure and Dielectric Properties of Recurrent Intergrowth Structures Formed by the Aurivillius Family of Bismuth Oxides of the Formula $Bi_2A_{n-1}B_nO_{3n+3}$, **J. Solid State Chem.** (1990) **86**, 206-211.

(17)   Jacobson, A. J., In *Chemical Physics of Intercalation II*; P. Bernier et. al., Ed.; "Synthesis and Reaction Chemistry of Layered Oxides with Perovskite Related Structures", Plenum: New York, 1993; pp 117-139.

(18)   Colville, A. A.; Geller, S., Crystal Structure of Brownmillerite, Ca_2FeAlO_5, **Acta Crystallogr. B-Struct. Sci.** (1971) **27**, 2311-2315.

(19)   Yanovskii, V. K.; Voronkova, V. I.; Roginskaya, Y. E.; Venevtsev, Y. N., Rapid anion transfer in Bi_2WO_6 crystals, **Soviet Physics and Solid State** (1982) **24**, 1603-1604.

(20)   Mairesse, In *Fast Ion Transport in Solids*; B. Scrosati, Ed.; "Bismuth-based Oxide Conductors: Novel Structural and Electrical Features", Kluwer: The Netherlands, 1993; pp 271-290.

24

Chapter 2
Recent Developments
in
Oxygen Ion Conductivity

2. RECENT DEVELOPMENTS IN OXYGEN ION CONDUCTIVITY

This literature review begins with an overview of oxygen ion conductors to provide a general background. The next section covers the brownmillerite and perovskite materials, beginning with structural descriptions and covering conductivity behavior of brownmillerite and intergrowth compounds. The last section reviews the relevant data on the Aurivillius phases, especially the widely studied $Bi_4V_2O_{11}$.

2.1 Oxygen Ion Conductors: General

Ionic conductors are a class of solids in which one set of ions is mobile. This may occur through several pathways including transport through planes or tunnels, interstitial migration, and vacancy hopping.[1] In oxygen ion conductors, vacancy hopping is the most common transport mechanism, so most studied materials have oxygen vacancies.[2] The most common way to create vacancies is through doping with cations with lower oxidation states, creating extrinsic vacancies. Calcia- and yttria- stabilized zirconias are examples of this, but many other materials including perovskites have also been studied in this manner. Although this method has generally been successful, it has limitations.[3] Other materials, those with intrinsic vacancies, have more sites than atoms, sometimes having crystallographically distinct sites for vacancies. Mobility between these sites and filled sites is then critical to oxygen ion conduction. One limitation in studying intrinsic vacancies is that few such materials are known. It has also been difficult to make modifications that improve on the intrinsic conductivity in these materials. Any successful modifications have tradeoffs. The following examples are

intended to illustrate these points and to provide a basis for comparison with the materials presented in this thesis.

2.1.1 Fluorite Structure Oxides

The fluorite structure oxides are the most widely studied oxygen ion conductors. These include ceria, thoria, and stabilized zirconia. In the fluorite structure, MO_2, each M is surrounded by eight equidistant oxygens and each oxygen is tetrahedrally coordinated.[4] The oxygens are not close-packed, allowing for a relatively large free volume in the lattice, which minimizes the interaction energies involved in moving to a vacant site. Ceria and thoria display the fluorite structure at all temperatures between room temperature and their melting points, while zirconia displays the fluorite structure only on doping, with yttria and calcia being the most common dopants.[1] Although ceria and thoria have the cubic fluorite structure, they also must be doped with aliovalent cations to introduce vacancies. Calcia-doped zirconia, for instance, may be written as $Zr_{1-x}Ca_xO_{2-x}(V_O^{\cdot\cdot})_x$.[5] Without doping, the carrier concentration comes solely from the defect concentration, and, consequently, the conductivity is not particularly high. Although calcia generates more vacancies, yttria may be more widely used due to a wider stability range as a dopant.[1] The conductivity of $Zr_{0.9}Y_{0.1}O_{1.95}$ (YSZ) is 10^{-1} S cm^{-1} at 900 °C.[3] One reason for the high ionic conductivity in the fluorite-type solutions may be the high solubility of the dopant solid solutions. Yttria may be substituted to almost $x = 0.4$.[1]

The conductivities in these materials follow the expected temperature dependence shown in equation 2.1.

$$\sigma T = \sigma_0 \exp\left(\frac{-E_a}{kT}\right) \qquad (2.1)$$

From this formula a plot of $\ln(\sigma T)$ versus $1/T$ should be linear, and the slope is the activation energy (E_a). The ionic conductivity of these solid solutions reaches a peak with small amounts of dopants (about 10 %) and then begins to decrease as shown in Figure 2.1. This is generally attributed to factors such as the formation of a superlattice based on ordering of the vacancies, association between the vacancies and the dopants, and destabilization of the solid solutions at high concentrations.[1,3] The ordering or clustering of defects increases the activation energy:

$$E_a = \Delta H_m + \frac{1}{2}\Delta H_t, \qquad (2.2)$$

where ΔH_m is the enthalpy required for migration through the lattice and ΔH_t is the trapping enthalpy which represents the attraction between the dopant and the vacancy.[6,7] Thus an increase in dopant concentration increases the carrier concentration, but also increases the activation energy. Kilner and Brook[7] have calculated ΔH_m for various structures and found a value of 0.6 eV for the fluorite structure. The experimental activation energy for these materials is around 1 eV, so the trapping energy is a sizable portion of the activation process.[1] Over long periods of time at high temperatures, the conductivity of stabilized zirconias has been observed to decrease. This phenomenon has been attributed to phase separations or clustering.[6]

Although these materials are the most widely studied and are already used in some applications, they show little promise of improvement. Significant problems such as instability and the required high temperatures may ultimately limit their usage.
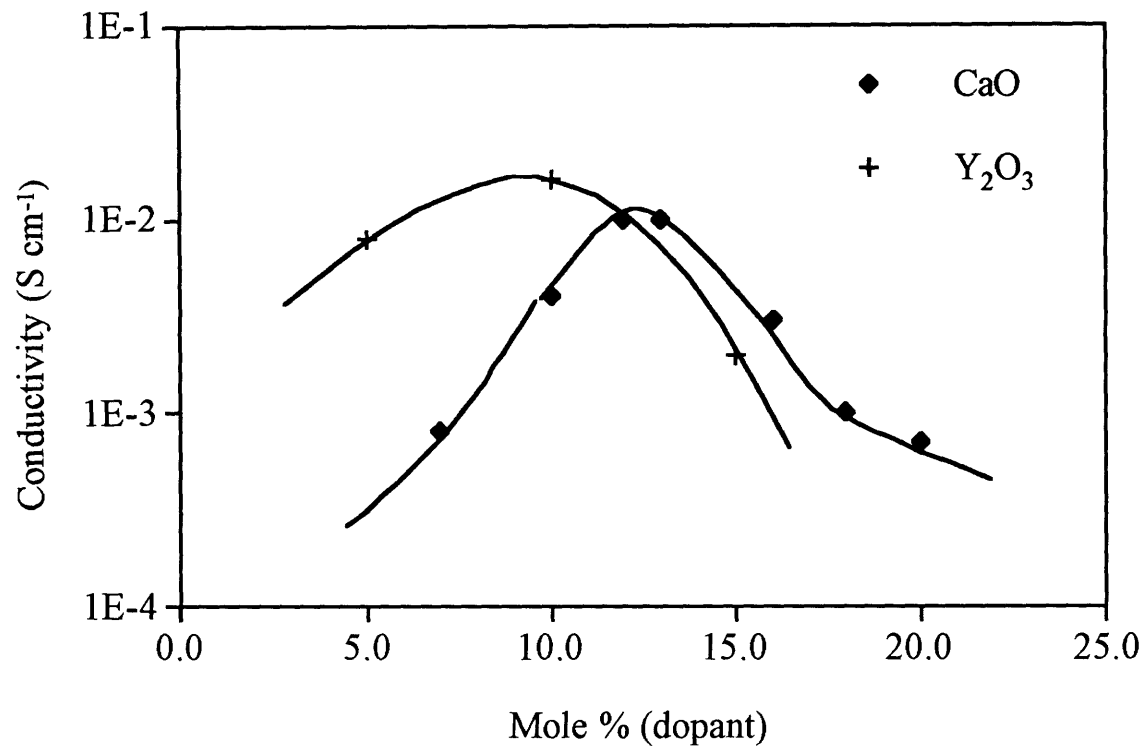
Figure 2.1 Conductivity of stabilized zirconias as a function of dopant concentration (after Kudo[1]).

2.1.2 Doped Perovskites

Other materials which have been studied through doping are perovskites. The perovskite structure has the general formula ABO_3 and can accommodate a range of cations to give a variety of conductivity behaviors, ranging from predominantly electronic ($LaNiO_3$) to ionic ($LaAlO_3$). In general the behavior of these materials is similar to the zirconias, although the conductivity is not as high. The materials are usually doped to create vacancies, resulting in increased activation energies. This becomes especially important in the case of the perovskites, since, as calculated by Kilner and Brook,[7] the intrinsic activation energy for the perovskite structure should be 0.8 ± 0.2 eV, in contrast to 0.6 eV for the fluorite structure. This is due to the smaller opening through which the oxygen ion must pass in the perovskite structure. A number of solid solutions display conductivities of 5×10^{-3} S cm^{-1} at 800 °C, which is sufficient for low conductivity applications (oxygen sensors and some catalysis) but insufficient for high flux applications (fuel cells and some oxygen separation operations).[3]

Sammells and co-workers[8,9] have studied doped perovskites and made some empirical predictions. Their methods were based primarily on ionic radius arguments in order to have a simple database from which to make calculations. They found that systems with high "free volumes", that is more unoccupied space in the lattice, had higher conductivities. Although this might be expected, the opposite trend is observed for the fluorite structure oxides. A high correlation between conductivity and the size of the critical radius (the radius of the smallest area through which the oxygen must pass) was also observed. Using these factors with estimated heats of formation, they were able to predict three previously unstudied materials that are among

the best perovskitic oxygen ion conductors. The best of these materials,

$BaTh_{0.9}Gd_{0.1}O_3$, displayed phase instability in moderate temperature fuel cell

usage.[10] Another doped perovskite which is particularly relevant to materials

in this thesis is Al-doped $CaTiO_3$. Iwahara[11] found that although $CaTiO_3$

displayed electronic conduction at high p_{O_2}, under fuel cell conditions, it is

almost a pure ionic conductor. The conductivity of this material is too low to

be used for low temperature fuel cells, however.

Perovskite materials have exhibited somewhat low oxygen ion

conduction. Without significant improvements, none of these materials is

likely to supplant YSZ as a commercially viable oxygen electrolyte. However,

this series of materials is much larger and more varied than the fluorite based

oxides and has received much less attention. Consequently, although no

ideal materials have been discovered so far, further studies of these materials

could help us to learn about oxygen ion conduction.

2.1.3 Bismuth Oxide

Another material that has been widely studied for its oxygen ion

conductivity is bismuth oxide. In contrast to the fluorite and perovskite

materials, bismuth oxide has intrinsic vacancies. At low temperatures

bismuth oxide exists in its α-phase, which is not highly conductive. At

730 °C, bismuth oxide undergoes a transition to the δ-phase, and displays a

corresponding jump in conductivity of about three orders of magnitude.[12]

An Arrhenius plot of the conductivity of Bi_2O_3 is shown in Figure 2.2. The

structure of δ-Bi_2O_3 is similar to the fluorite structure where one quarter of

the anion sites are vacant: $BiO_{1.5}(V_O)_{0.5}$. Although these sites are ordered, the

polarizability of Bi^{3+} is thought to allow mobility in and out of the vacant

site.[3]
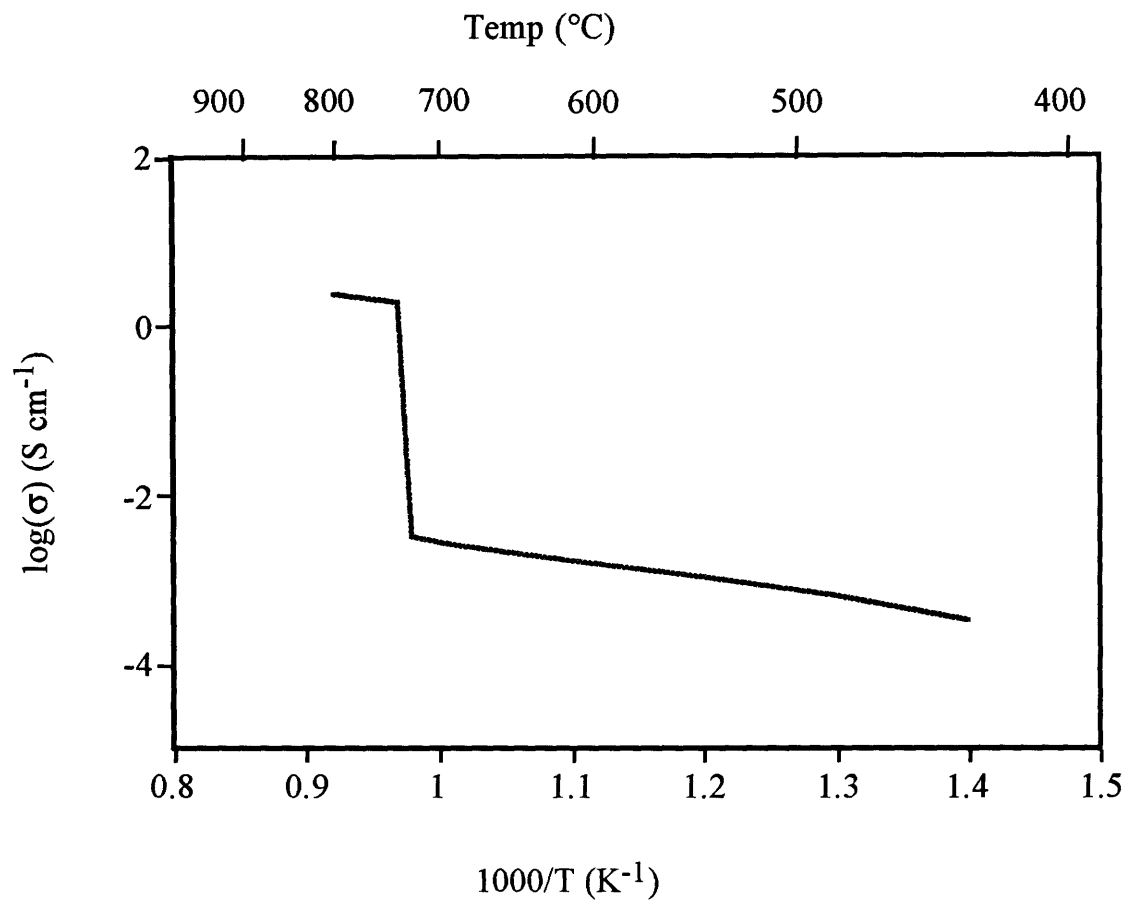
Figure 2.2 Conductivity of Bi_2O_3 as a function of temperature (after Takahashi[12]). The conductivity displays a discontinuity with a large increase in conductivity. The activation energy (proportional to the slope) of the high temperature region is smaller than that of the low temperature region.

One problem with bismuth oxide as an oxygen ion conductor is that the transition to the δ-phase occurs within 100 degrees of the melting point. To avoid this problem, dopants may be used to stabilize the δ-phase to lower temperatures. Using yttria as the dopant, $(Bi_2O_3)_{1-x}(Y_2O_3)_x$, the structure can be stabilized down to room temperature, and for $x = 0.25$ conductivities as high as 1.3×10^{-2} S cm^{-1} have been observed at 500 °C.[12] The conductivity of YSZ at this temperature is only 5×10^{-4} S cm^{-1}.[1] A plot of the conductivities of tungsten-stabilized Bi_2O_3 is shown in Figure 2.3 with pure bismuth oxide and YSZ for comparison. Another problem with bismuth oxide is that it is easily reduced. At oxygen partial pressures near one atmosphere, the transference number of bismuth oxide and most of its solid solutions is close to unity, but as the partial pressure decreases, Bi_2O_3 may be partially reduced and electronic conductivity predominates below 10^{-13} bar.[1]

Although Bi_2O_3 has many limitations, its significant low-temperature conductivity may find some applications in catalysis and other applications not requiring low partial pressures of oxygen.

2.1.4 Conduction through Point Defects

A small number of materials without apparent vacancies are oxygen ion conductors. The materials conduct through point defects in the materials. Such defects are found in all materials. The two most common point defects are Frenkel and Schottky defects.[5] Frenkel defects consist of pairs of cations on interstitial sites and vacant cation sites, represented as follows for a simple MO compound:

$$M_M + V_i \leftrightarrow V_M'' + M_i^{\bullet\bullet}, \tag{2.3}$$

where M_M represents a metal on a metal site, V_i represents a vacancy on an interstitial site, V_M'' represents a vacancy on a metal site with a corresponding
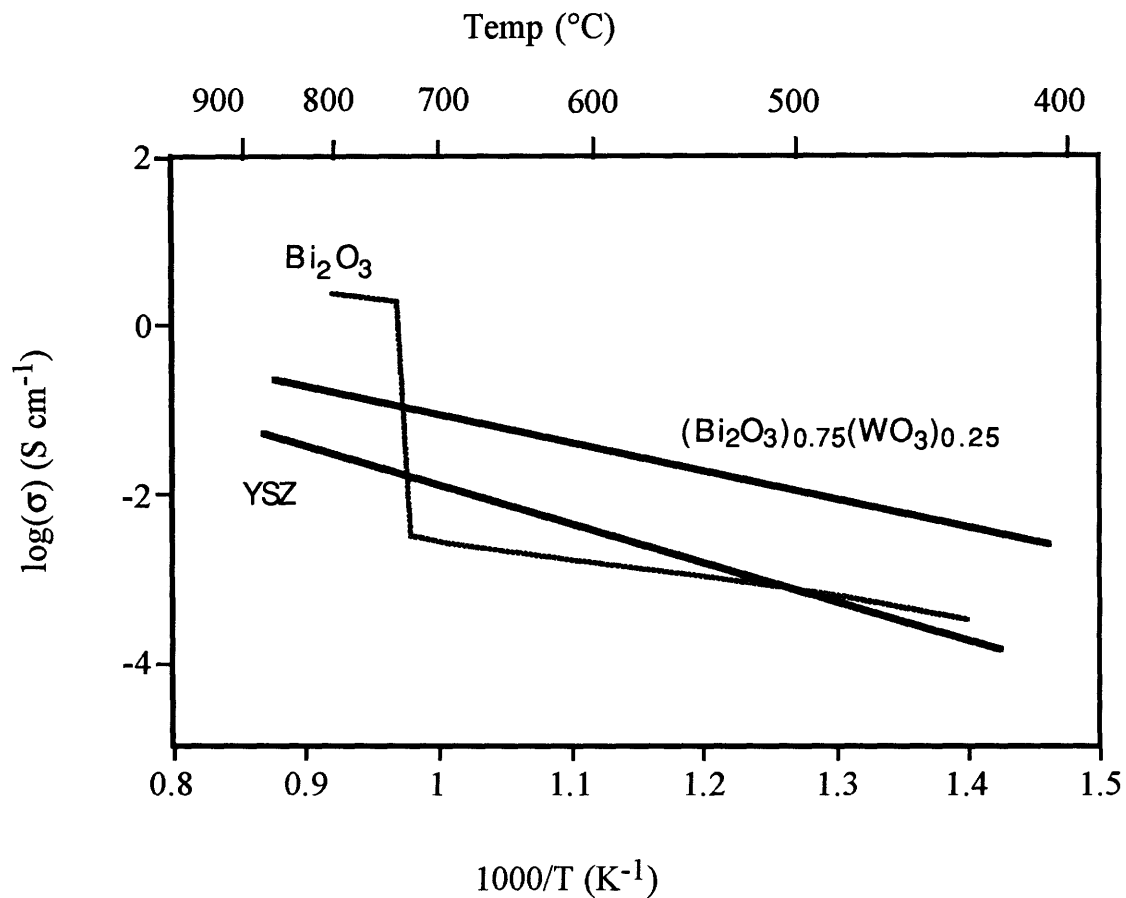
Figure 2.3 Conductivities of Bi_2O_3, stabilized δ-Bi_2O_3, and YSZ as a function of temperature (after Takahashi[12] and Kudo[1]). Although the conductivity of the stabilized δ-Bi_2O_3 is increased relative to pure Bi_2O_3, it is much lower than the extrapolation from the δ-phase of pure Bi_2O_3.

double positive charge, and $M_i^{\bullet\bullet}$ represents a metal on an interstitial site with a double negative charge. An anti-Frenkel defect involves anions:

$$O_O + V_i \leftrightarrow V_O^{\bullet\bullet} + O_i''. \tag{2.4}$$

Schottky defects are pairs of anion and cation vacancies:

$$M_M + O_O \leftrightarrow MO + V_M'' + V_O^{\bullet\bullet}. \tag{2.5}$$

These point defects may contribute to ionic or electronic conductivity depending on the type and number of defects. In order to maintain electroneutrality in the solid, the number of charges, and thus the relative number of defects must balance:

$$2[V_O^{\bullet\bullet}] + 2[M_i^{\bullet\bullet}] + [h^{\bullet}] = 2[V_M''] + 2[O_i''] + [e']. \tag{2.6}$$

This equilibrium is especially important at high oxygen partial pressures where the species may be oxidized:

$$1/2\,O_2 + V_i \leftrightarrow O_i'' + 2h^{\bullet}, \tag{2.7}$$

or at low partial pressures where reduction takes place:

$$O_O \leftrightarrow 1/2\,O_2 + V_O^{\bullet\bullet} + 2e'. \tag{2.8}$$

The simplest combination of these equations gives the expected total conductivity as a sum of electron, hole, and ionic contributions:

$$\log(\sigma) = \log\left[A + B\left(p_{O_2}\right)^{-1/4} + C\left(p_{O_2}\right)^{+1/4} \right], \tag{2.9}$$

where A, B, and C represent the ionic, electronic, and hole contributions, respectively. All three values are generally temperature dependent. Thus at low oxygen partial pressures, n-type conductivity may predominate while p-type conductivity may be possible at higher partial pressures of oxygen. If the electron and hole conductivities or concentrations are small, the ionic conductivity will predominate, and the conductivity will remain constant over a range of oxygen partial pressures. Since both the electronic and hole conductivities are dependent on oxygen concentration, lack of oxygen partial

pressure dependence is an indicator of oxygen ions being the major charge carrier. Slopes of $1/4$ and $-1/4$ indicate p- and n-type conductivities, respectively.

In a similar manner, protonic conduction in oxides can be studied through the reaction of defects with water:

$$H_2O + O_O + V_O^{\bullet\bullet} \leftrightarrow 2OH_O^{\bullet}. \tag{2.10}$$

The $OH_O^{\bullet}$ could also be viewed as $O_O + H_i^{\bullet}$. Thus if protons or hydroxide ions are charge carriers, the conductivity would be expected to change with atmospheric moisture concentrations.

2.2 Brownmillerite and Perovskite Materials

2.2.1 Structures

2.2.1.1 The perovskite structure

The idealized perovskite structure, named for the mineral $CaTiO_3$, is a simple cubic system in space group $Pm\bar{3}m$ with composition ABO_3 having one formula unit per unit cell.[4] Although other oxidation states are possible, all materials covered in this thesis have the oxidation states $A^{2+}B^{4+}O_3$. The structure is shown in Figure 2.4. The B cation is octahedrally coordinated to six oxygens, and these octahedra are corner-shared. The A cation sits in the space between eight octahedra and has twelve nearest-neighbor oxygens. For this simple system, the lattice parameters are about 4 Å. There are many possible distortions to this structure depending on the nature of the A and B cations.[13]
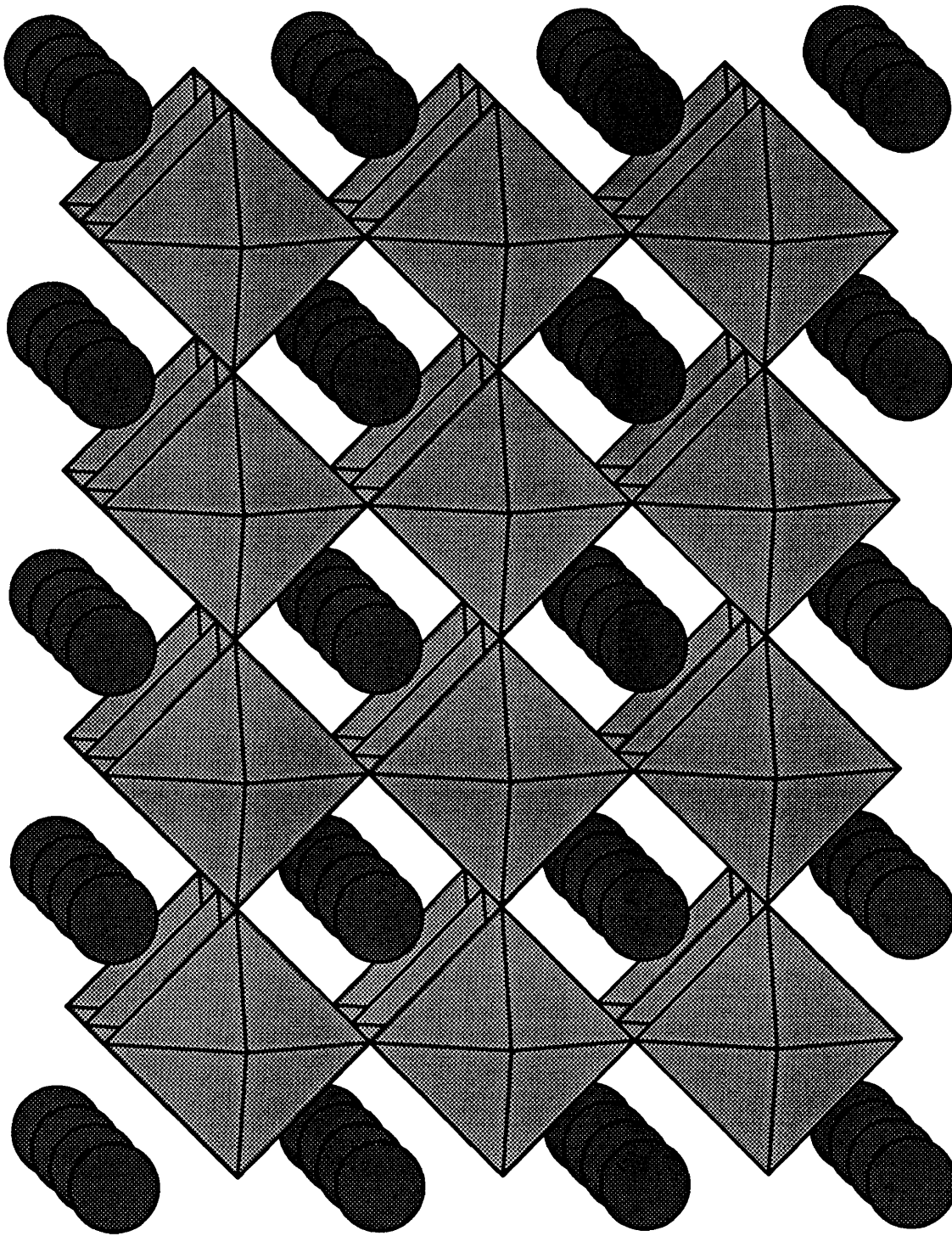
Figure 2.4 The perovskite structure, ABO_3. Dark gray spheres are A, and light gray octahedra are BO_6.

2.2.1.2 The brownmillerite structure

The brownmillerite structure has the composition $A_2MM'O_5$ and is named for the mineral Ca_2FeAlO_5. The idealized brownmillerite structure is orthorhombic in space group Ibm2.[14] If the M and M' cations are identical, the space group is Pcmn.[15] The brownmillerite structure can be viewed as the perovskite structure with oxygen vacancies along the [101] direction in alternate layers. This results in an increased unit cell relative to the perovskite: $a = \sqrt{2}a_p$, $b = 4b_p$, $c = \sqrt{2}c_p$. This structure is shown in Figure 2.5. For comparison a perovskite structure is shown along the [101] direction in Figure 2.6. Other perovskite related structures are possible for the composition $A_2M_2O_5$, including that of $Ca_2Mn_2O_5$.[16] It is also possible that the oxygen vacancies in the structure do not order. This simply gives the perovskite structure with a statistical occupancy of the oxygen sites.

2.2.1.3 Brownmillerite-perovskite intergrowths

All brownmillerite-perovskite intergrowths in this thesis are of the type $(AMO_{2.5})_x(AM'O_3)_y$. Two basic types of intergrowths exist -- ordered and disordered. One possibility is to have disordered or random occupancy of M and M' on the B cation site. In this case the unit cell will consist of only one octahedral unit unless distortions decrease the symmetry. Intergrowths of this type are isostructural to a simple perovskite (Figure 2.4). Ordered intergrowths may be of block or layer type. The previously studied brownmillerite-perovskite intergrowths were layer-type. The $CaTiO_3$-$Ca_2Fe_2O_5$ system has been studied and two ordered intergrowths were found.[17] $Ca_3Fe_2TiO_8$ has the structure shown in Figure 2.6, where there are three perovskite layers in a unit cell. Single crystals of this compound have not
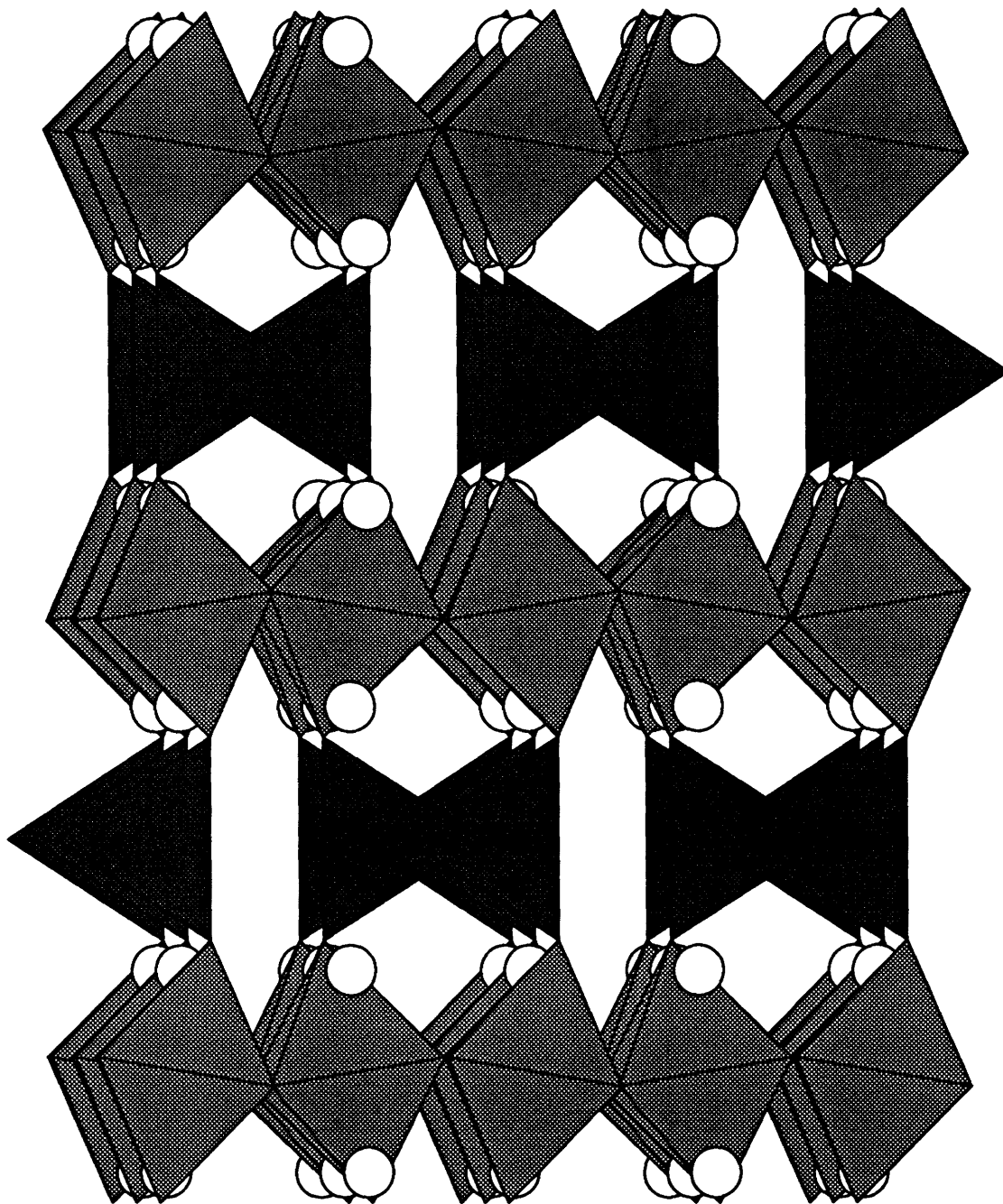
Figure 2.5 The brownmillerite structure, Ca_2FeAlO_5. White spheres are Ca, dark gray represents $(Al,Fe)O_4$ tetrahedra, and light gray $(Fe,Al)O_6$ octahedra.
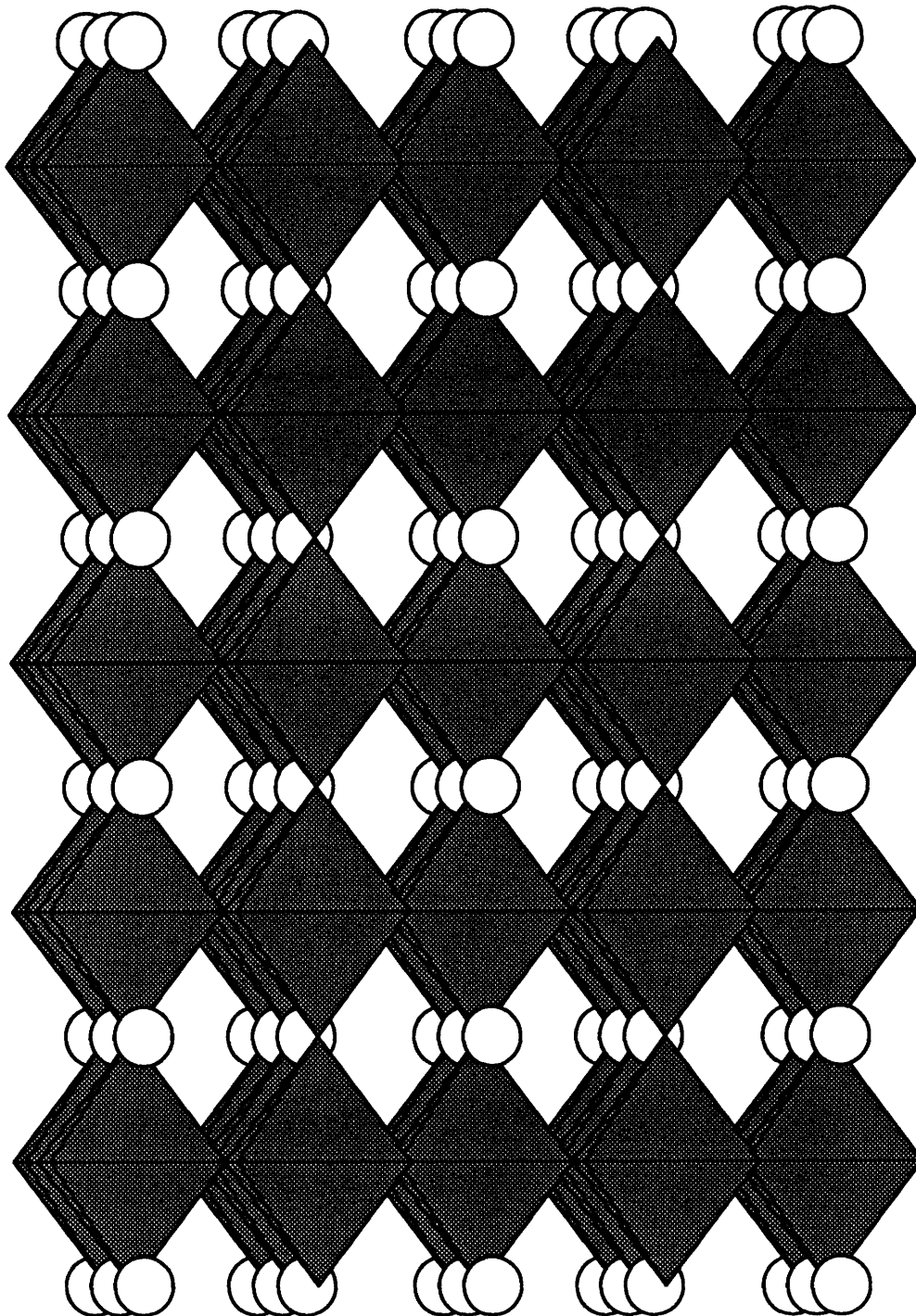
Figure 2.6 The perovskite structure, ABO₃ viewed along the [101] direction.
White spheres are A and gray octahedra are BO₆.
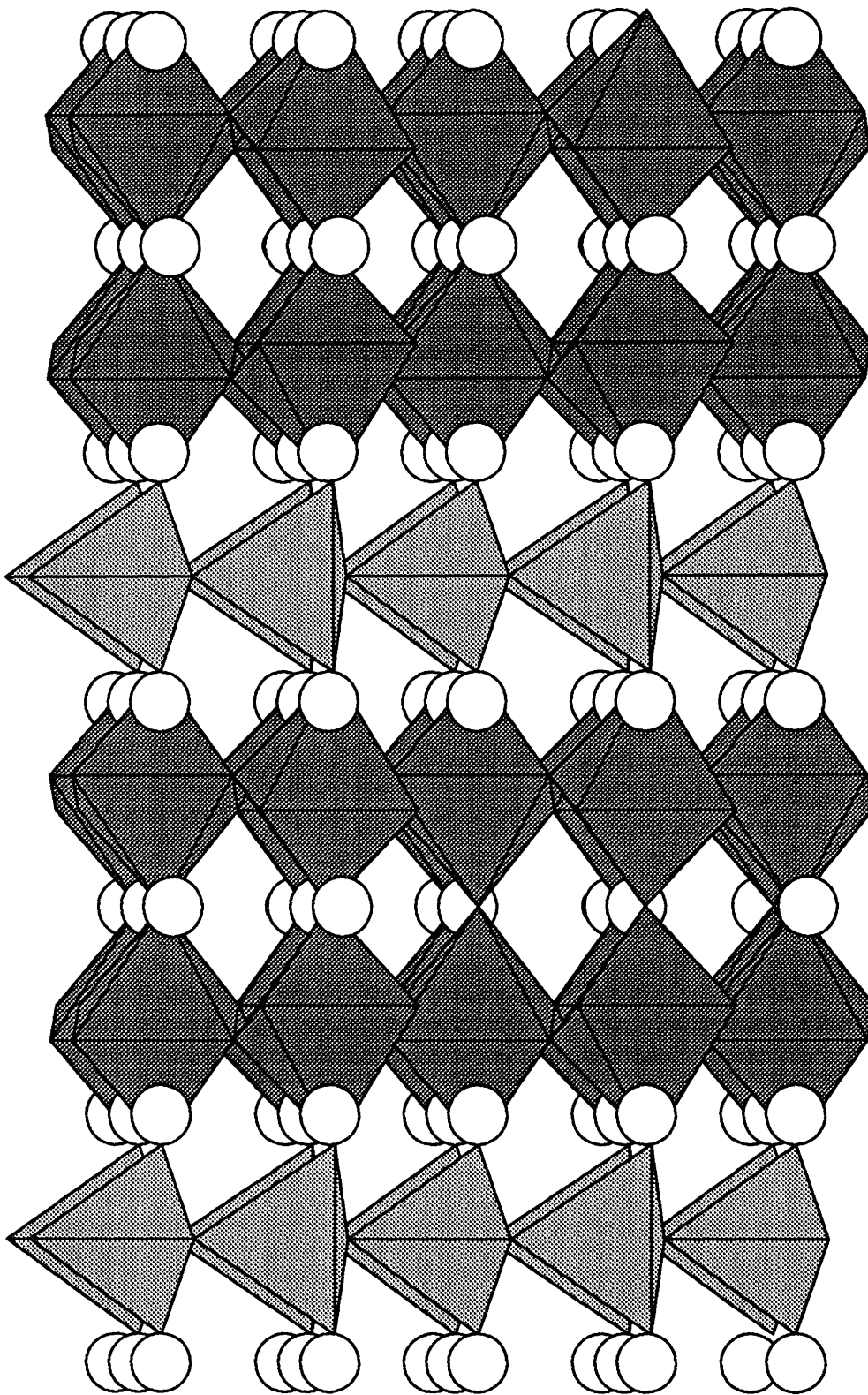
Figure 2.7 The structure of $Ca_3Fe_2TiO_8$. White spheres are Ca. Light Gray tetrahedra are $(Fe,Ti)O_4$, and gray octahedra are $(Ti,Fe)O_4$.

been prepared, so several techniques have been used to establish the structure including X-ray, electron, and neutron diffraction,[17] and Mössbauer spectroscopy.[18] The structure of $Ca_4Fe_2Ti_2O_{11}$ also has a single layer of tetrahedra, but has three perovskite layers. No other ordered intergrowths have been observed in the $CaTiO_3$-$Ca_2Fe_2O_5$ system.

The compounds $Ba_3In_2ZrO_8$ and $Ba_3In_2HfO_8$ were originally reported to be isostructural with $Ca_3Fe_2TiO_8$,[6] but further studies suggest that this system is a disordered cubic solid-solution.[19]

2.2.2 Conductivities

2.2.2.1 Brownmillerite materials

$SrFeO_{3-x}$ can exist for a wide range of x from 0 to 0.5. Of interest here is the x = 0.5 endmember, which has the brownmillerite structure at room temperature. In contrast to other brownmillerite structure materials, Ca_2FeAlO_5 and $Ca_2Fe_2O_5$, $Sr_2Fe_2O_5$ undergoes a structural order-disorder transition.[20,21] Through the use of high temperature diffraction this compound has been observed to transform from an orthorhombic structure with ordered oxygen vacancies at room temperature, to a cubic structure (disordered perovskite) above 700 °C, and back to the original orthorhombic structure when cooled. Ca_2FeAlO_5 and $Ca_2Fe_2O_5$ do not show a similar transition and do not show oxygen ion conduction, which $Sr_2Fe_2O_5$ does.[22]

In 1990, Goodenough et al.[6] reported on a new series of oxygen ion conductors. These materials consisted of $Ba_2In_2O_5$ and a series of intergrowths of $Ba_2In_2O_5$ and $BaMO_3$ perovskite materials. Single crystal studies on $Sr_2In_2O_5$[23] and $Ba_2In_2O_5$[24] revealed that while $Sr_2In_2O_5$ has the brownmillerite structure, $Ba_2In_2O_5$ has the cubic perovskite structure with random partial

occupancies of the oxygen site. Goodenough et al.[6] indexed the X-ray powder diffraction pattern of $Ba_2In_2O_5$ to an orthorhombic unit cell consistent with the brownmillerite structure. This structural distortion has been observed in polycrystalline samples by other researchers,[25,26] although a full structural refinement has not been performed. Goodenough et al. observed conductivity in $Ba_2In_2O_5$ of about 10^{-1} S cm^{-1} above 900 °C. Around 900 °C a jump in conductivity of more than an order of magnitude was observed. This was attributed to a disordering of the oxygen vacancies at high temperatures. Measurements of conductivity versus oxygen partial pressure revealed p-type conductivity at high partial pressures of oxygen, and ionic conductivity becoming predominant as oxygen partial pressures are reduced to 10^{-3} atmospheres. The oxygen partial pressure dependence was only studied down to 10^{-6} atmospheres, so the stability of this material at very low partial pressures is unknown. In an attempt to alleviate the discontinuity, the sample was doped with Ce^{4+} on the indium site. At a doping level of 12.5% no discontinuity in the conductivity was observed; however, a change in the activation energy was still present.

Other researchers have investigated $Ba_2In_2O_5$ to analyze the proposed order-disorder transition. Prasanna and Navrotsky[25] performed heat capacity measurements. They observed a first order transition (the heat capacity was the same before and after the transition), but the observed entropy of the transition itself was only four percent of that expected for a complete disordering from the brownmillerite to the perovskite structure. They suggest that full randomization of the oxygens does not occur; however, it also seems possible that full ordering does not occur. Interestingly, although the only single crystal structure of $Ba_2In_2O_5$[24] showed a defect perovskite,

quenching of polycrystalline $Ba_2In_2O_5$ has not yielded the defect perovskite at room temperature.

Adler et al.[26] have also studied this material. Using high temperature X-ray diffraction, they have observed that the sample maintains an orthorhombic structure until 1200 °C, at which point a cubic X-ray pattern is observed. Since this transition is significantly higher than that observed using differential thermal analysis or by conductivity measurements, a detailed high temperature ^{17}O NMR study was performed. From this they observed that the multiple oxygen peaks from the brownmillerite structure began to coalesce by 920 °C, where a single broad peak was observed. They explained their results as a two step process toward disordering. In the first step, the structure could undergo reorganization within the oxygen deficient layer. At higher temperatures the vacancies could be redistributed across other layers as well, thus the shift to a cubic crystal structure at 1200 °C.

Other brownmillerite structure compounds have also been prepared and studied for oxygen ion conduction. $Ca_2Cr_2O_5$ was found to be isostructural with $Ca_2Fe_2O_5$.[27] The conductivity of this material is not particularly high (10^{-3} S cm^{-1} at 900 °C), but oxygen partial pressure dependencies suggest that the conductivity is primarily ionic. Below 10^{-2} atmospheres of oxygen, the conductivity increased, indicative of n-type electronic conduction. This material did not show any evidence of an order-disorder type transition below 1000 °C, and it is unstable above this temperature.

Schwartz et al.[28] investigated $Ba_2GdIn_{1-x}Ga_xO_5$ (x = 0, 0.2, 0.4). The X-ray diffraction of Ba_2GdInO_5 was consistent with the brownmillerite structure (Ibm2), and the other samples appeared to be similar. Both the x = 0.2 and 0.4 samples showed good conductivity (about 5 x 10^{-3} S cm^{-1} at 600 °C), and the

activation energies were very low, 0.35 and 0.45 eV, respectively. They suggest that the increased conductivity in these materials relative to $Ba_2In_2O_5$ is due to a higher free volume. They tested the materials in a hydrogen-oxygen fuel cell at 600 °C and found no evidence of decomposition or degradation after several days.

Takeda et al.[29] studied a somewhat different series of materials based on Sr_2ScAlO_5. These materials show a disordered structure. When these materials were prepared above 1500 °C, they showed no evidence of vacancy ordering, giving a cubic X-ray diffraction pattern. They examined the materials by TEM and did not observe any microdomains or evidence of short range ordering. Sr_2ScAlO_5 shows only low levels of oxygen ion conduction $(10^{-4}$ S cm^{-1} at 1000 °C), but increases in conductivity were observed for any substitutions that they tried. Increasing the relative scandium to aluminum ratio increased the lattice parameters and also the conductivity. In general they found that the materials with the highest conductivities had the largest lattice parameters. The best material they found, $Sr_{1.8}Ba_{0.2}Sc_{1.2}Al_{0.6}Mg_{0.2}O_{4.9}$, had a conductivity of 10^{-2} S cm^{-1} at 1000 °C and the largest lattice parameters of any of the materials studied. All of the materials showed transference numbers greater than 0.8, but low densities in the materials most likely contributed to diffusion. Many of these compounds showed evidence of a different activation energy at temperatures below 400 °C, possibly indicating some protonic conduction.

Brownmillerite materials which undergo order-disorder transitions show significant conductivity above the order-disorder transition. These materials are unlikely to be useful in pure form; however, stabilization of the disordered structure to lower temperatures might create useful or interesting materials.

2.2.2.2 Brownmillerite-perovskite intergrowths

A series of brownmillerite-perovskite intergrowths, $Ba_3In_2MO_8$, M = Ce, Zr, or Hf, were also investigated[6] and showed interesting behavior, which led to further investigations by many researchers. This initial study reported anomalously high conductivities for all three materials at low temperatures (10^{-3} S cm^{-1} at 400 °C), and a saturation in conductivity above 500 °C. Low temperature activation energies were about 0.7 eV. The transference numbers, t_O, were found to be about 0.95. They used both quenching and slow cooling of their samples to investigate the possibility of disorder frozen into the samples, but the resultant conductivity differences were insignificant. Conductivity isotherms for $Ba_3In_2ZrO_8$ versus oxygen partial pressure showed predominantly oxygen ion conduction between 10^{-5} and 10^{-21} atmospheres of oxygen.[30]

In later studies, Goodenough and co-workers[19,31] studied these materials as a solid solution, $BaZr_{1-x}In_xO_{3-0.5x}$, where x = 0.67 corresponds to the previously studied $Ba_3In_2ZrO_8$. They observed an orthorhombic brownmillerite structure for x ≥ 0.8 and a cubic structure with disordered oxygen vacancies for x < 0.8. An increased unit cell was observed for 0.4 < x < 0.8 versus lower values of x. This increase was non-linear. They also reported increased conductivity and decreased activation energies for samples in this composition region. These studies also presented the likelihood of protonic rather than oxygen ion conduction, at least at low temperatures. Samples equilibrated under wet air showed higher conductivity than those heated under dried air. Samples heated under wet air or wet nitrogen showed a region of high conductivity at low temperatures with a plateau in conductivity between 400 and 500 °C. This is presumably

due to a reduced number of carriers as the materials lose water. Thermogravimetric analysis showed a weight uptake on cooling of about two percent under wet nitrogen. This would roughly correspond to water filling all of the vacant oxygen sites. Reversible loss of this weight is observed on heating. Samples heated under nitrogen which had been dried over P_2O_5 also showed some weight uptake. This was attributed to residual oxygen in the nitrogen.

Steele and co-workers[3,32] also investigated the $BaZr_{1-x}In_xO_{3-0.5x}$ solid solution for x values of 0.6 to 0.8. They found the conductivity was highest for x = 0.33, which also had the largest lattice parameters, but the conductivity was about two orders of magnitude lower than that originally reported by Goodenough.[6] They found that the activation energy increased with increasing Zr content, which gave a corresponding increase in cell volume. At the highest indium concentrations the conductivity decreased, possibly indicating some short-range ordering in the system. They also reported that $Ca_3Fe_2TiO_8$ showed conductivities about two orders of magnitude lower than $Ba_3In_2ZrO_8$, suggesting that ordering in the structure would decrease the conductivity.

This series of brownmillerite-perovskite intergrowths shows that ionic conduction can be influenced by intergrowth structures. Oxygen ion conductivity is observed, and this represents a possible new method for preparation and study of various ionic conductors. This method allows control over the number of oxygen vacancies as well as the ability to alter promising materials to improve on conductivity. The low temperature protonic conduction in these materials may also be useful.

2.3 Aurivillius Phases

Oxygen ion conductivity has also been observed in the Aurivillius phases, $(Bi_2O_2)^{2+}(A_{n-1}M_nO_{3n+1})^{2-}$. These consist of puckered bismuth oxide sheets and perovskitic regions. The structures of Bi_2WO_6, n = 1, and $BaBi_4Ti_4O_{15}$, n = 4, are shown in Figures 2.7 and 2.8, respectively. These structures can usually be approximated by a tetragonal unit cell, $a \approx 3.8$ Å and $c \approx 16, 25, 33, 41, 49$ Å for one through five layer systems.[33] However, based on their properties, such as ferroelectricity, and detailed crystal structure analyses, lower symmetries are generally present.[34] The large c parameter is due to the stacking sequence, in which the unit cell contains two perovskite regions and two bismuth oxide layers. The unit cell of $BaBi_4Ti_4O_{15}$ is shown in Figure 2.10.

Although they have no intrinsic vacancies, Bi_2WO_6 and Bi_2MoO_6 show high oxygen conduction.[35,36] Conductivity as high as 10^{-1} S cm^{-1} has been observed in single crystals of Bi_2WO_6 measured parallel to the bismuth oxide plane, while conductivity in a direction perpendicular to the planes is about 100 times lower.[36] The transference number is almost 1 at high PO_2, but decreases rapidly to about 0.3 under an oxygen partial pressure of 10^{-3} atmospheres.[37] Observed conductivity values for polycrystalline samples are somewhat lower (10^{-2} S cm^{-1} at 900 °C), but still show transference numbers close to unity for an air oxygen concentration cell.[35] Bi_2MoO_6 has been used as a catalyst for selective oxidation of olefins.[38]

$Bi_4V_2O_{11}$ ($Bi_2VO_{5.5}$) is the only Aurivillius phases with intrinsic oxygen vacancies. It was discovered simultaneously by Bush and Debreuille-Gresse.[39,40] Its γ-phase shows excellent oxygen ion conductivity above 570 °C,[41] but two other phases (α and β) exist at lower temperatures:
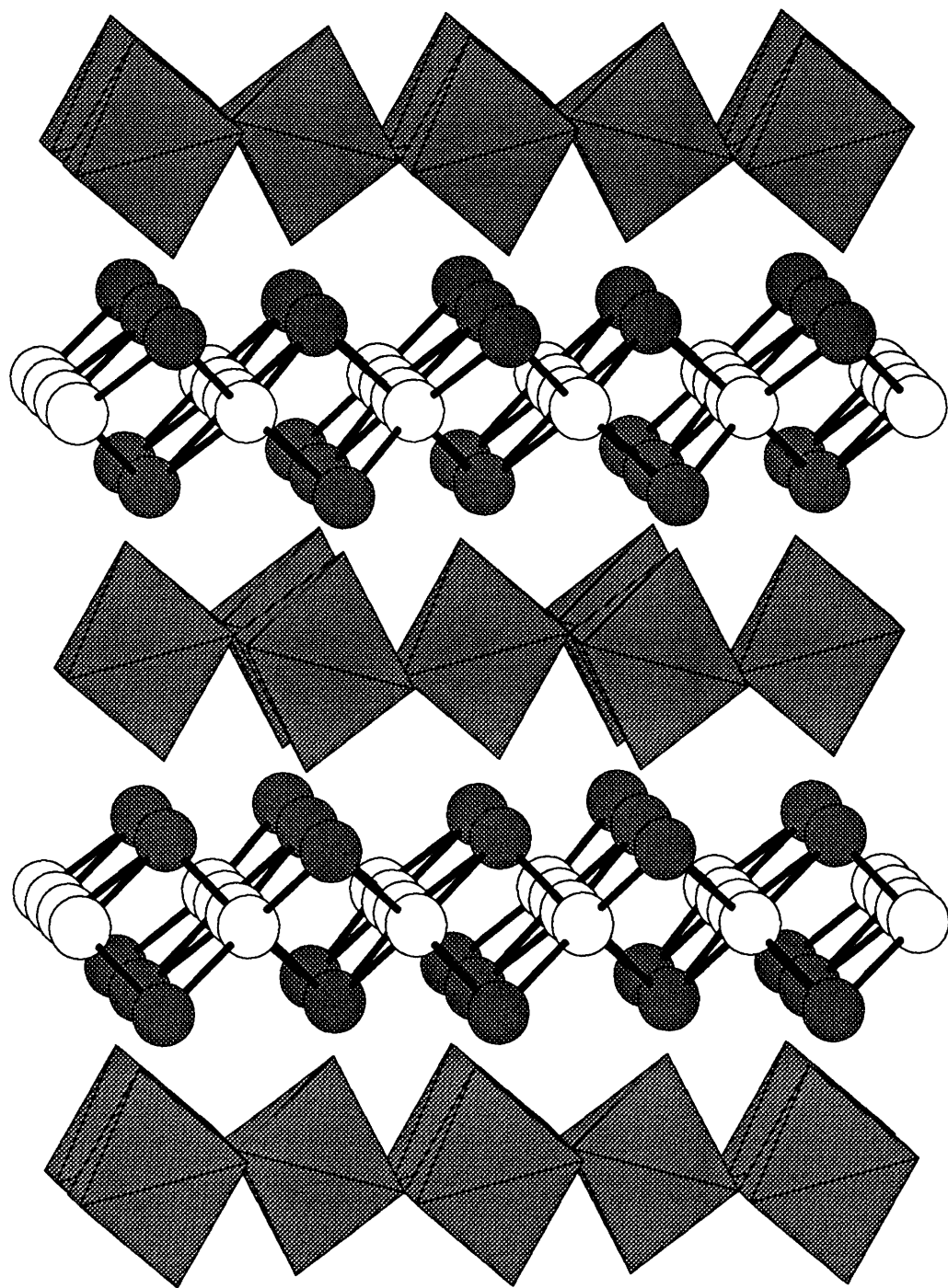
Figure 2.8 The structure of Bi_2WO_6. White spheres are oxygen. Dark gray spheres are bismuth, and octahedra are WO_6.
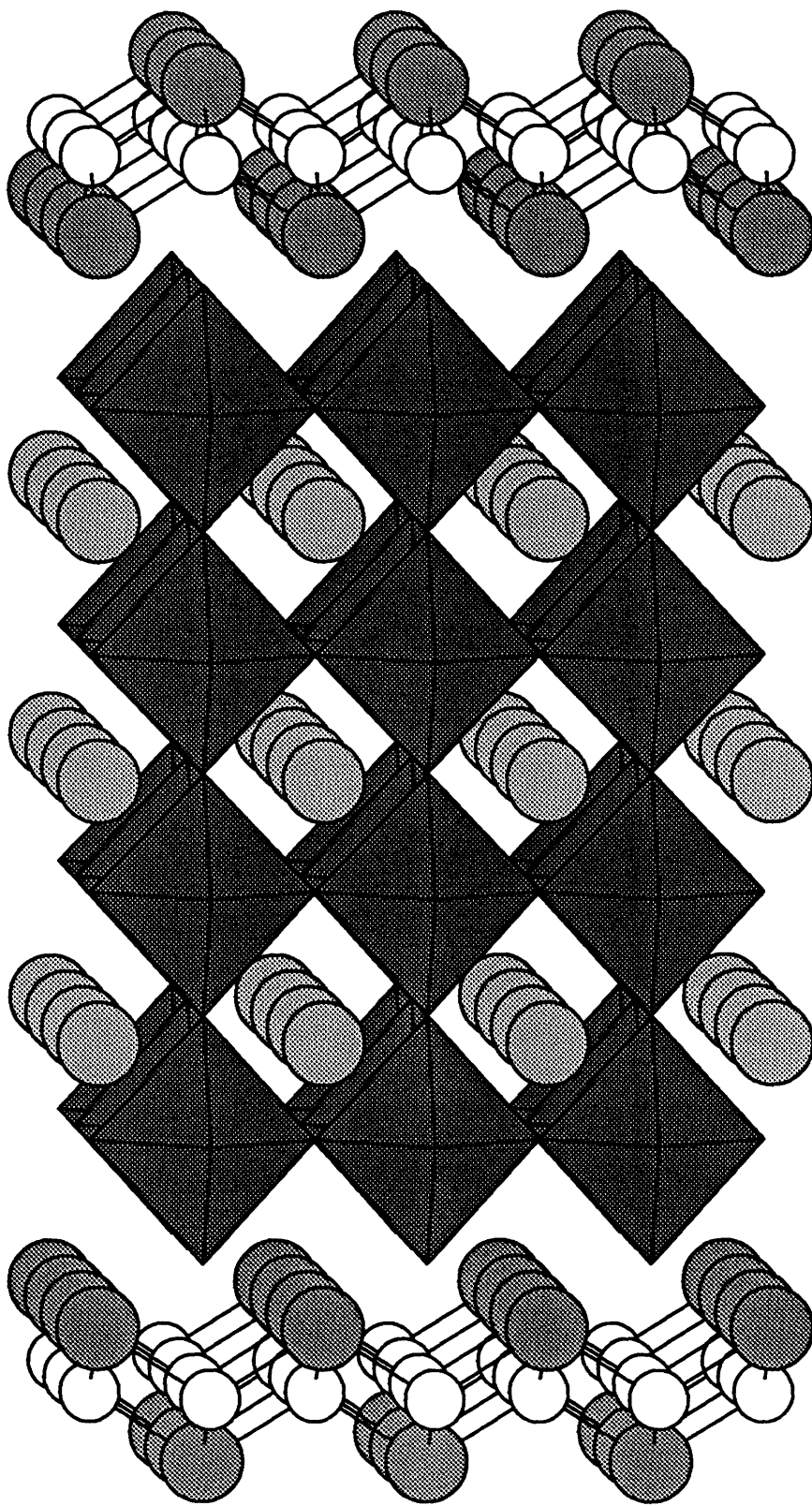
Figure 2.9 The structure of $BaBi_4Ti_4O_{15}$. White spheres are oxygen. Light gray spheres are Ba/Bi, and octahedra are TiO_6.
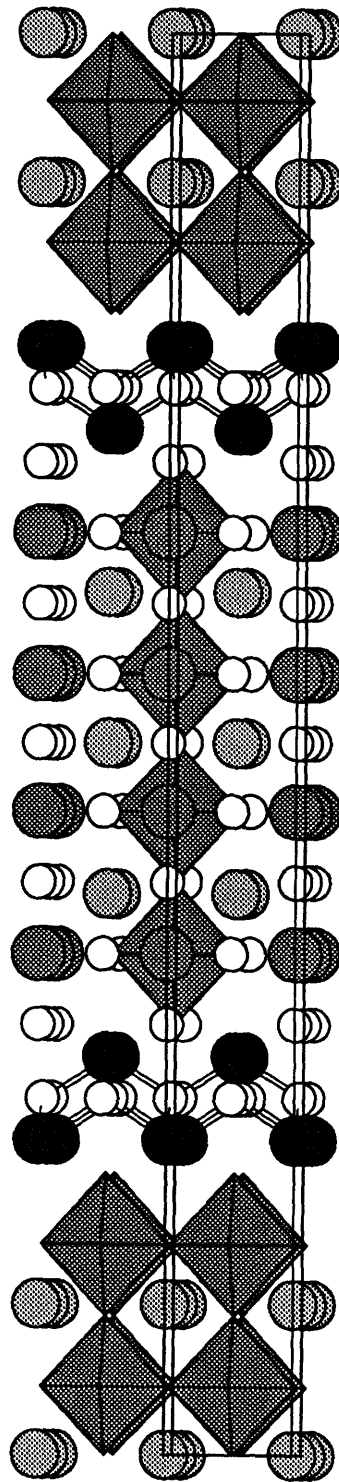
Figure 2.10 The structure of $BaBi_4Ti_4O_{15}$, showing the unit cell. White spheres are oxygen; light gray spheres are barium/bismuth; and dark gray spheres are bismuth/barium. Medium gray octahedra are TiO_6 and spheres of the same color are Ti.

$$\alpha - Bi_4V_2O_{11} \xrightarrow{\text{450 °C}} \beta - Bi_4V_2O_{11} \xrightarrow{\text{570 °C}} \gamma - Bi_4V_2O_{11}. \text{(2.10)}$$
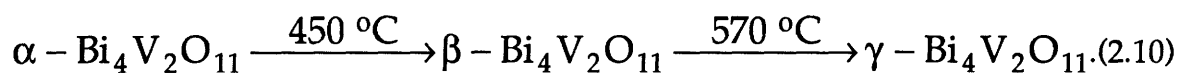
Using DTA two phase transitions could be observed on heating and cooling, although a significant hysteresis was observed for the α to β transition on heating versus the β to α transition on cooling. High temperature X-ray diffraction revealed that changes in crystallographic symmetry accompanied the phase transitions. All three phases showed significant superstructures as compared to the simplest analog, Bi_2MoO_6, so the structures have not yet been fully elucidated. It is clear, however, that the symmetry is increased on heating, indicating a decrease in ordering within the material. In the high temperature phase the oxygen vacancies are presumably disordered, while different orderings exist for each of the two low temperature phases. Although single crystals are readily obtained, they are largely twinned, so structural descriptions are minimal. Three conductivity regimes were observed, corresponding to the three phases. Although all three phases show significant oxygen ion conductivity, the high temperature phase is particularly interesting. It exhibits an extremely low activation energy (0.2 eV), a t_o close to unity, and a conductivity of about 10^{-1} S cm^{-1} at 600 °C.[42]

Abraham et al.[43] further studied this material, attempting to stabilize the γ-phases to lower temperatures. By doping the vanadium site with other metals, a new series of materials, the BIMEVOX family, is created. The solid solution, $Bi_2V_{1-x}Cu_xO_{5.5-3x/2}$ was the first to be reported and it is among the best. It has been characterized by single crystal measurements, which show that for $x \le 0.07$ the solid solution takes on the structure of the α-phase, while for $0.07 \le x \le 0.12$ the solution is isostructural with the γ-phase. Conductivity measurements on single crystals of both structures indicated that the structure was of primary importance to the conductivity. Crystals of the

α-phase displayed a jump in conductivity, while crystals of the γ-phase displayed only a change in activation energy with no discontinuity in conductivity. The materials stabilized into the γ-phase had significantly higher conductivities than those of the α-phase. The conductivity was observed to be highest in a direction parallel to the bismuth oxygen layers and more than an order of magnitude less perpendicular to the layers. The conductivity of sintered powders is closer to that of the parallel direction.[42] At high temperatures these materials have conductivities similar to YSZ and Bi_2O_3, but at lower temperatures they exhibit a significant improvement. The conductivity of the BIMEVOX materials is almost two orders of magnitude higher than Bi_2O_3 or YSZ below 400 °C.[42] Several other dopants have been used.[44,45] These also confirm that stabilization of the γ-phase is more important than the number of vacancies. Titanium and niobium doped samples seem to conduct as well as the copper doped samples. Several other metals (Li^+, Al^{3+}, Ge^{4+}) were not as successful in stabilizing the γ-phase and, consequently, showed little improvement in conductivity.

Electrochemical measurements on these samples show a transference number close to one, but some electronic conduction is present.[46] Measurements of conductivity as a function of oxygen partial pressure revealed small changes in the conductivity (about 2% at 200 °C and 4% at 650 °C), indicating a small electronic contribution to the conductivity. A concentration cell was used to evaluate the transference number, and the materials were found to be very non-ideal. This was attributed to electrode polarization due to slight electrical conductivity, but even this explanation could not account for the observed deviations, especially at low temperatures.

Recently a detailed X-ray and neutron diffraction study has been performed on powdered samples of the α-phase.[47] They determined that this

phase is likely monoclinic with ordered oxygen vacancies, giving tetrahedral and octahedral vanadiums. They proposed a series of structural changes from ordered oxygen vacancies in the α-phase, to non-equivalent vanadium-oxygen octahedra for the β-phase, and a more symmetrical structure for the γ-phase. This work nonetheless ignores much of the superstructure which has been observed in these materials.

The BIMEVOX family shows high oxygen ion conduction with significant limitations. These materials could be useful for catalysis or oxygen pumps, if electronic conduction is minimized. These materials have the highest low temperature conductivity of any known materials and, therefore, may be useful for low-temperature applications. Stability at low partial pressures of oxygen and higher temperatures is unlikely.

2.4 Conclusions

Although many materials have been studied for oxygen ion conduction, no single material is appropriate for all uses. YSZ must be used at high temperatures, but does not possess long-term stability at those temperatures. Bismuth oxide is easily reduced and has a low melting point. The BIMEVOX family, although promising, has similar limitations. Further studies of oxygen ion conductors are warranted to find improved materials. The use of intergrowths appears to be a promising approach to find new materials.

References

(1)   Kudo, T.; Fueki, K., *Solid State Ionics*; VCH: New York, NY, 1990.

(2)   Dell, R. M.; Hooper, A., In *Solid Electrolytes*; P. Hagenmuller and W. van Gool, Ed.; "Oxygen Ion Conductors", Academic Press: New York, 1978; pp 291-312.

(3)   Steele, B. C. H., Oxygen Ion Conductors and Their Technological Applications, **Mater. Sci. Eng. B-Solid State M.** (1992) **13**, 79-87.

(4)   Wells, A. F., *Structural Inorganic Chemistry*; Oxford University Press: New York, 1984.

(5)   Maier, J., Defect Chemistry: Composition, Transport, and Reactions in the Solid State; Part I: Thermodynamics, **Angew. Chem. Int. Ed.** (1993) **32**, 313-456.

(6)   Goodenough, J. B.; Ruiz-Diaz, J. E.; Zhen, Y. S., Oxide-ion conduction in $Ba_2In_2O_5$ and $Ba_3In_2MO_8$ (M = Ce, Hf, or Zr), **Solid State Ionics** (1990) **44**, 21-31.

(7)   Kilner, J. A.; Brook, R. J., A Study of Oxygen Ion Conductivity in Doped Non-stoichiometric Oxides, **Solid State Ionics** (1982) **6**, 237-252.

(8)   Cook, R. L.; Sammells, A. F., On the Systematic Selection of Perovskite Solid Electrolytes for Intermediate Temperature Fuel Cells, **Solid State Ionics** (1991) **45**, 311-321.

(9)   Sammells, A. F.; Cook, R. L.; White, J. H.; Osborne, J. J.; MacDuff, R. C., Rational Selection of Advanced Solid Electrolytes for Intermediate Temperature Fuel Cells, **Solid State Ionics** (1992) **52**, 111.

(10)   Cook, R. L.; Osborne, J. J.; White, J. H.; MacDuff, R. C.; Sammells, A. F., Investigations on $BaTh_{0.9}Gd_{0.1}O_3$ as an Intermediate Temperature Fuel Cell Solid Electrolyte, **J. Electrochem. Soc.** (1992) **139**, L19.

(11)   Iwahara, H., Oxide-ionic and Protonic Conductors based on Perovskite-type Oxides and Their Possible Applications, **Solid State Ionics** (1992) **52**, 99-104.

(12)   Takahashi, T.; Iwahara, H., Oxide Ion Conductors Based on Bismuthsesquioxide, **Mater. Res. Bull.** (1978) **13**, 1447-1453.

(13)   *Crystallographic and Magnetic Properties of Perovskite and Perovskite-related Compounds*; Goodenough, J. B.; Longo, J. M., Ed.; Springer-Verlag: Berlin, Heidelberg, 1970; Vol. 4. Magnetic and Other Properties of Oxides and Related Compounds, Part a, Landholt-Bornstein Numerical Data and Functional Relationships in Science and Technology, New Series Group III, pp 126-314.

(14)   Colville, A. A.; Geller, S., Crystal Structure of Brownmillerite, Ca_2FeAlO_5, **Acta Crystallogr. B-Struct. Sci.** (1971) **27**, 2311-2315.

(15)   Bertaut, E. F.; Blum, P.; Sagniéres, A., Structure du Ferrite Bicalcique et de la Brownmillerite, **Acta Crystallogr.** (1959) **12**, 149-159.

(16)   Anderson, M. T.; Vaughey, J. T.; Poeppelmeier, Structural Similarities among Oxygen-Deficient Perovskites, **Chem. Mater.** (1993) **5**, 151-165.

(17)   Rodríguez-Carvajal, J.; Vallet-Regí, M.; González Calbet, J. M., Perovskite Threefold Superlattices: A Structure Determination of the $A_3M_3O_8$ Phase, **Mater. Res. Bull.** (1989) **24**, 423-430.

(18)   Grenier, J.-C.; Pouchard, M.; Hagenmuller, P., In *Structure and Bonding*, "Vacancy Ordering in Oxygen-Deficient Perovskite-Related Ferrites", Springer-Verlag: 1981, Vol. 47; pp 1-25.

(19)   Goodenough, J. B.; Manthiram, A.; Kuo, J.-F., Oxygen Diffusion in Perovskite-related Oxides, **Mater. Chem. Phys.** (1993) **35**, 221-224.

(20) Shin, S.; Yonemura, M.; Ikawa, H., Order-Disorder Transition of $Sr_2Fe_2O_5$ from Brownmillerite to Perovskite Structure at an Elevated Temperature, **Mater. Res. Bull.** (1978) **13**, 1017-1021.

(21) Shin, S.; Yonemura, M.; Ikawa, H., Crystallographic Properties of $Ca_2Fe_2O_5$. Difference in Crystallographic Properties of Brownmillerite-like Compound, $Ca_2Fe_2O_5$ and $Sr_2Fe_2O_5$, at Elevated Temperatures, **Bull. Chem. Soc. Jpn.** (1979) **52**, 947-948.

(22) Rouxel, J., Institut des Materiaux de Nantes, Personal Communication.

(23) von Schenck, R.; Müller-Buschbaum, H., Über ein neues Erdalkalimetall-Oxoindat: $Sr_2In_2O_5$, **Z. anorg. allg. Chem.** (1973) **395**, 280-286.

(24) Mader, K.; Müller-Buschbaum, H., Notiz über einen Perowskit der Zusammensetzung $BaInO_{2.5}$, **Z. anorg. allg. Chem.** (1985) **528**, 125-128.

(25) Prasanna, T. R. S.; Navrotsky, A., Energetics of the Oxygen Vacancy Order-disorder Transition in $Ba_2In_2O_5$, **J. Mater. Res.** (1993) **8**, 1484-1486.

(26) Adler, S. B.; Reimer, J. A.; Baltisberger, J.; Werner, U., Chemical Structure and Oxygen Dynamics in $Ba_2In_2O_5$, **J. Am. Chem. Soc.** (1994) **116**, 675-681.

(27) Kontoulis, I.; Steele, B. C. H., Fabrication and Conductivity of a New Compound Calcium Chromium Oxide ($Ca_2Cr_2O_5$), **J. Eur. Ceram. Mater.** (1992) **9**, 459-62.

(28) Schwartz, M.; Link, B. F.; Sammells, A. F., New Brownmillerite Solid Electrolytes, **J. Electrochem. Soc.** (1993) **140**, L62-L63.

(29) Takeda, Y.; Imanishi, N.; Kanno, R.; Mizuno, T.; Higuchi, H.; Yamamoto, O., Oxide Ion Conductivity in Perovskite Type Sr_2ScAlO_5 and Related Compounds, **Solid State Ionics** (1992) **53-56**, 748-753.

(30)   Goodenough, J. B.; Zhen, Y. S., In *Solid State Ionics II*; G. A. Nazri, D. F.

         Shriver, R. A. Huggins and M. Balkanski, Ed.; "New Oxide-Ion

         Electrolytes", Materials Research Society: Pittsburgh, Pennsylvania,

         1991, Vol. 210; pp 287-301.

(31)   Manthiram, A.; Kuo, J. F.; Goodenough, J. B., Characterization of

         Oxygen-deficient Perovskites as Oxide-ion Electrolytes, **Solid State**

         Ionics (1993) **62**, 225-234.

(32)   Kontoulis, I.; Ftikos, C. P.; Steele, B. C. H., Oxygen ion conductivity in

         $Ba_3In_{3-x}Zr_xO_{7.5+x/2}$ (x=0.7-1.3), **Mater. Sci. Eng. B-Solid State M.** (1994) **22**,

         313-316.

(33)   Subbarao, E. C., Crystal Chemistry of Mixed Bismuth Oxides with Layer-

         Type Structure, **J. Amer. Ceram. Soc.** (1962) **45**, 166-169.

(34)   Frit, B.; Mercurio, J. P., The Crystal Chemistry and Dielectric Properties

         of the Aurivillius Family of Complex Bismuth Oxides with Perovskite-

         like Layered Structures, **J. Alloys Compounds** (1992) **188**, 27-35.

(35)   Takahashi, T.; Iwahara, H., High Oxide Ion Conduction in the Sintered

         Oxides of the System Bi_2O_3-WO_3, **J. Appl. Electrochem.** (1973) **3**, 65-72.

(36)   Yanovskii; Voronkova, Rapid Anion Transfer in Bi_2WO_6 Crystals,

         Soviet Physics and Solid State (1982) **24**, 1603-1604.

(37)   Utkin, V. I.; Roginskaya, Y. E.; Voronkova, V. I.; Yanovskii, V. K.;

         Galyamov, B. S.; Venevtsev, Y. N., Dielectric Properties, Electrical

         Conductivity, and Relaxation Phenomena in Ferroelectric Bi_2WO_6,

         Phys. Stat. Solidi A-Appl. Res. (1980) **59**, 75-82.

(38)   Batist, P. A.; Bouwens, J. F. H.; Schuit, G. C. A., Bismuth Molybdate

         Catalysts: Preparation, characterization and Activity of Different

         Compounds in the Bi-Mo-O System, **J. Catal.** (1972) **25**, 1-11.

(39)   Bush, A. A.; Venetsev, Y. N., Crystals of the New Phase $Bi_4V_2O_{11}$ in the Bi_2O_3-V_2O_5 system, **Russ. J. Inorg. Chem.** (1986) **31**, 769-771.

(40)   Debreuille-Gresse, Thesis, Universite de Lille, 1986.

(41)   Abraham, F.; Debreuille-Gresse; Mairesse, G.; Nowogrocki, G., Phase Transitions and Ionic conductivity in $Bi_4V_2O_{11}$, an Oxide with a Layered Structure, **Solid State Ionics** (1988) **28-30**, 529-532.

(42)   Mairesse, In *Fast Ion Transport in Solids*; B. Scrosati, Ed.; "Bismuth-based Oxide Conductors: Novel Structure and Electrical Features", Kluwer: The Netherlands, 1993; pp 271-290.

(43)   Abraham, F.; Debreuille-Gresse; Mairesse, G.; Nowogrocki, G., The BIMEVOX Series: A New Family of High Performance Oxide Ion Conductors, **Solid State Ionics** (1990) **40/41**, 934-937.

(44)   Sharma, V.; Shukla, A. K.; Gopalakrishnan, J., Effect of Aliovalent-cation Substitution on the Oxygen-ion Conductivity of $Bi_4V_2O_{11}$, **Solid State Ionics** (1992) **58**, 359-362.

(45)   Goodenough, J. B.; Manthiram, A.; Paranthaman, P.; Zhen, Y. S., Fast Oxide-ion Conduction in Intergrowth Structures, **Solid State Ionics** (1992) **52**, 105-109.

(46)   Iharada, T.; Hammouche, A.; Fouletier, J.; Kleitz, M.; Boivin, J. C.; Mairesse, G., Electrochemical Characterization of BIMEVOX Oxide-ion Conductors, **Solid State Ionics** (1991) **48**, 257-265.

(47)   Joubert, O.; Jouanneaux, A.; Ganne, M., Crystal Structure of Low-Temperature Form of Bismuth Vanadium Oxide Determined by Rietveld Refinement of X-ray and Neutron Diffraction Data (α-$Bi_4V_2O_{11}$), **Mater. Res. Bull.** (1994) **29**, 175-184.

Chapter 3
Experimental Methods

3. EXPERIMENTAL METHODS

This section presents the details of the methods used in this thesis. Sample preparation is presented first, followed by characterization techniques. Powder X-ray diffraction (XRD) was used extensively to determine if samples were single-phased as well as to determine the structures of the final products. Neutron diffraction was also used for structure determination of some samples. Complex impedance was used to measure the conductivity of the samples. Simultaneous differential thermal analysis and thermogravimetric analysis were used to analyze phase transitions.

3.1 Sample Preparation

All characterized samples were prepared by solid state reactions. Unless a larger sample was needed for analysis, samples were prepared in five gram quantities. Initially finely divided powders of the oxides or carbonates were weighed out in stoichiometric quantities and ground under acetone with an agate mortar and pestle. The acetone helps to keep the fine powders in the bottom mortar. The starting materials, purities, and suppliers are listed in Table 3.1. For the first heating, samples were ground for one-half to one hour, while the acetone was allowed to evaporate. The acetone was further allowed to evaporate for about an hour. After this, the samples were pressed into 13 mm diameter pellets. Pellets were pressed at 5000 pounds using a uniaxial press. A stainless steel die was used for the early experiments (most of the brownmillerite-perovskite intergrowths), while a carbide press was used for the later experiments. From this point the preparation of the two types of intergrowths differs somewhat.

Table 3.1 Suppliers and purities of starting materials

Material	Supplier	Purity
$BaCO_3$	Johnson Matthey Aesar	99.9
$SrCO_3$	Johnson Matthey	99.999
$CaCO_3$	Johnson Matthey	99.97
TiO_2, anatase	Aldrich	99.9+
ZrO_2	Spex	99.9
HfO_2	Cerac	99.95
α-Al_2O_3	Johnson Matthey	99.99
Ga_2O_3	Johnson Matthey	99.999
In_2O_3	Cerac	99.99
Sc_2O_3	Aran Isles	99.99
Bi_2O_3	Johnson Matthey Aesar	99.99

3.1.1 Preparation of Brownmillerite-Perovskite Intergrowths

These samples were initially heated in an alumina boat to 1250 °C for 24 to 48 hours. The heating rates were 20 degrees per minute, while cooling rates were 10 degrees per minute. The samples at this point were typically highly cracked, with the pellet divided into several layers. Powder XRD of samples at this point showed little of the final product and often little reaction other than the loss of CO_2 from the carbonate materials. Samples were reground without using acetone and repelletized. Heating cycles at this point depended on the sample. $Ba_3In_2TiO_8$ could be prepared at temperatures as low 1250 °C, while most other materials required temperatures of at least 1350 °C for complete reaction. Samples were reheated at progressively higher temperatures until the reaction was complete as monitored by XRD. Typical total reaction times were one to two weeks. A final heating cycle 50 to 100 degrees higher than previous temperatures was used in attempt to make dense samples. Densities, however, were typically only about 65 percent of the theoretical density based on XRD and predicted structures. The pellets were stored in a vacuum dessicator when not being measured, as they were found to crack after extended exposure to moisture.

3.1.2 Preparation of Aurivillius-Brownmillerite Intergrowths

The Aurivillius-brownmillerite intergrowths and the Aurivillius phases were placed on platinum foil for all heating cycles to avoid reaction with the alumina boat. All samples were initially heated slowly (10 to 30 °C per hour) to 800 °C or slightly higher. Bismuth oxide is low melting, and slow heating rates allowed reaction of Bi_2O_3 with other components before the melting point was reached. It was important to stay below the melting

point of the mixture at all times since the bismuth oxide mixtures quickly leeched through the alumina crucibles if they were not contained by the platinum foil. For the Aurivillius-brownmillerite intergrowths presented in this thesis, optimal heating cycles were found to consist of heating over three days to 800 °C, followed by two weeks at 850 to 900 °C with intermittent grinding. To obtain dense samples, these materials were heated to 1000 or 1050 °C for two hours. These samples did not appear to have any significant sensitivity to air or moisture.

3.2 X-ray Diffraction Measurements

Powder X-ray diffraction measurements were performed on a Rigaku RU-300 rotating anode diffractometer using copper radiation. All measurements were run at 50 kV and 200 mA. The same size slits were used for all runs: divergence slit, 0.5 degrees; scatter slit 0.5 degrees; and receiving slit, 0.15 mm. Routine measurements to check sample composition and purity were run in continuous scan mode at a rate of 20 degrees per minute and a step size of 0.04 degrees. Scans were routinely collected from 3 to 88 ° 2θ. If the pellet remained intact through the heating cycle, X-ray measurements were performed on pellets using the aluminum sample holder, shown in Figure 3.1. Otherwise the pellets were ground, and small amounts of the powder were mixed with a Collodion-amyl acetate binder and applied to a glass slide. To determine lattice parameters, the slide preparation technique was used, and an internal standard of silicon (NBS SRM #640B) or mica (NBS SRM #675) was mixed with the sample at a ratio of approximately 1:1, as required to give comparable intensity to the sample. Slower scans were used to accurately determine peak positions, either continuous scans at 5 degrees per minute and 0.01 degree steps or step scans at 0.01 degree step size
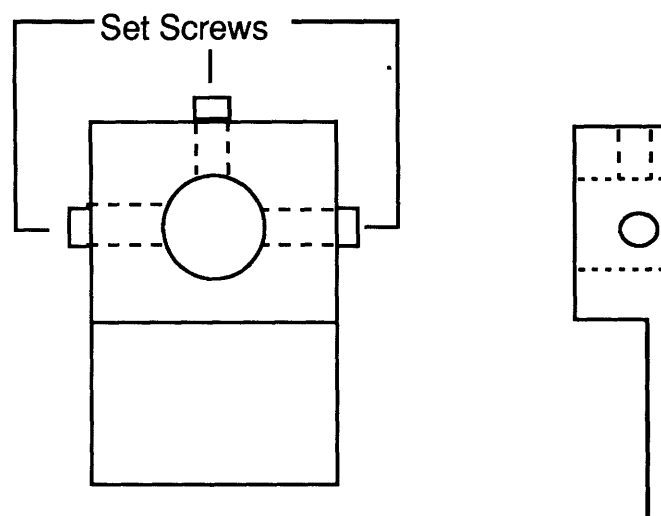
Figure 3.1 Sample holder for X-ray diffraction measurements on pellets. The sample holder consists of a machined aluminum block, and the sample is held in place by set screws.

and 0.5 second collection time. TREOR[1] and the NRCVAX program PPLP[2] were used to determine lattice parameters from the XRD patterns. Collection for structural analysis using Rietveld refinement was much slower. Data were collected from 5 to 105 or 140 degrees in step scan mode using 0.01 to 0.02 degree step sizes and 5 to 10 second counting times. Rietveld refinements were performed using GSAS[3] software.

High temperature XRD was performed on a Rigaku RU-200 rotating anode diffractometer equipped with a Rigaku hot stage. The hot stage was controlled by an Omega temperature controller. Two type R platinum-rhodium thermocouples were used. One controlled the furnace temperature and the other was attached to the sample holder and measured the sample temperature. Samples for the hot stage had to be between 1 and 1.5 mm thick. Thin pellets 13 mm in diameter were prepared and sintered. Due to the vertical sample mounting of this stage, it was necessary for the pellet to be sturdy enough to maintain its shape throughout the experiment. A triangular file was used to notch the pellet, so that thin platinum wires could be used to tie it to the sample holder. The sample holder is not designed to align the sample automatically in any way. Before measurement on the high temperature stage, samples were measured on the RU-300 to determine accurate peak positions and lattice parameters. This measurement was used to align the sample on the hot stage. Using the alignment mechanism on the high temperature stage, it was possible to bring the 100 percent peak into alignment, but alignment of other peaks was not assured. Therefore, the room temperature measurement of the sample thus aligned on the hot stage was calibrated against the previously obtained peak positions, and the same calibrations were used for all samples. The RU-200 produces less power, so samples were run at 40 kV and 150 mA. In addition the hot stage uses nickel

foil as a shield for stray X-rays, so the overall intensity was significantly decreased versus conventional room temperature measurements. All high temperature diffraction measurements were run as step scans to improve the limited signal intensity. A relatively small scan range was used, 29 to 64 $^\circ$ 2θ. A step size of 0.02 degrees was used with a count time of 1.0 seconds. The sample was allowed to equilibrate for about half an hour at each temperature.

3.3 Differential Thermal Analysis

Differential thermal analysis was used to look for phase transitions in the materials. Measurements were performed in air on a TA Instruments SDT 2960 simultaneous TGA/DTA. Samples were heated at 25 °C per minute to 1000 °C in platinum crucibles.

3.4 Conductivity Measurements

3.4.1 Background

Ionic conductivity cannot be measured using simple dc conductivity. Many other approaches are used, but the most common is complex impedance. This technique measures the frequency dependent electrical impedance. If electrical processes in the material have different frequency dependencies, it can be used to distinguish between them. Phenomena such as bulk, grain boundary, and electrode impedances are frequently separated by this technique. A polycrystalline material is typically represented by a series of three parallel RC elements as show in Figure 3.2. The Cole-Cole plot of the complex impedance spectrum of a single RC element is a semicircle, and the spectrum of the three elements in series is expected to give three semicircles as shown in Figure 3.3. The Cole-Cole plot is a plot of the imaginary versus
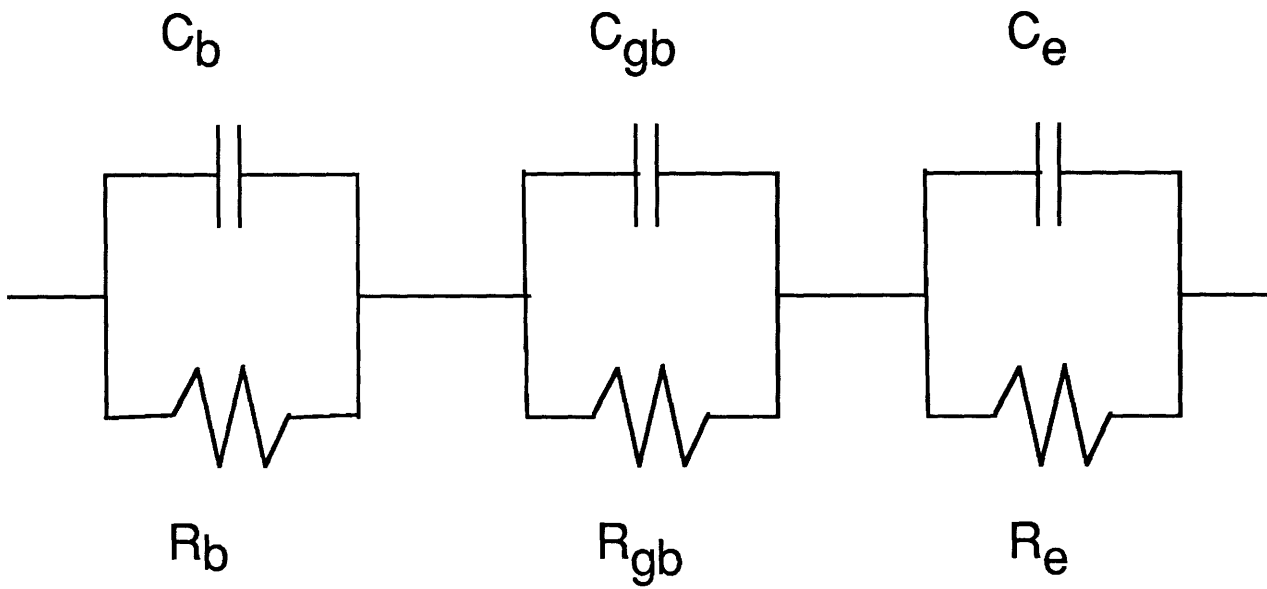
Figure 3.2 Electrical model for complex impedance of polycrystalline samples showing a series of capacitor and resistor parallel circuits.
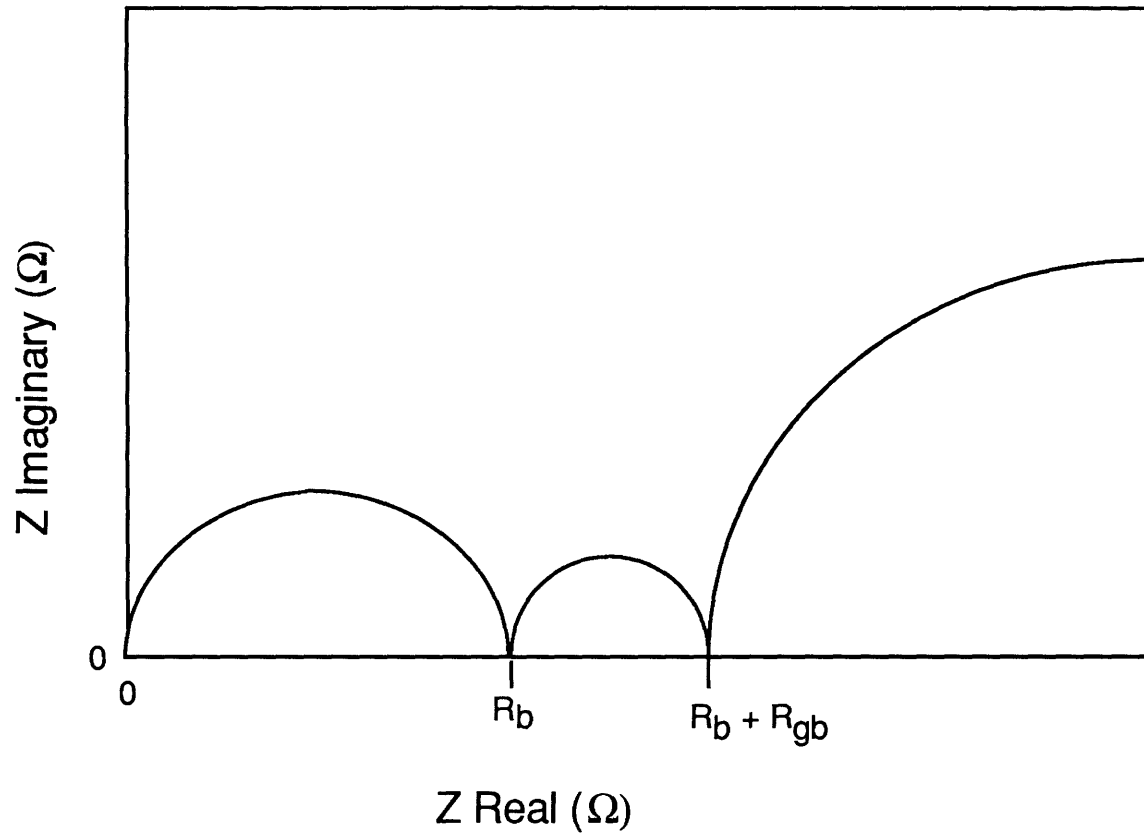
Figure 3.3 Idealized complex impedance plot for a polycrystalline sample showing three arcs: bulk, grain boundary, and electrode.

the real impedance of the material. The resistance of each phenomena is taken as the distance across the circle along the real axis. This is also illustrated in Figure 3.3. For ionic conductors with blocking electrodes (electrodes which do not supply or produce the ions involved in conduction, in this case O^{2-}) it is expected that the electrode impedances will be very large, and this was observed at low temperatures. At higher temperatures the platinum electrodes can catalyze the formation of O^{2-}, so the electrode resistance decreases.

3.4.2 Measurement of Complex Impedance

Disk shaped samples were used in all measurements. The faces of the disk were sanded with 600 grade emery paper. The thickness and diameter of the samples were then measured to 0.02 mm using calipers. The samples were also weighed to determine the densities. The faces of some samples were coated with platinum ink. The use of platinum ink necessitated another brief heating cycle to remove the binder from the Pt. Silver paint that required no heat treatment was also applied to some samples. No difference was observed between samples measured with silver paint, with platinum ink, and no coating. The pellet was mounted in the sample holder shown in Figure 3.4. This sample holder was modified from that used by Moon.[4] It can be sealed to allow atmospheric control and gas flow through the system. It consists of two half-inch double-bore mullite tubes which press on the sides of the sample. If gas flow through the sample holder was desired, a hole was drilled through the side of each tube into one of the bores. A platinum wire runs down one bore of each tube, and a circular platinum sheet approximately the same size as the pellet is attached to it by running the wire through holes in the foil. A type K, chromel-alumel, thermocouple

Gas Flow

Thermo
Couple

Nickel Tube

Pt Wire

Electrode

Rubber Cord

Thermocouple

Sample

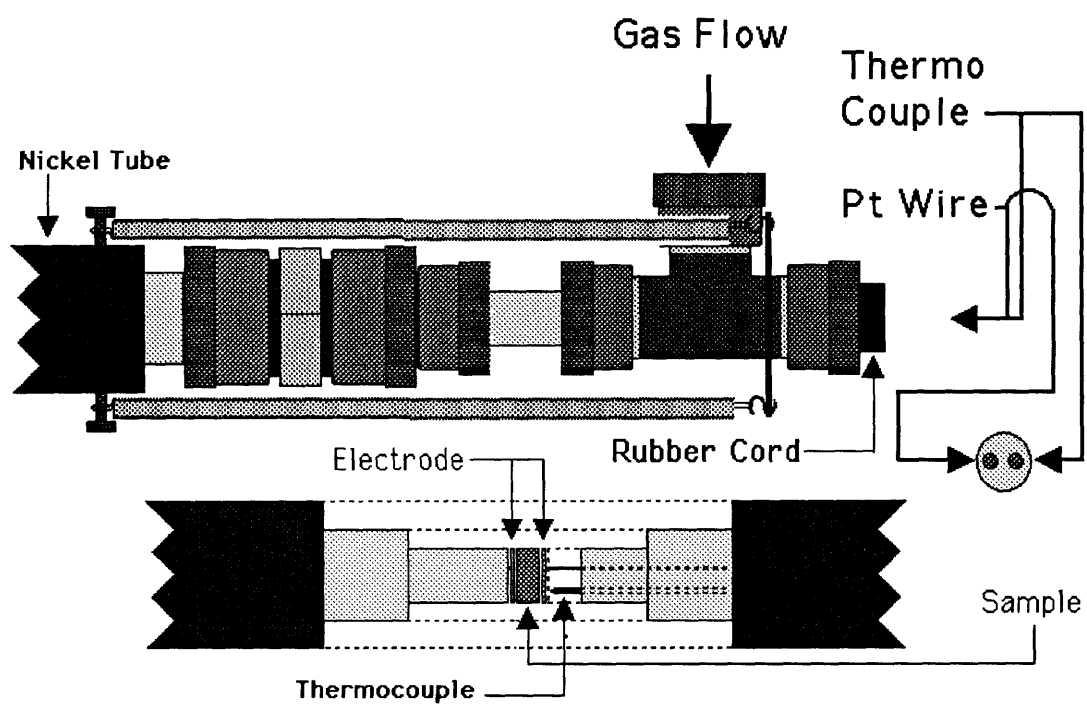Figure 3.4 Sample holder for complex impedance measurements.

with an inconel sheath is inserted into one of the tubes. These tubes are inserted into a 0.75 inch outer mullite tube which is in turn inserted into a nickel or inconel tube. A series of Ultratorr® fittings are used to seal the sample holder as well as to provide an attachment for springs. The sample is spring loaded to insure good contact with thermal expansion. The springs run from an Ultratorr® fitting at the end of each tube to the nickel tube. Due to the spring loading, the sample was always found to adhere to the platinum electrodes by the end of the run. This is most likely why no effect was observed in applying platinum or silver directly to the samples. The tube is grounded to provide electrical shielding for the sample. Rubber cord can be used to seal the Ultratorr® fittings and allow feed-through of wires and thermocouples. The external wires are fit with BNC connectors to allow easy changing among samples.

Conductivity measurements on the sample were performed using a Solartron 1260 Impedance/Gain-Phase Analyzer with Z-Plot software.[5] A frequency range of 5 MHz to 1 Hz was scanned, taking 10 measurements per decade. Measurements were taken as a function of temperature at a rate of two to four measurements per day. It was found experimentally that sample equilibration at a given temperature was not reached in less than four hours. Samples were typically measured from about 400 to 950 °C in increments of 50 °C. Samples were also measured on cooling in similar although staggered increments.

The resistance of the sample can be determined at each temperature through Cole-Cole plots of the impedance. The intercept (the resistance) is found by fitting the circle and calculating the intercepts with the x-axis. The conductivity can then be calculated from the resistance as follows:

$$\sigma = \left(\frac{L}{A}\right)\left(\frac{1}{R}\right),$$ (3.1)

where L and A are the length and area and R is the resistance. An Arrhenius of $\ln(\sigma T)$ versus $1/T$ to determine the activation energy, based on the equation,

$$\sigma = \sigma_0 \exp\left(\frac{-E_a}{kT}\right).$$ (3.2)

Although $\ln(\sigma T)$ must be used to fit the data, $\log(\sigma)$ is often used for clarity and adds little curvature to the plot.

3.4.3 Measurement of Oxygen Partial Pressure Dependencies

The oxygen partial pressure dependence of some samples was measured. The gas flow system shown in Figure 3.5 was set up to accomplish this. Premixed tanks of oxygen-argon mixtures and CO/CO_2 mixtures in argon were purchased from Middlesex or Matheson. The actual mixtures are listed in Table 3.2. The CO/CO_2 mixtures were used to obtain low oxygen partial pressures. The partial pressure of such mixtures can be predicted from Equation 3.3,[6]

$$\log PO_2 = -\frac{29508}{T} + 9.071 + 2\log\frac{P_{CO_2}}{P_{CO}}.$$ (3.3)

These were set up so that adjacent cylinders could be mixed to increase the effective number of gases. An MKS #247 4-channel readout with two 1200 series mass flow controllers was used to control flow rates in the gases. The two controllers had maximum flow rates of 50 and 200 ccm. The gases were

passed through a stainless steel tube filled with stainless steel shot to provide mixing. The gases were measured for oxygen content using the zirconia oxygen sensors illustrated in Figure 3.6. The oxygen sensors were constructed from zirconia tubes with a single open end. The tubes had an external diameter of 0.75 inches and were about 12 inches long. The inside and outside of the tube end was coated with platinum ink to create electrodes. These were sealed using Ultratorr® fittings in a manner similar to that of the sample holders. In this case, however, extra fittings were required to allow gas flow in and out of the same end of the sample holder. A one-quarter inch diameter alumina tube was used as an oxygen conduit to the inner end of the tube, as well as an electrical insulator for a platinum wire which ran to the end of the tube and was connected to a piece of platinum foil in contact with the tube end. The external electrode ran down a secondary alumina tube of small diameter. These oxygen sensors were placed directly before and after the sample in the gas flow path. The oxygen content was determined by measuring the voltage through the zirconia sensor and using the Nernst equation:

$$EMF = -\frac{RT}{4F} \ln \frac{P_{O_2}}{P_{O_2} \text{ (ref)}} \qquad (3.4)$$

The samples were measured under several different gas mixtures at a single temperature. Only two measurements were taken per day so that each gas could be allowed to equilibrate for several hours. Measurements were performed from high to low p_{O_2} to minimize any effects from irreversible sample or electrode degradation.

Table 3.2 Gases used in oxygen partial pressure measurements

Tank	Gas	Grade
1	Oxygen	4
2	100 ppm O_2 in Argon	certified
3	1 % O_2 in Argon	certified
4	Argon	5
5	CO_2	4
6	1000 ppm CO, 1% CO_2 in Argon	certified
7	100 ppm CO, 10 % CO_2 in Argon	certified
8	1% CO, 1000 ppm CO_2 in Argon	certified

Symbol	Item
o	2-way valve
▽	3-way valve
⬡V	5-way valve
▽	3-way needle valve
⊙	check valve (1 psi)
F	flow meter
⊢	union tee

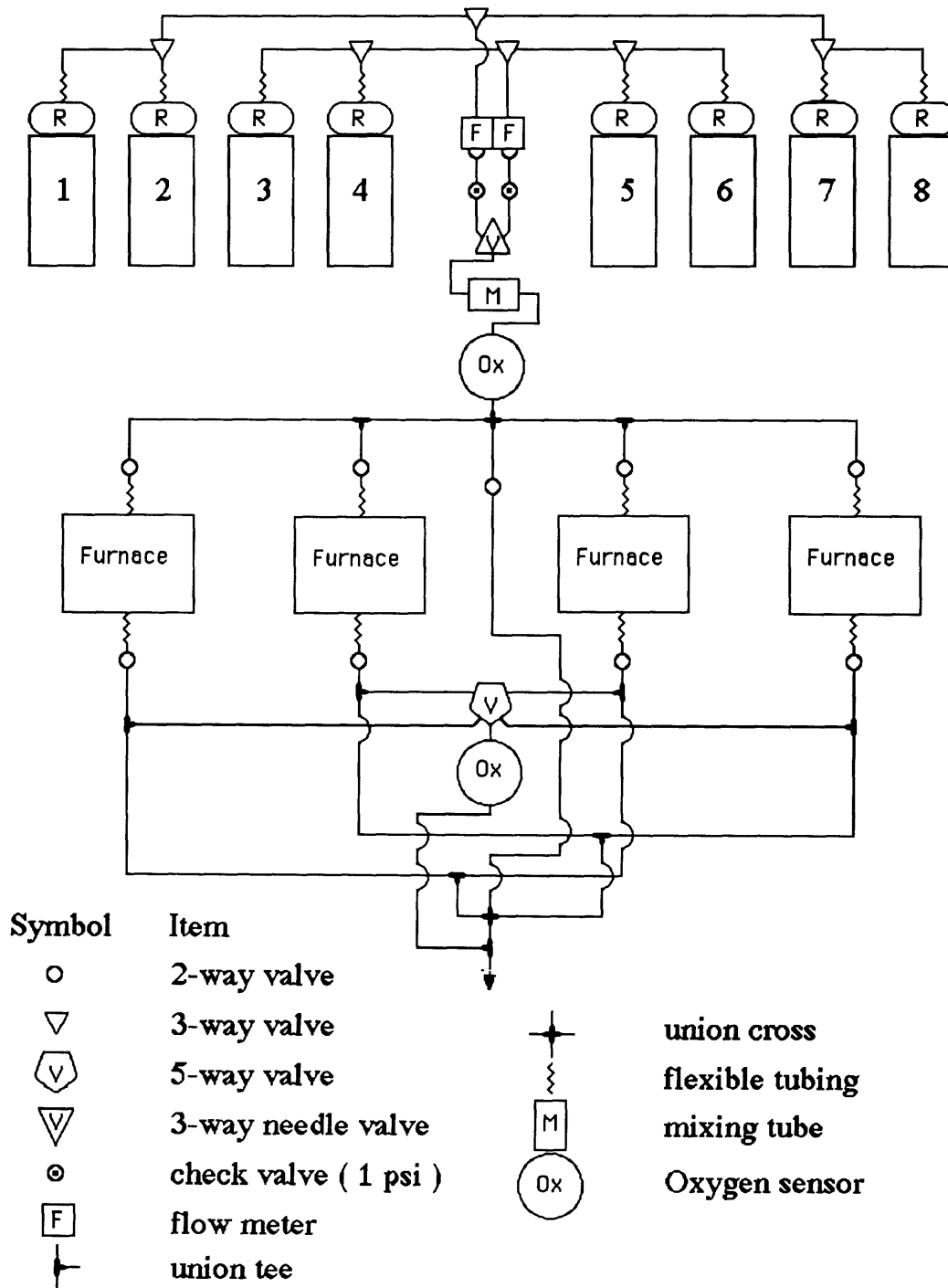|	
┼	union cross
⌇	flexible tubing
M	mixing tube
Ox	Oxygen sensor

Figure 3.5 Diagram of the gas flow system for measuring oxygen partial pressure dependencies
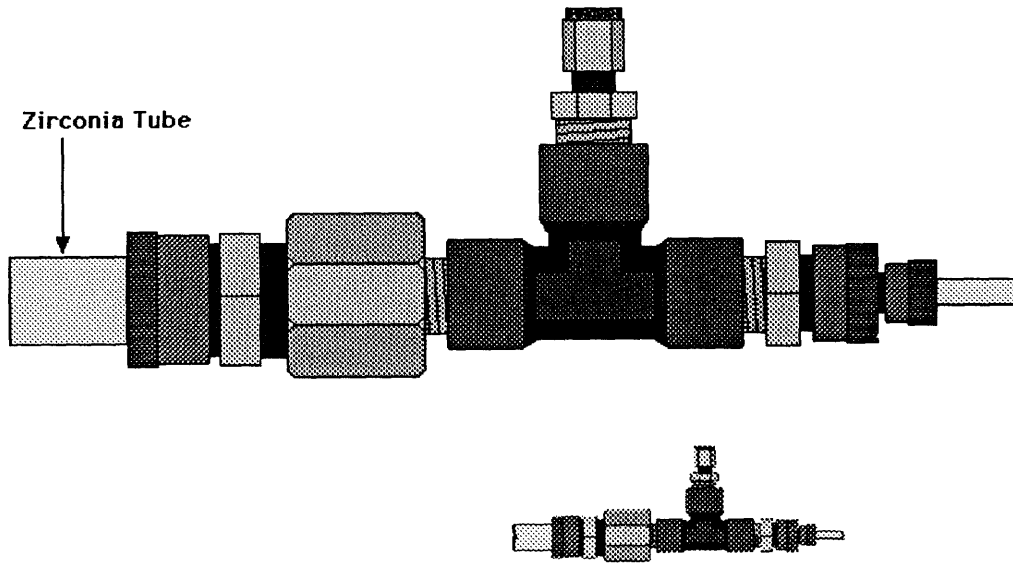
Zirconia Tube

Figure 3.6 Diagram of the oxygen sensor used in the gas flow system.

3.5 Neutron Diffraction Measurements

Neutron diffraction measurements on polycrystalline samples were run at Brookhaven National Laboratory on the H4S diffractometer with the help of Uli Wildgruber. Neutron diffraction was used to elucidate the oxygen ordering in these materials since X-ray diffraction is not particularly sensitive to oxygen relative to the large metals in these samples. Samples were prepared as pellets of approximately ten grams. Measurements were collected from 5 to 120 ° 2θ in 0.1 ° step sizes. Data were collected at each point for a fixed number of counts on a fraction of the beam. This is due to fluctuation in the neutron flux. The wavelength of the neutrons was calibrated versus a cerium oxide sample to 1.355 nm. These data were collected by computer and also analyzed using GSAS. The structures were analyzed using both XRD and neutron data.

References

(1)   Werner, P.-E.; Eriksson, L.; Westdahl, M., TREOR, A Semi-exhaustive trial-and-error powder indexing program for all symmetries, **J. Appl. Crystallogr.** (1985) **18**, 367-370.

(2)   Gabe, E. J.; Page, Y. L.; Charland, J.-P.; Lee, F. L.; White, P. S., NRCVAX -- An Interactive Program System for Structure Analysis, **J. Appl. Crystallogr.** (1989) **22**, 384.

(3)   "GSAS: General Structure Analysis System," Larson, A. C.; Von Dreele, R. B., Los Alamos National Laboratory, 1990.

(4)   Moon, P. K., Ph. D. Thesis, Massachusetts Institute of Technology, 1988.

(5)   "ZPLOT Electrochemical Impedance Software," Scribner Associates, Inc., 1991.

(6)   Gaskell, *Introduction to Metallurgical Thermodynamics*; Hemisphere Publishing: New York, 1973, p. 273.

Chapter 4
Brownmillerite-Perovskite
Intergrowths

4. BROWNMILLERITE-PEROVSKITE INTERGROWTHS

Based on the initial results by Goodenough and co-workers described in Chapter 2,[1,2] the brownmillerite-perovskite series seemed worthy of further investigation. At this point, only one intergrowth combination, $(BaInO_{2.5})(BaMO_3)$, had been studied. Several permutations of these materials could be used to study trends in oxygen ion conduction. For example, the number of vacancies in these materials can be controlled by changing the ratio of brownmillerite to perovskite units, while changing the metal on a specific site can change the lattice parameters and have an effect on metal and oxygen vacancy ordering. Substitutions were made for all three metals in the intergrowth system to give the new series $(AMO_{2.5})_x(AM'O_3)_y$, (A = Ca, Sr, or Ba; M = Al, Ga, Sc, or In; M' = Ti, Zr, or Hf).[3] Relative ratios, x to y, of 2:2, 2:1, 3:1, and 4:1 were prepared for various combinations of the cations. In all cases the A cation was the same in both components of the intergrowth.

4.1 Synthesis

All materials that were successfully prepared had to be heated above 1200 °C. Below this temperature little reaction occurred, as observed by powder XRD. In choosing appropriate temperatures for sample preparation several factors were considered. Higher temperatures generally yielded a material which appeared to be a solid solution by X-ray diffraction, while at slightly lower temperatures, some ordering could be observed. The temperature range in which an ordered material forms seems to be relatively narrow (about 50 °C), and the materials generally decompose if heated at slightly lower temperatures (1200 to 1250 °C for most samples) for extended periods of time. Once formed, the materials show no evidence of

decomposition when heated at temperatures below 1000 °C. However, these materials were generally sensitive to atmospheric conditions, most likely moisture, and pellets were found to crack or crumble over a period of a few days to a few weeks if exposed to air. Although materials of high theoretical density (the measured density of a pellet versus the crystallographic density) are generally desired for conductivity measurements, few of these materials could be prepared with densities significantly greater than 65 percent of the theoretical density.

Although many of these compounds were successfully prepared, a number of these materials proved difficult to make. All gallium-containing samples were found to be low-melting (below 1300 °C), and no single-phased materials were found in these systems. The synthesis of all aluminum samples was equally unsuccessful. Since $Ca_2Al_2O_5$ has not previously been reported, it seems this lattice site is too large for aluminum. However, materials such as $Ba_3Sc_2TiO_8$ could be made even though $Ba_2Sc_2O_5$ is not especially stable and is known to decompose above 1000 °C. To start this study, it would have been desirable to study all of the $A_2M_2O_5$ compounds; however, $Ba_2In_2O_5$ appears to be the only one of these compositions to form a stable crystalline phase which can be sintered and whose ionic conductivity can be measured. It was found that $Ba_2Sc_2O_5$ could be prepared only as a fine powder, while $Sr_2Sc_2O_5$ and $Sr_2In_2O_5$ could not be prepared at all. In general it was easier to form these solid solutions with barium than with strontium. No single-phased materials were made with calcium. This is most likely due to the smaller size of calcium. In general it was easier to make the brownmillerite-perovskite intergrowths with titanium than with zirconium or hafnium, and with indium rather than scandium, gallium or aluminum.

4.2 X-ray Diffraction

X-ray diffraction measurements established that most of these perovskite-brownmillerite intergrowths crystallize in the cubic perovskite structure, ABO_3. This corresponds to a disordering of the M and M' cations on the B site. Lattice parameters for materials showing cubic symmetry are listed in Table 4.1. The formulas for these materials are also listed as solid solutions to permit easy comparisons of their oxygen contents and vacancy concentrations. Although slight ordering was observed in some of these materials, no well-behaved, ordered intergrowths were found. However, even in the disordered solid solutions, some "superstructure" peaks were occasionally observed. In particular, a low intensity peak with a d-spacing of √2 times the cubic lattice parameter was observed in many materials. This could be due to oxygen ordering or partial ordering of the M and M' cations. If full ordering of these cations were achieved, superstructure peaks should have been much more intense than those that were observed. The X-ray diffraction patterns of $Ba_3In_2TiO_8$ and $Ba_3Sc_2TiO_8$ are shown in Figures 4.1 and 4.2 along with their Rietveld refinement patterns. The XRD patterns shown in Figures 4.1 and 4.2 have been refined as a disordered solid solution by Rietveld refinement using the GSAS[4] refinement package. The conditions and results of the Rietveld refinements are listed in Tables 4.2 and 4.3.

4.3 Conductivity

Although complex impedance can ideally separate out grain boundary and bulk effects, this was seldom observed in these samples and may be due to the low sample density. The Cole-Cole plot for $Ba_3In_2TiO_8$ at 200 °C is shown in Figure 4.3. The plot shows a single semicircle for the combined

Table 4.1 Lattice parameters for brownmillerite-perovskite intergrowths

Compound	Solid solution formula	a, cubic lattice parameter (Å)
$Sr_3In_2ZrO_8$	$SrIn_{0.67}Zr_{0.33}O_{2.67}$	4.066(1)
$Sr_4In_2Zr_2O_{11}$	$SrIn_{0.5}Zr_{0.5}O_{2.75}$	4.065(2)
$Sr_4In_3ZrO_{10.5}$	$SrIn_{0.75}Zr_{0.25}O_{2.625}$	4.048(2)
$Sr_5In_4ZrO_{13}$	$SrIn_{0.8}Zr_{0.2}O_{2.60}$	4.040(3)
$Sr_3In_2HfO_8$	$SrIn_{0.67}Hf_{0.33}O_{2.67}$	4.102(1)
$Sr_4In_2Hf_2O_{11}$	$SrIn_{0.5}Hf_{0.5}O_{2.75}$	4.101(1)
$Ba_3In_2TiO_8$	$BaIn_{0.67}Ti_{0.33}O_{2.67}$	4.19520(7)[*]
$Ba_4In_2Ti_2O_{11}$	$BaIn_{0.5}Ti_{0.5}O_{2.75}$	4.1258(4)
$Ba_3Sc_2TiO_8$	$BaSc_{0.67}Ti_{0.33}O_{2.67}$	4.15531(5)[*]
$Ba_3In_2HfO_8$	$BaIn_{0.67}Hf_{0.33}O_{2.67}$	4.224(1)

[*]from Rietveld analysis
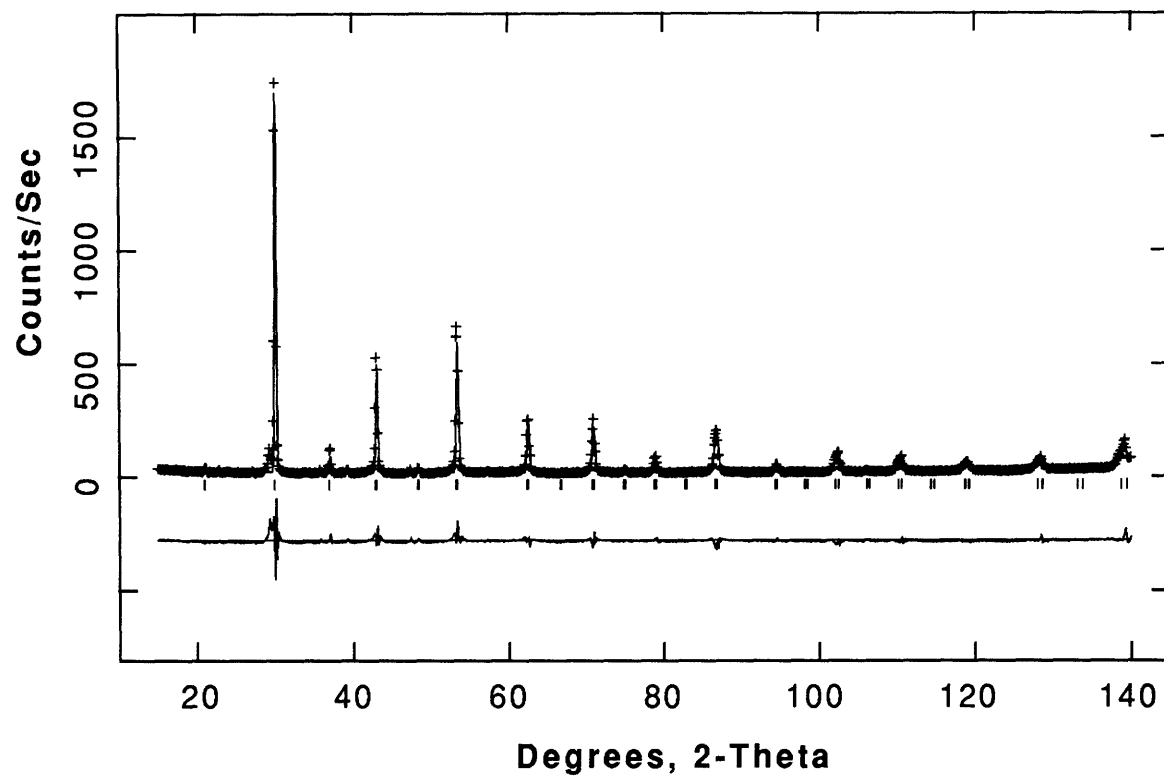
Figure 4.1 Rietveld refinement of the XRD pattern for $Ba_3In_2TiO_8$ showing the observed (crosses), calculated (line), and difference (bottom line) plots.
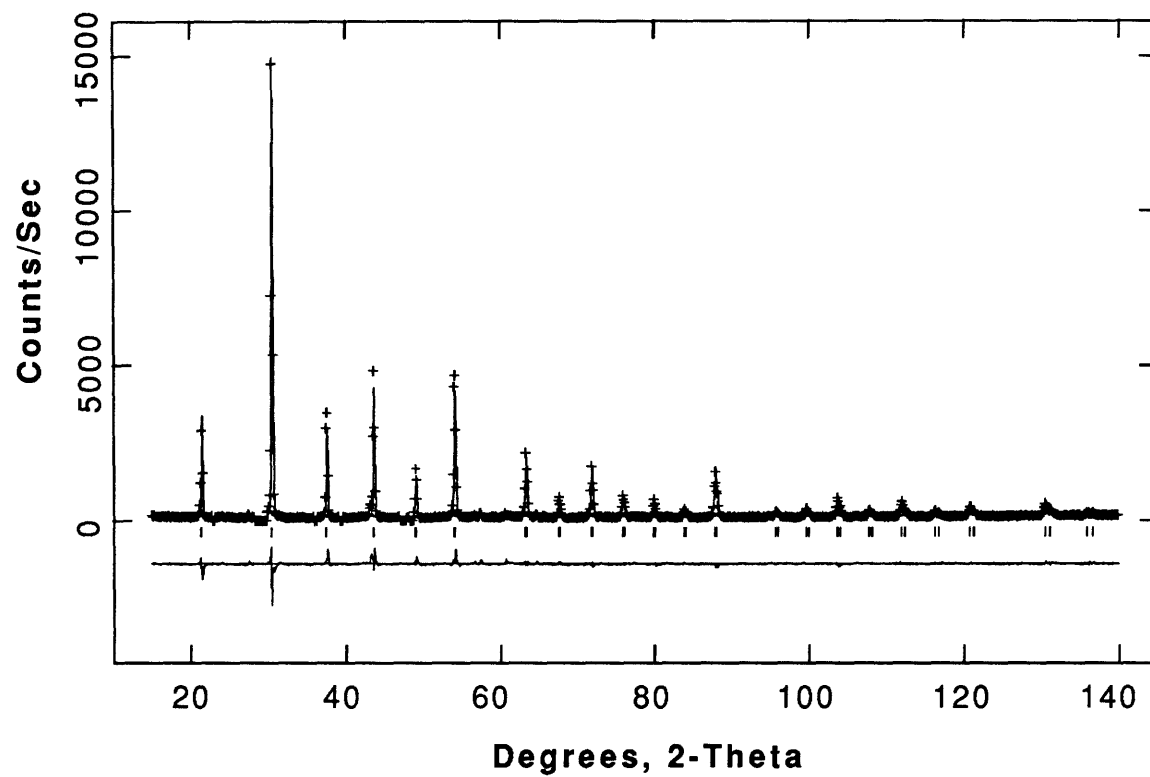
Figure 4.2 Rietveld refinement of the XRD pattern for $Ba_3Sc_2TiO_8$ showing the observed (crosses), calculated (line), and difference (bottom line) plots.

Table 4.2 Rietveld refinement data for powder XRD of $Ba_3In_2TiO_8$

Formula	$BaIn_{0.67}Ti_{0.33}O_{2.67}$
Space Group	$Pm\bar{3}m$
a, Å	4.19520(7)
Z	1
λ, Å	1.54059
2θ scan range (°)	15-140
Step Interval (°2θ)	0.01
Number of unique reflections	56
Number of structural parameters (including lattice parameters and thermal parameters)	4
Number of background parameters	6
Number of profile parameters	6
R_{wp}	12.6
R_{exp}	9.4
Goodness of Fit (R_{wp}/R_{exp})	1.34

	x	y	z	occupancy
Ba	1/2	1/2	1/2	1
In	0	0	0	0.66667
Ti	0	0	0	0.33333
O	1/2	0	0	0.88889

Table 4.3 Rietveld refinement data for powder XRD of $Ba_3Sc_2TiO_8$

Formula	$BaSc_{0.67}Ti_{0.33}O_{2.67}$
Space Group	$Pm\bar{3}m$
a, Å	4.15531(5)
Z	1
λ, Å	1.54059
2θ scan range (°)	15-140
Step Interval (°2θ)	0.01
Number of unique reflections	56
Number of structural parameters (including lattice parameters and thermal parameters)	6
Number of background parameters	6
Number of profile parameters	8
R_{wp}	12.7
R_{exp}	7.7
Goodness of Fit (R_{wp}/R_{exp})	1.65

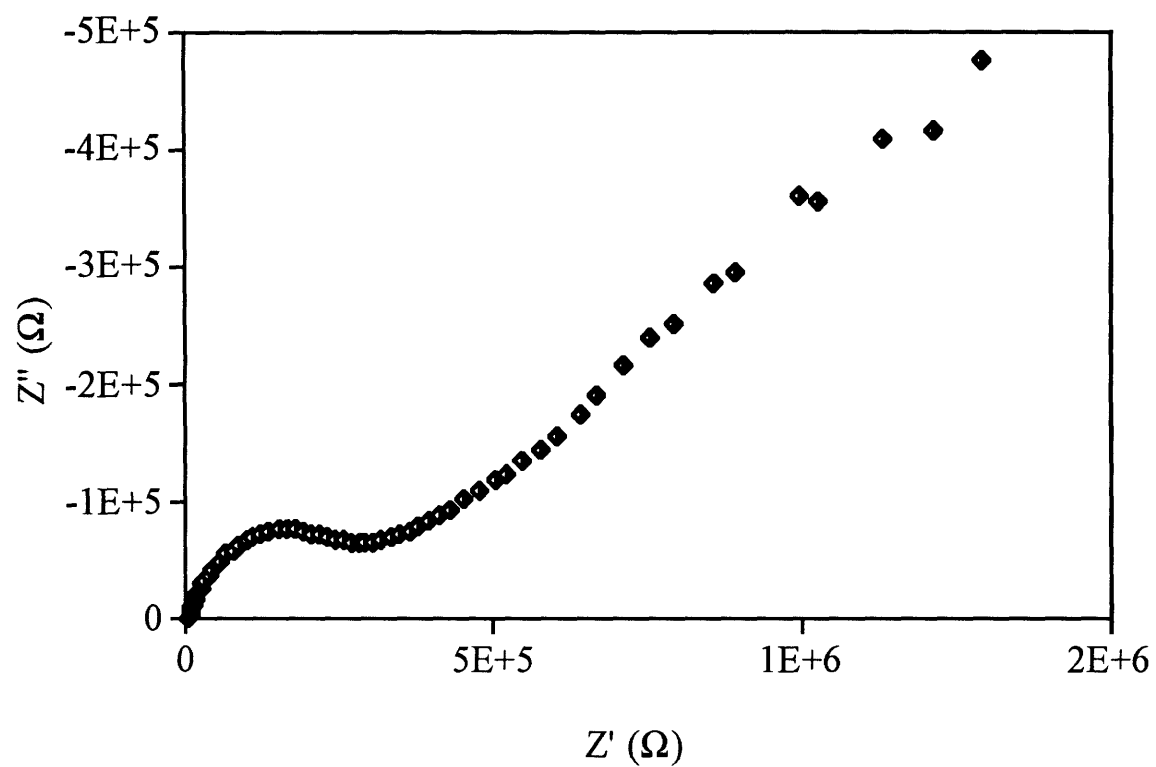|	x	y	z	occupancy
Ba	1/2	1/2	1/2	1
In	0	0	0	0.66667
Sc	0	0	0	0.33333
O	1/2	0	0	0.88889

Figure 4.3 A Cole-Cole plot for $Ba_3In_2TiO_8$ at 200 °C shows a single arc for grain boundary and bulk resistances and a large arc for the electrode.

bulk and grain boundary resistances and a much larger arc for the electrode. The assignment of these features was achieved by using different sample thicknesses. Since the electrode is not affected by the sample thickness, the portion of the plot which does not change can be attributed to the electrode. With increasing temperatures, the relative size of the arcs changes. A typical high temperature plot, that of $Sr_4In_3ZrO_{10.5}$ at 900 °C, is shown in Figure 4.4. In this case the bulk arc is no longer observed; however, it can be seen that the bulk and grain boundary resistances are of comparable magnitudes, about 2000 Ω.

Some typical Arrhenius plots are shown in Figures 4.5 through 4.8. Figure 4.5 shows the behavior of $Sr_4In_2HfO_{11}$. This compound had a rather low conductivity (2×10^{-4} S cm^{-1} at 900 °C) with a low activation energy (0.52 eV). Its conductivity behavior could be readily fit to a linear plot of log conductivity versus reciprocal temperature. Figure 4.6 shows the temperature dependence of the conductivity of $Sr_4In_2Zr_2O_{11}$. This material also exhibited linear Arrhenius behavior and a low activation energy of 0.48 eV for the bulk material. To compare $Sr_4In_2Zr_2O_{11}$ to $Sr_4In_2Hf_2O_{11}$, however, the activation energy for the total conductivity of $Sr_4In_2Zr_2O_{11}$, 1.20 eV, must be used. Thus the activation energy increases significantly in moving from Hf to Zr, which may be related to the size difference between Zr and Hf ions. The conductivity of $Sr_4In_2Zr_2O_{11}$ is less than that of $Sr_4In_2Hf_2O_{11}$ at all measured temperatures. The temperature dependence for the conductivity of $Sr_3In_2HfO_8$ is illustrated in Figure 4.7. This conductivity exhibits nonlinear behavior. From previous research on $Ba_3In_2ZrO_8$ it would seem possible that there are two conduction processes here: protonic conduction at low temperature and oxygen ion conduction at higher temperatures. Several other materials display this behavior in greater or
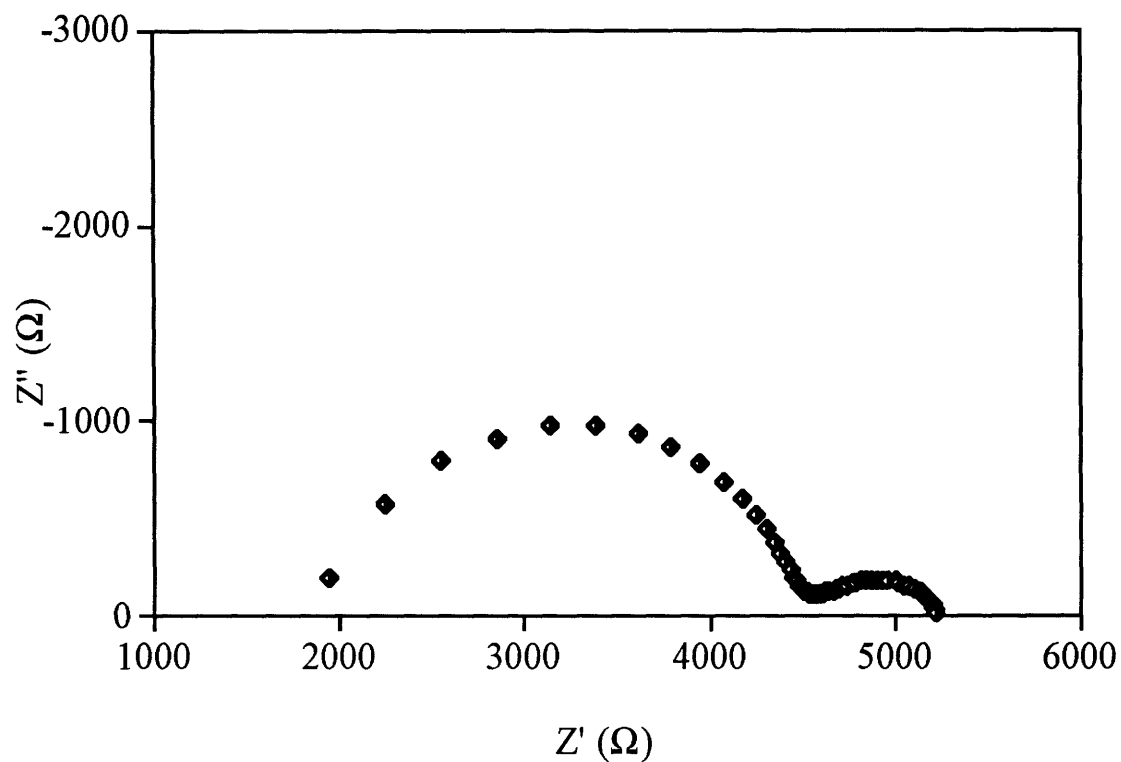
Figure 4.4 Cole-Cole plot for $Sr_4In_3ZrO_{10.5}$ at 900 °C, showing a single arc for the grain boundary conductivity process and a second small arc for the electrode. The bulk conductivity process cannot be observed at this temperature, but its magnitude is calculated as the left intercept of the grain boundary process.
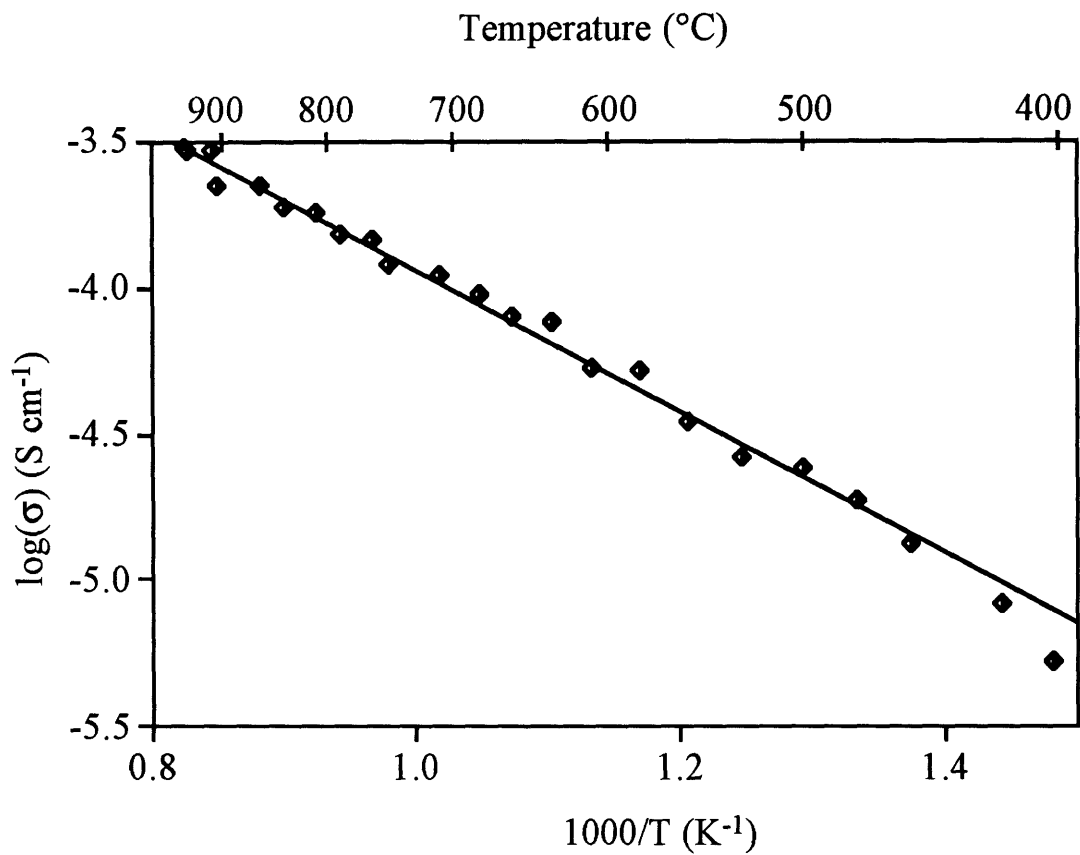
Figure 4.5 A plot of log conductivity of $Sr_4In_2Hf_2O_{11}$ versus $1/T$ exhibits a linear Arrhenius behavior with an activation energy of 0.52 eV.
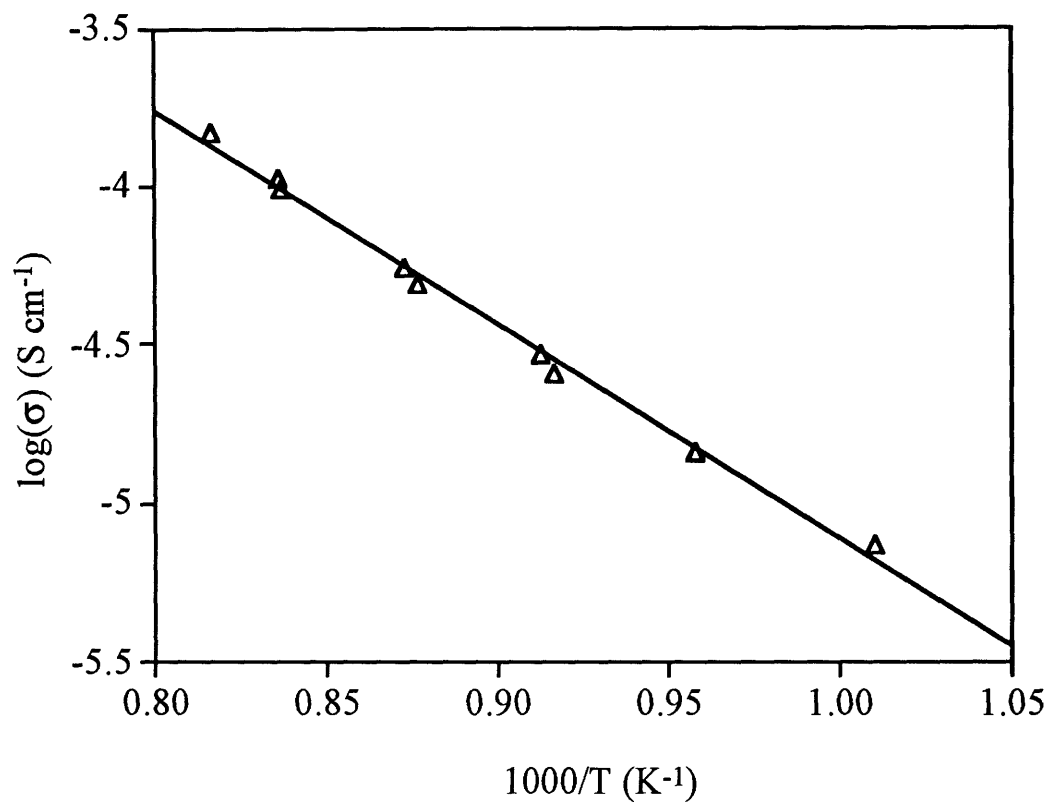
Figure 4.6 A plot of log conductivity versus 1000/T for the bulk conductivity of $Sr_4In_2Zr_2O_{11}$ exhibits linear Arrhenius behavior with an activation of 0.48 eV.
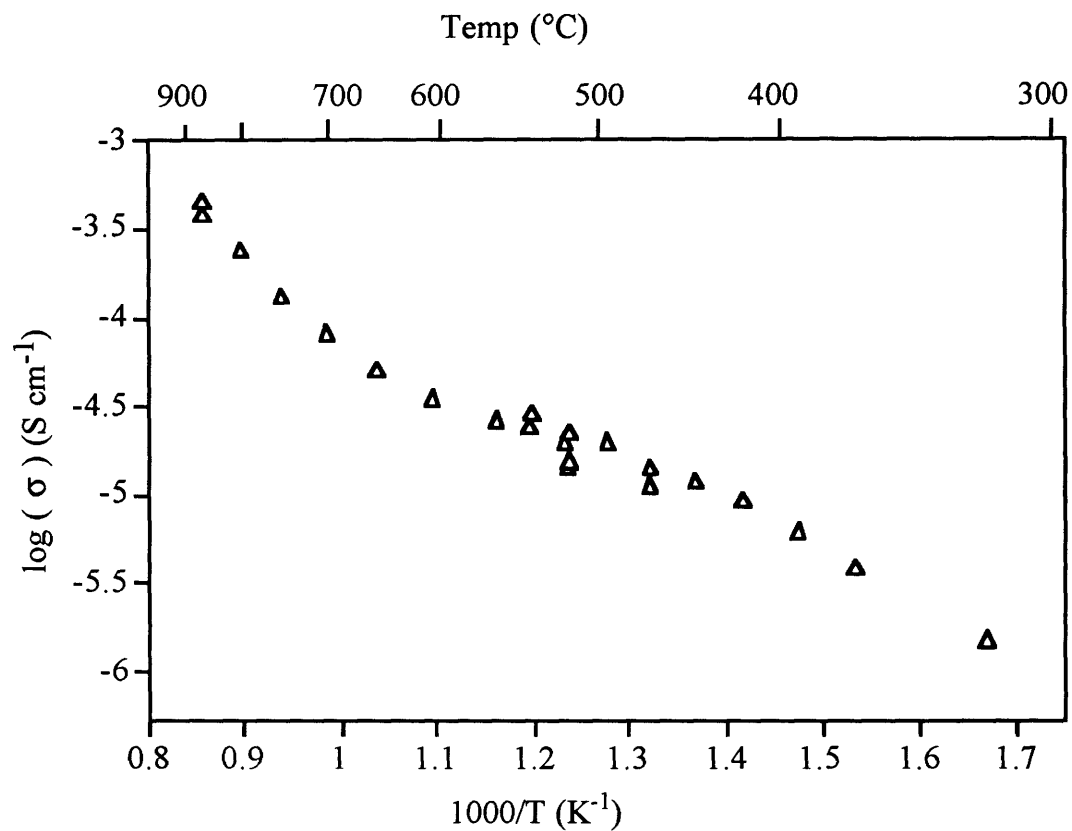
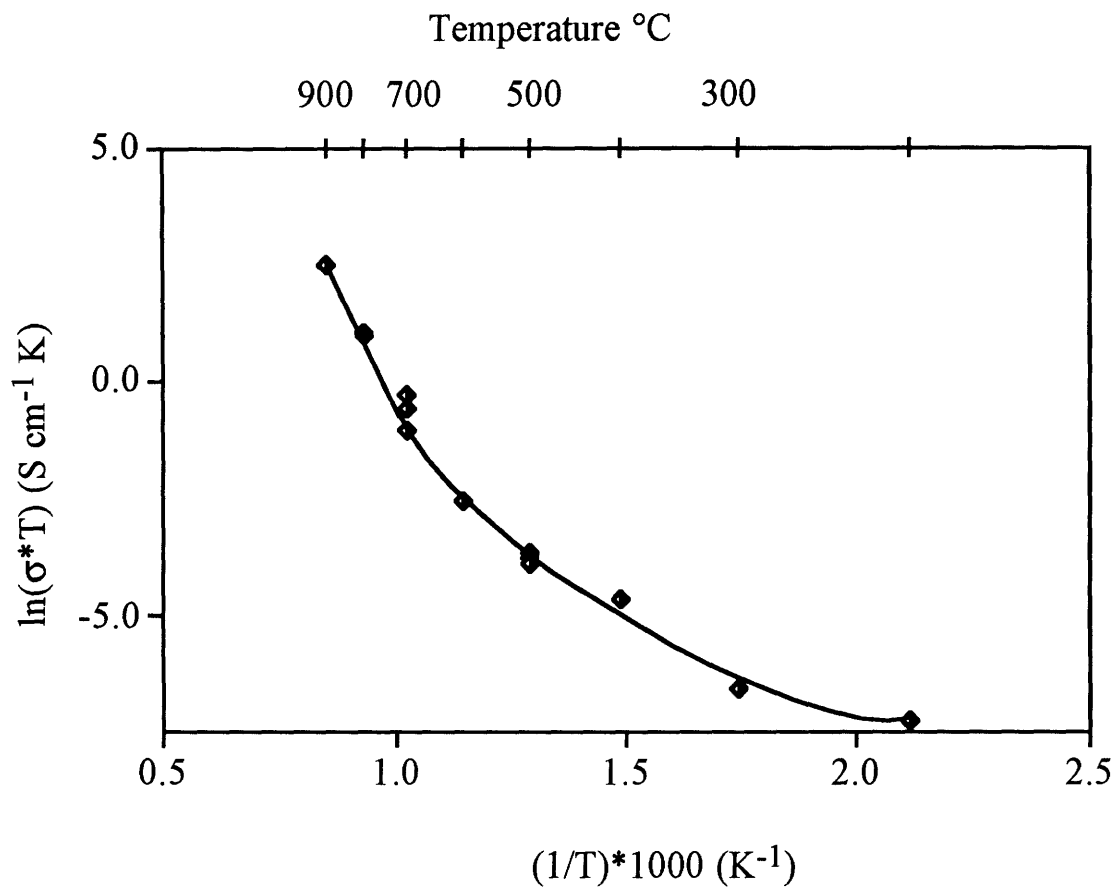Figure 4.7 Log conductivity versus 1000/T for $Sr_3In_2HfO_8$. A change in activation energy is observed.

Figure 4.8 An Arrhenius plot of bulk conductivity for Ba₃In₂TiO₈ displays significant curvature.

lesser degrees. $Ba_3In_2TiO_8$, for instance, also exhibited nonlinear Arrhenius behavior (Figure 4.8). Since this material was among the easiest to synthesize, it was used for several other studies including the measurements of protonic conductivity. Total conductivities and activation energies for the studied materials are listed in Table 4.4.

Using the lattice parameters obtained from X-ray diffraction measurements and Shannon's radii,[5] the "free volume" in the sample can be calculated. The free volumeswere calculated for the simple cubic unit cells listed in Table 4.1 and correlated to conductivities and activation energies. A plot of activation energy versus free volume is shown in Figure 4.9. Clusters of the materials containing the same elements can be observed in this plot. No overall trend is observed to describe the behavior in the clusters; however, for either A cation (Sr or Ba) the clusters with higher free volumes had lower activation energies. All compositions in the Sr-In-Zr series had higher activation energies than all compounds in the Sr-In-Hf series, and Ba-Sc-Ti and Ba-In-Ti containing samples had higher activation energies than Ba-In-Hf containing samples. The relationship between materials such as $Sr_3In_2HfO_8$ and $Ba_3In_2HfO_8$ is not clear in this plot. They have very different free volumes, but similar activation energies. Some trend in free volumes appears to be present, but it is not clear which alterations to a material would give a change in activation energy with a change in the free volume. From the data collected here, however, modifications in a material that change the free volume only slightly change the activation energy the most.

A plot of high temperature conductivity (900 °C) versus free volume is shown in Figure 4.10. This is somewhat more predictive as there is basically a

Table 4.4 Conductivities and activation energies of brownmillerite-perovskite intergrowths.

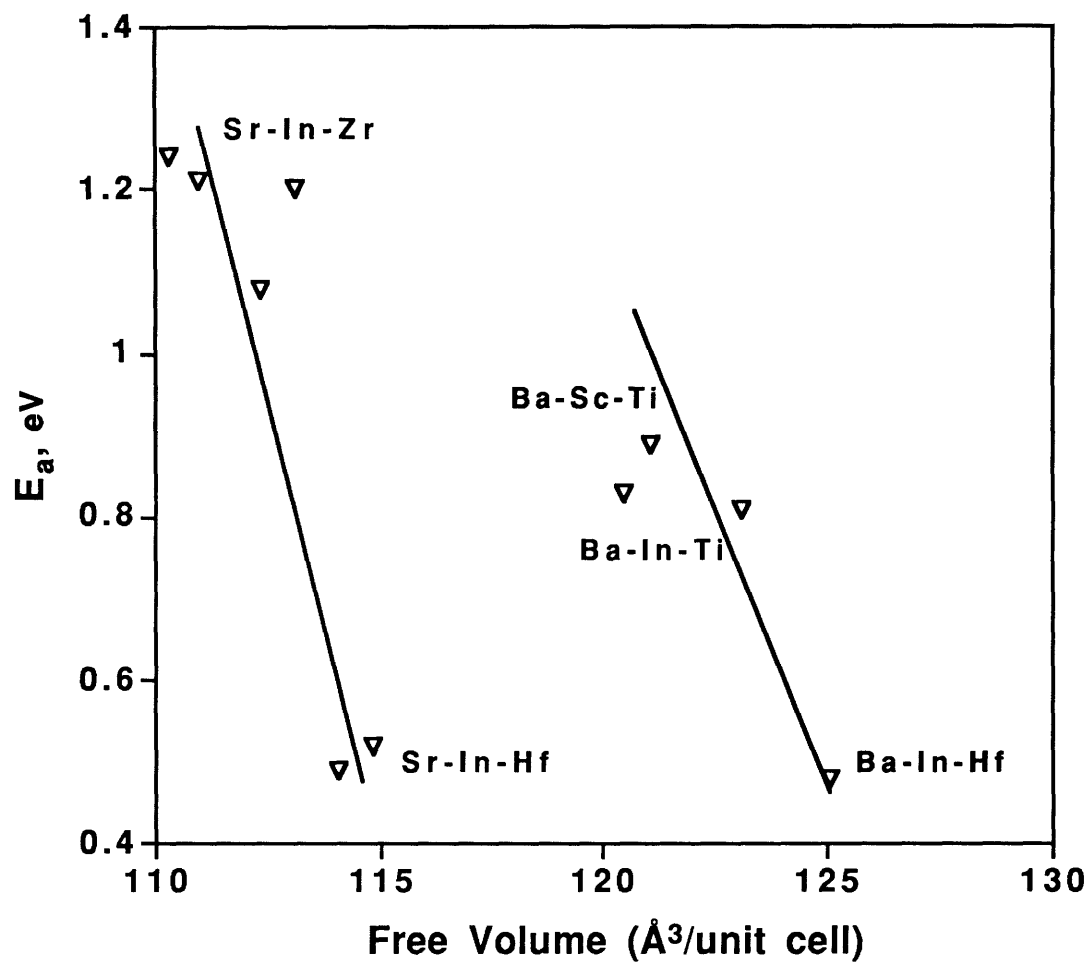| Compound	$\text{Log}(\sigma)$ at 500 °C	$\text{Log}(\sigma)$ at 900 °C	Activation energy (eV)
$Sr_3In_2ZrO_8$	-6.30	-3.87	1.08
$Sr_4In_2Zr_2O_{11}$	-6.46	-4.55	1.20
$Sr_4In_3ZrO_{10.5}$	-6.81	-4.27	1.21
$Sr_5In_4ZrO_{13}$	-6.93	-4.30	1.24
$Sr_3In_2HfO_8$	-5.38	-3.78	0.49
$Sr_4In_2Hf_2O_{11}$	-5.36	-3.66	0.52
$Ba_3In_2TiO_8$	-4.55	-2.92	0.81
$Ba_4In_2Ti_2O_{11}$	-4.90	-2.85	0.83
$Ba_3In_2HfO_8$	-3.82	-2.82	0.48
$Ba_3Sc_2TiO_8$	-4.99	-3.17	0.89

Figure 4.9 Activation energy versus free volume for studied brownmillerite-perovskite intergrowths.
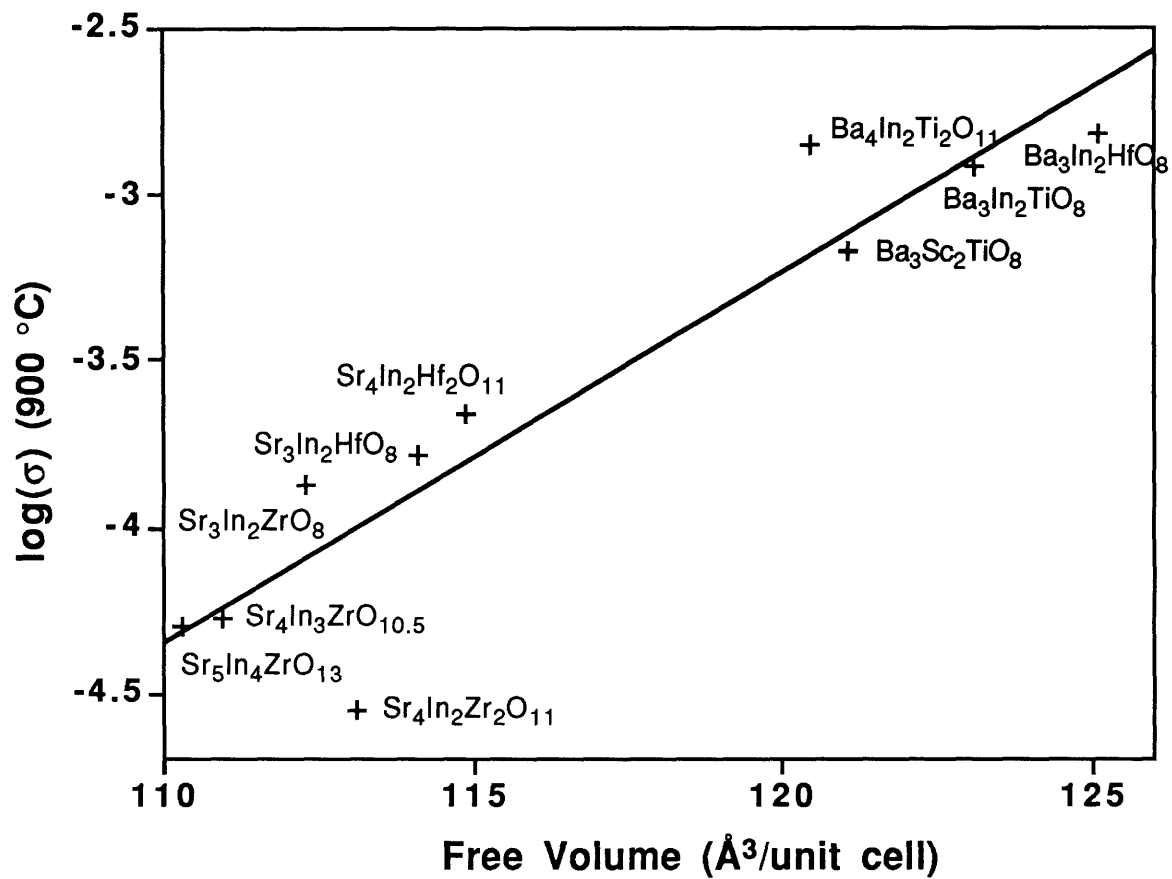
Figure 4.10 Log conductivity at 900 °C versus free volume for studied brownmillerite-perovskite materials.

linear relationship. Materials with larger free volumes have lower activation energies.

4.4 High Temperature Powder XRD

High temperature X-ray diffraction was used to investigate the behavior of $Ba_3In_2TiO_8$. Figure 4.11 shows a plot of the cubic lattice parameter versus temperature. This displays a general increase in the lattice parameter. No change in symmetry, however, was observed, suggesting that changes in long-range cation ordering are not responsible for the curvature in the Arrhenius plots. It is not apparent from these high temperature measurements that there exists any short-range cation order on the B site or any ordering of the oxygen vacancies.

4.5 Neutron Diffraction

Powder neutron diffraction was used to investigate the oxygen vacancy ordering in $Ba_3In_2TiO_8$ and $Ba_3Sc_2TiO_8$. The neutron diffraction patterns could be fit to the disordered cubic solid solution in space group $Pm\bar{3}m$. The refinements for $Ba_3In_2TiO_8$ and $Ba_3Sc_2TiO_8$ are shown in Figures 4.12 and 4.13, respectively. The specifics of the refinements are listed in Tables 4.5 and 4.6. The background for both samples is relatively high, which most likely indicates some amount of moisture present in the samples. Attempts to refine the oxygen content of these materials to model oxygen uptake in lattice sites were not positive. Increasing the occupancy of the oxygen site worsened rather than improving the fit.
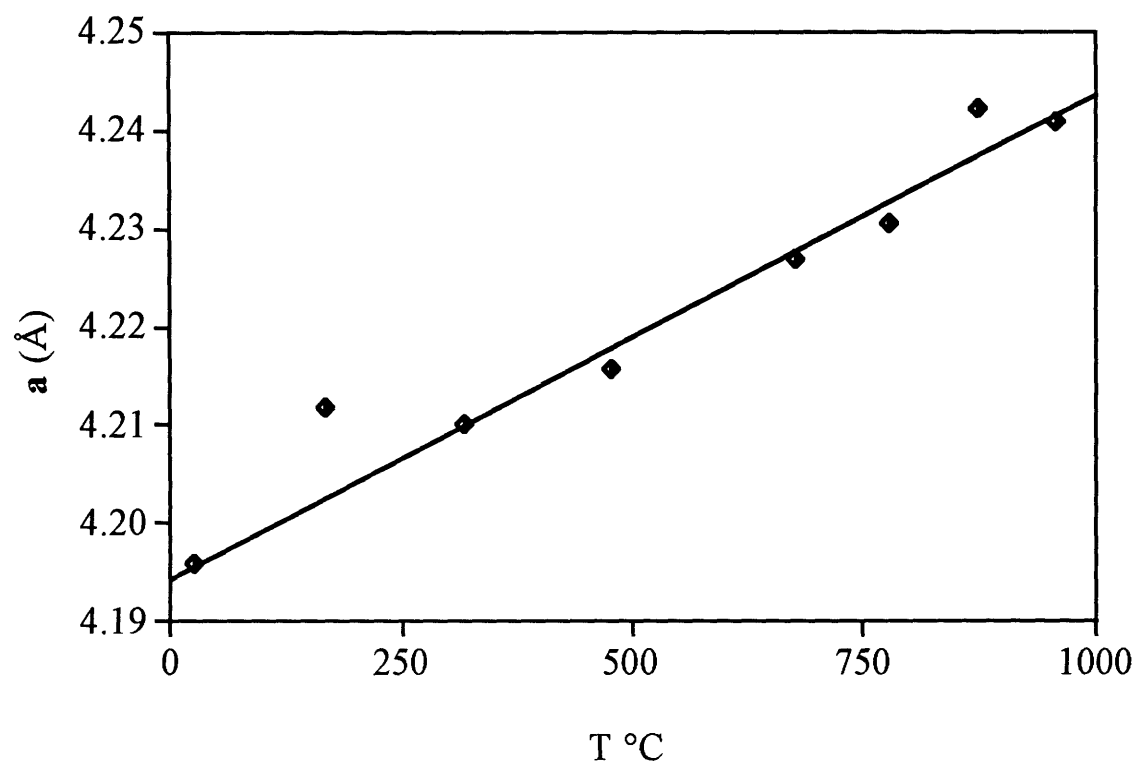
Figure 4.11 Cubic lattice parameter, a, versus temperature for $Ba_3In_2TiO_8$. Only an expansion in the lattice parameters was observed, no change in symmetry.
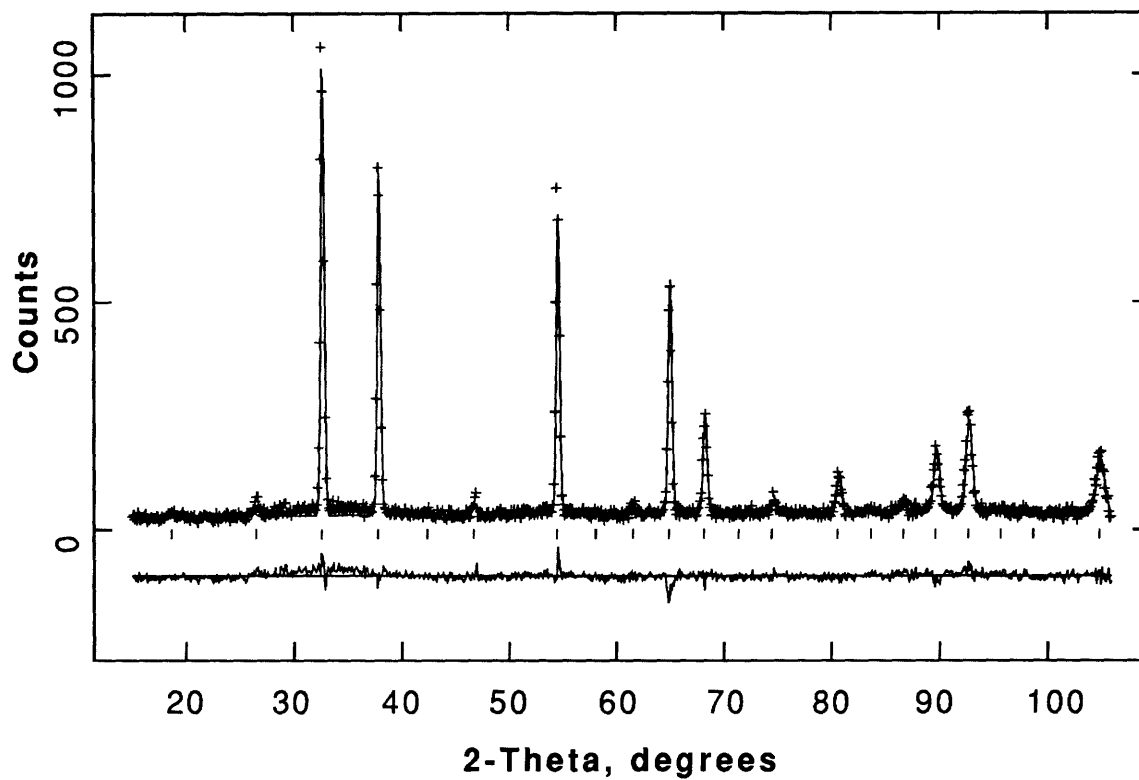
Figure 4.12 Rietveld refinement of the neutron diffraction pattern of $Ba_3In_2TiO_8$ showing the observed (crosses), calculated (line), and difference (bottom line) plots.
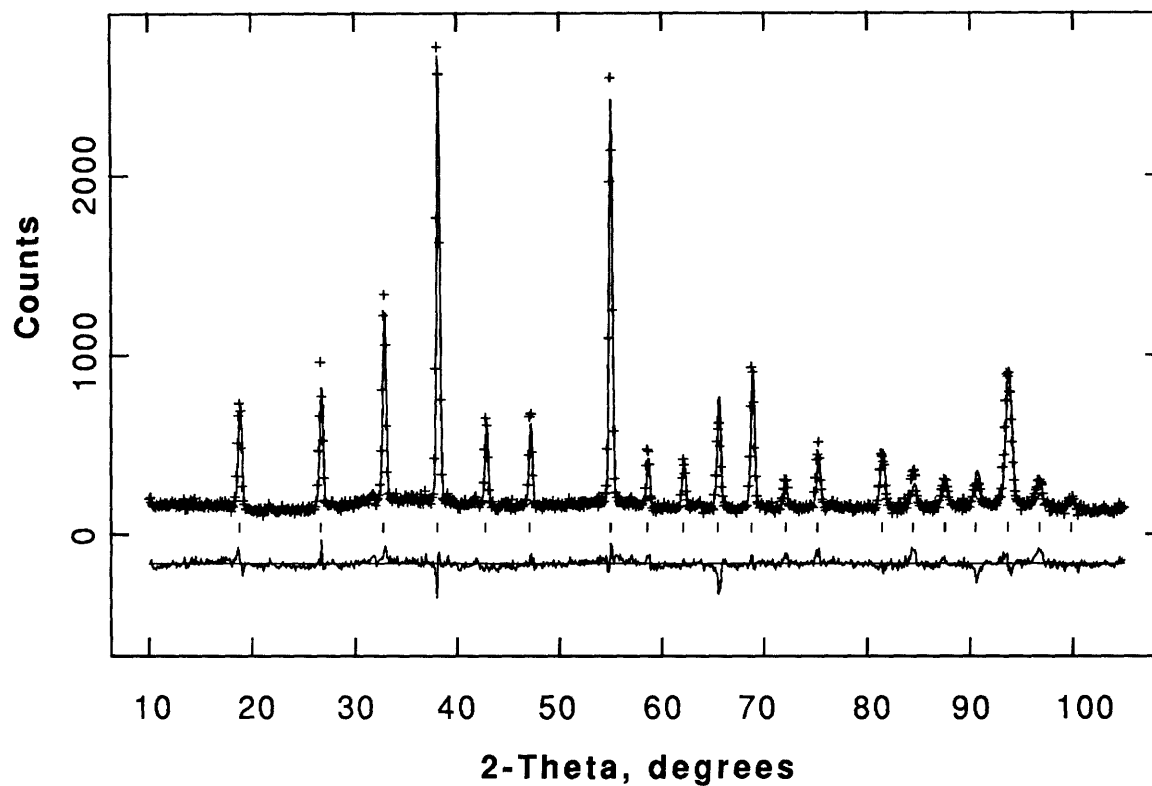
Figure 4.13 Rietveld refinement of the neutron diffraction pattern of $Ba_3Sc_2TiO_8$ showing the observed (crosses), calculated (line), and difference (bottom line) plots.

Table 4.5 Rietveld refinement data for powder neutron diffraction of $Ba_3In_2TiO_8$

| Formula	$BaIn_{0.67}Ti_{0.33}O_{2.67}$
Space Group	$Pm\bar{3}m$
a, Å	4.19520(7)
Z	1
λ, Å	1.356
2θ scan range (°)	15-105
Step Interval (°2θ)	0.1
Number of unique reflections	26
Number of structural parameters (including lattice parameters and thermal parameters)	4
Number of background parameters	6
Number of profile parameters	6
R_{wp}	19.3
R_{exp}	13.4
Goodness of Fit (R_{wp}/R_{exp})	1.44

	x	y	z	occupancy
Ba	1/2	1/2	1/2	1
In	0	0	0	0.66667
Ti	0	0	0	0.33333
O	1/2	0	0	0.88889

Table 4.6 Rietveld refinement data for powder neutron diffraction of $Ba_3Sc_2TiO_8$

Formula	$BaSc_{0.67}Ti_{0.33}O_{2.67}$
Space Group	$Pm\bar{3}m$
a, Å	4.15531(5)
Z	1
λ, Å	1.356
2θ scan range (°)	10-105
Step Interval (°2θ)	0.1
Number of unique reflections	23
Number of structural parameters (including lattice parameters and thermal parameters)	4
Number of background parameters	12
Number of profile parameters	6
R_{wp}	10.5
R_{exp}	6.8
Goodness of Fit (R_{wp}/R_{exp})	1.54

	$\underline{x}$	$\underline{y}$	$\underline{z}$	occupancy
Ba	1/2	1/2	1/2	1
Sc	0	0	0	0.66667
Ti	0	0	0	0.33333
O	1/2	0	0	0.88889

4.6 Thermogravimetric Analysis

TGA measurements were used to determine if there were any weight loss in the samples during heating, to indicate, for example, loss of absorbed water or loss of oxygen due to sample reduction. $Ba_3In_2TiO_8$ and $Ba_3Sc_2TiO_8$ were heated under forming gas (5% H_2/N_2), and a small weight loss was observed. Both samples exhibited about one percent weight loss (Figures 4.14 and 4.15), which corresponds to approximately half of an oxygen. This is in contrast with $Ba_3In_2ZrO_8$ which shows uptake or loss of weight corresponding to a whole oxygen on cooling and heating as mentioned in Chapter 2. It is possible that these samples could also undergo further weight uptake with time, as no special effort was made to increase the oxygen content. From these studies it can be concluded that some component, presumably H_2O or O_2, is being weakly adsorbed or intercalated into the material, although it is not clear how this affects the conductivity.

4.7 Measurements under Controlled Atmospheres

4.7.1 Measurements under Moisture-controlled Atmospheres

To investigate the effects of the weight uptake on the ionic conductivity and to investigate the possibility of protonic conduction in these samples, the conductivity of $Ba_3In_2TiO_8$ was measured under air, air dried over drierite, and air sparged through water. Plots of log conductivity versus 1000/T are shown in Figures 4.16 through 4.18. The same sample was used for all measurements. The sample was first heated under air, then dried air, and finally wet air. Under air a hysteresis was observed as the sample became more conductive after one heating cycle. This increase in conductivity was not reversed on heating in dried air. The high temperature regions of both
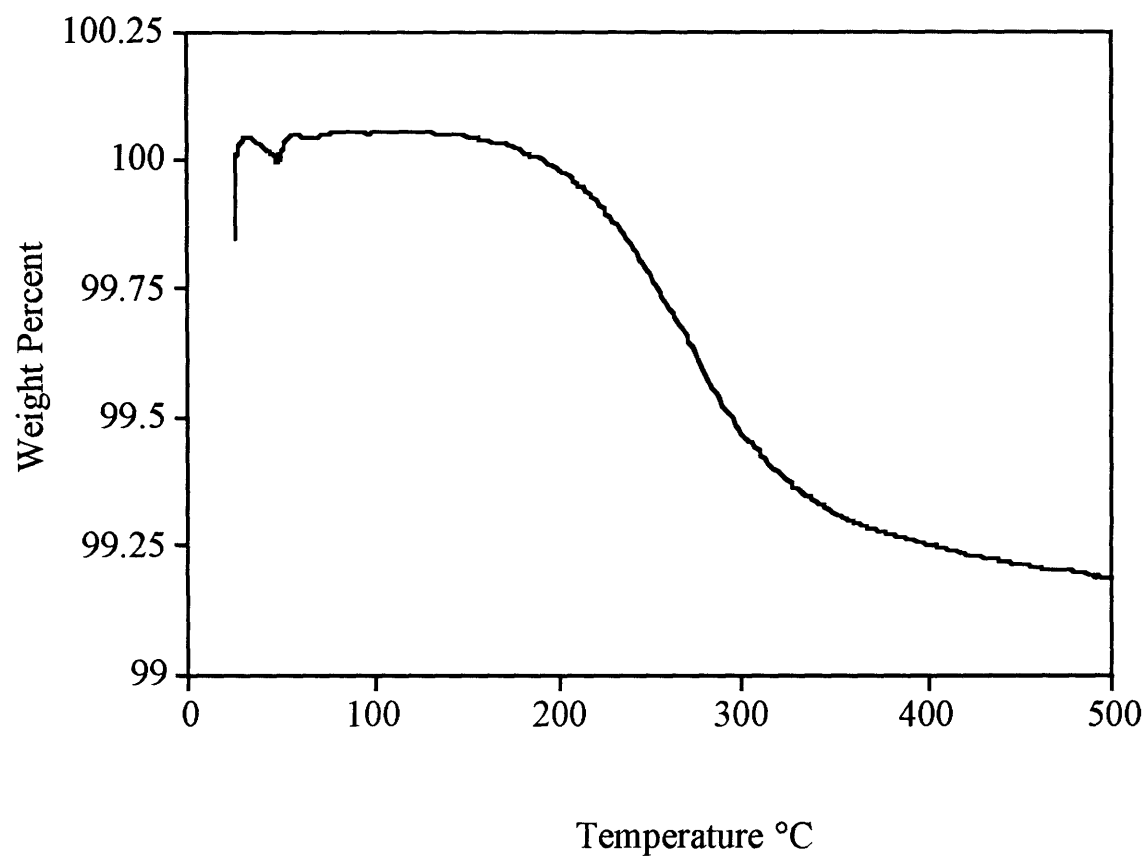
Figure 4.14 TGA of $Ba_3In_2TiO_8$ under H_2/N_2 shows a weight loss of about one percent.
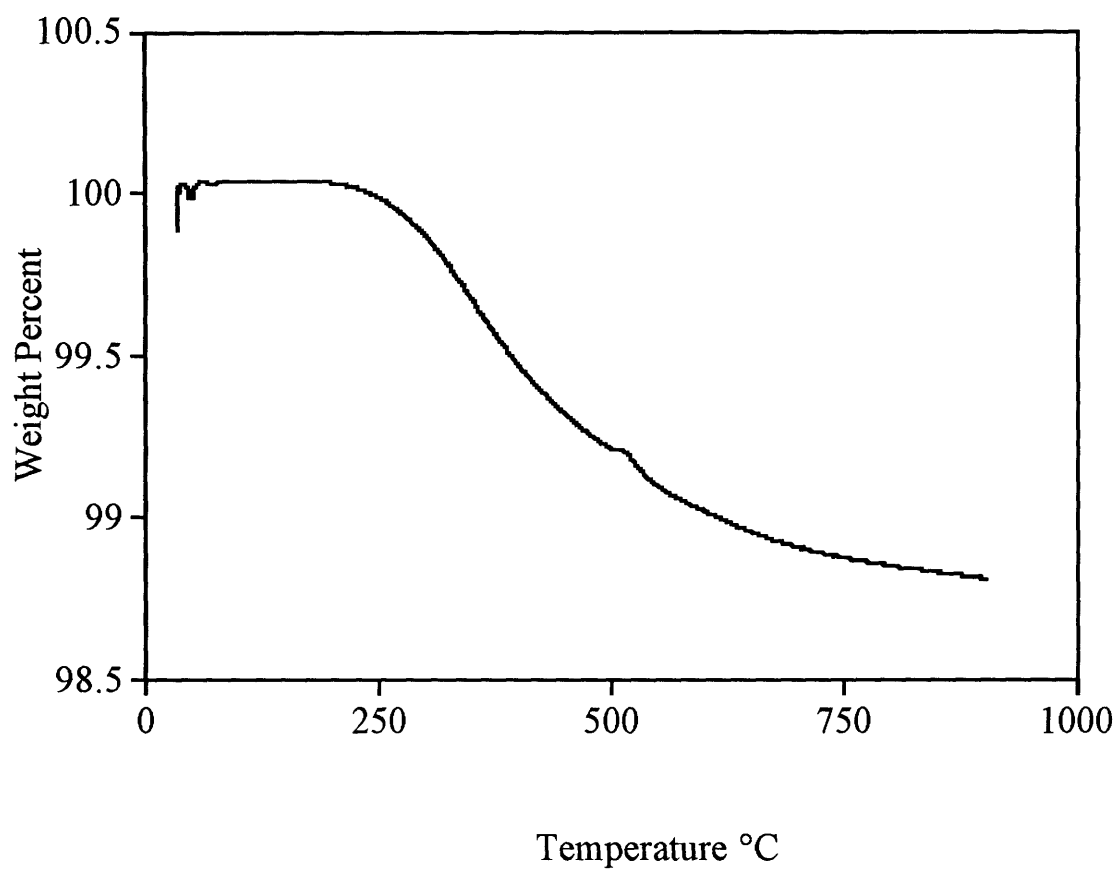
Figure 4.15 TGA of Ba₃Sc₂TiO₈ under H₂/N₂ shows a weight loss of about one percent.
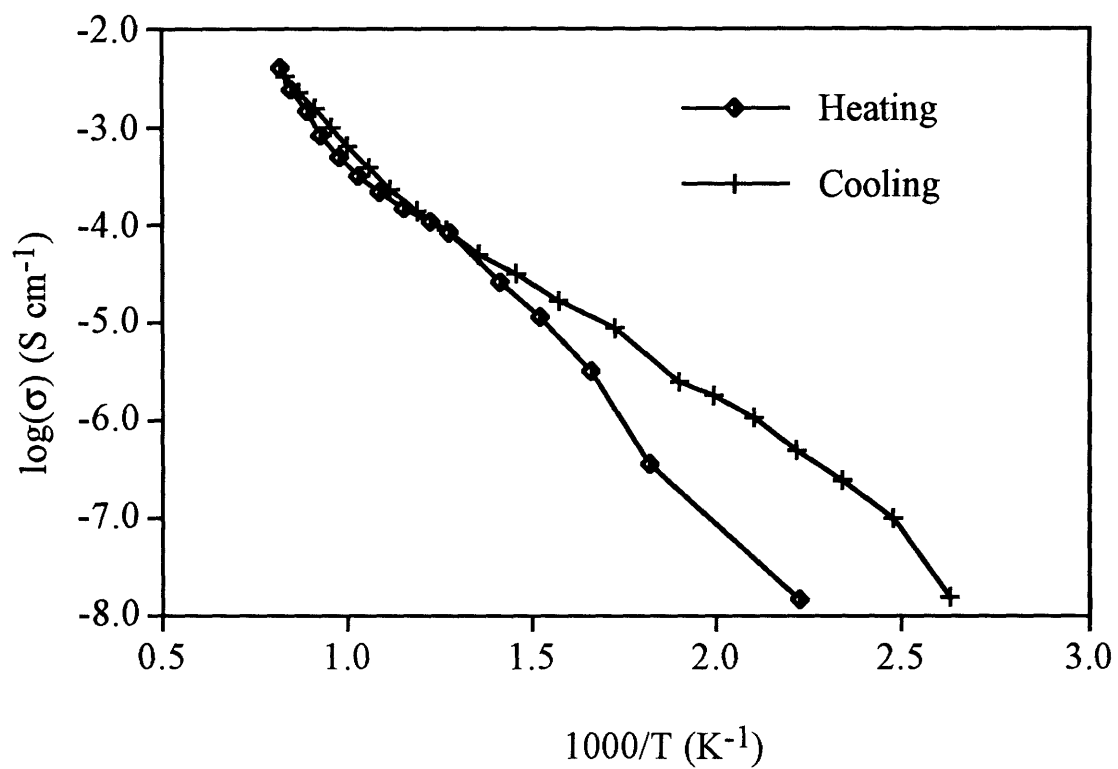
Figure 4.16 A plot of log conductivity versus 1/T for Ba₃In₂TiO₈ in air shows curvature on heating with a hysteresis on cooling.
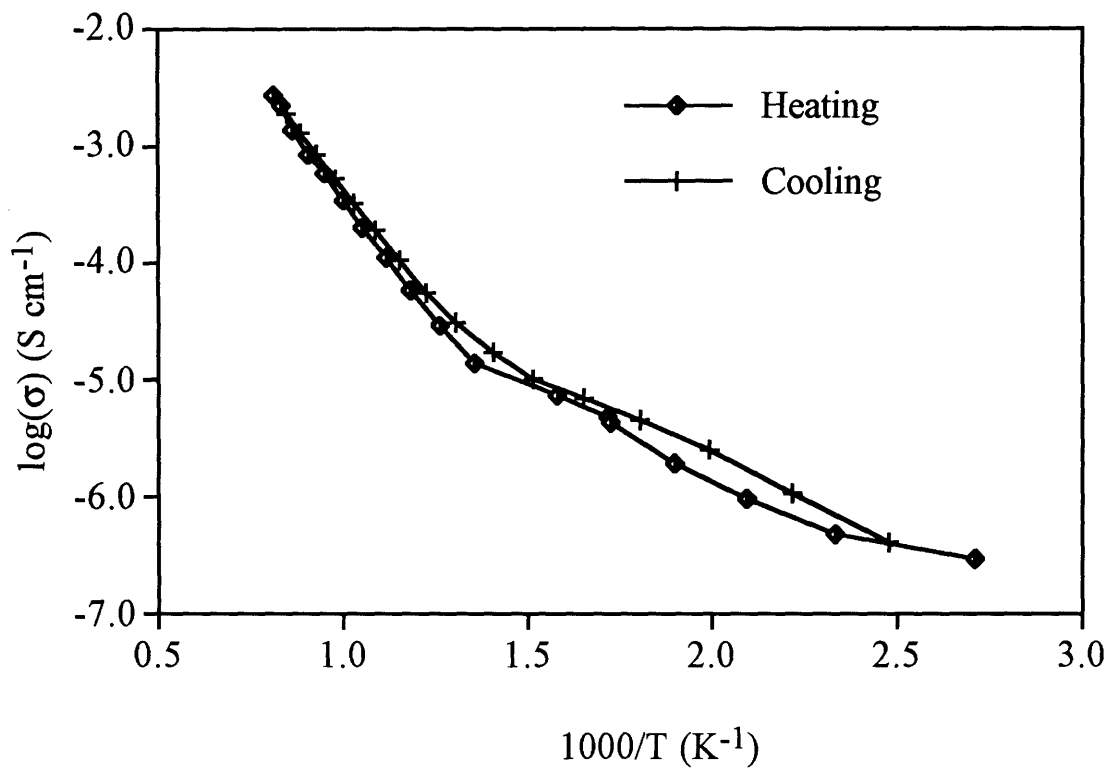
Figure 4.17 A plot of log conductivity versus 1/T for $Ba_3In_2TiO_8$ in dry air shows significant curvature, but is similar for heating and cooling.
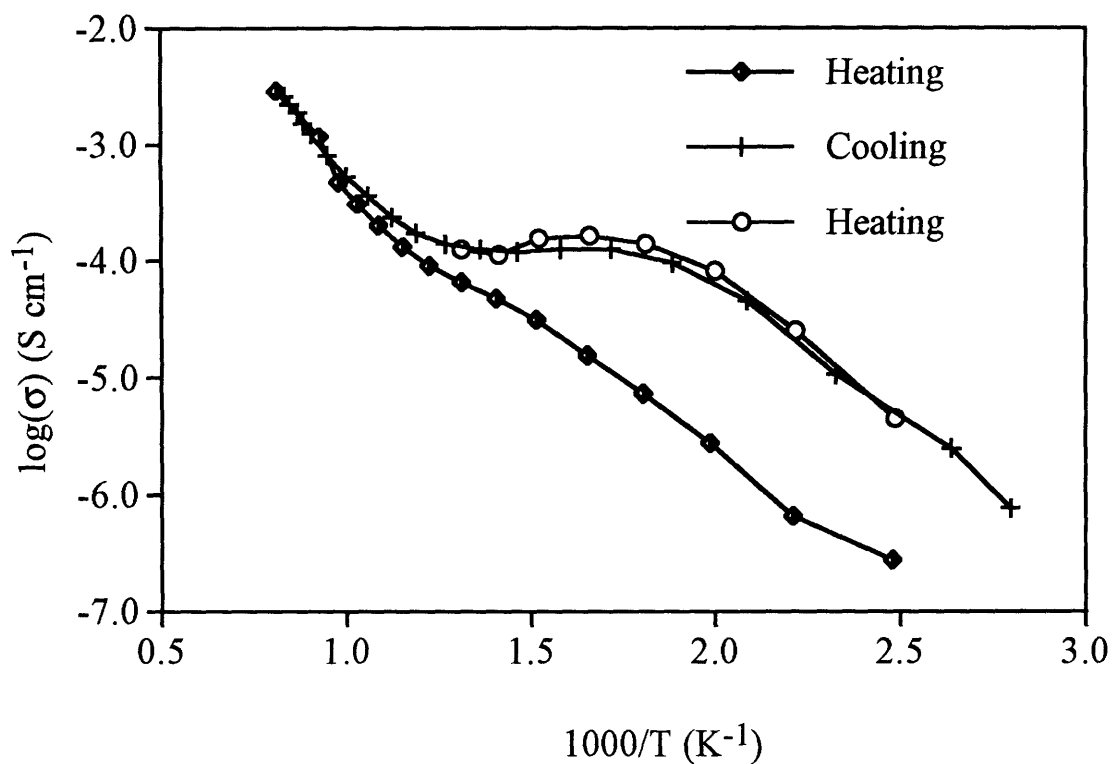
Figure 4.18 A plot of log conductivity versus 1/T for $Ba_3In_2TiO_8$ in moist air exhibits significant hysteresis. The initial heating cycle is similar to that observed in non-hydrated air, but, on cooling, a significantly higher conductivity is observed at low temperatures.

plots are nearly identical. The conductivity measured during the initial heating cycle under wet air was not significantly different from the two previous runs, but on cooling, the sample maintained a high conductivity. A plateau in conductivity was observed between 250 and 500 °C. A second linear region of conductivity is observed at low temperatures in wet air. This data is consistent with a sample exhibiting protonic conduction at low temperatures and oxygen ion conduction at higher temperatures. The low temperature protonic conductivity might be useful in high temperature pH sensors or other applications.

4.7.2 Measurements under Different Oxygen Partial Pressures

The conductivities of two samples were measured in atmospheres other than air. The conductivity of $Sr_4In_2ZrO_{11}$ was determined under air and nitrogen, and no change in conductivity or activation energy was observed between the two runs. This lack of conductivity dependence on oxygen partial pressure indicates that the sample is predominantly an ionic conductor in this range of oxygen partial pressure. $Ba_3Sc_2TiO_8$ was measured under a variety of different oxygen pressures, with slightly different results. A double log plot of conductivity versus oxygen partial pressure showed increasing conductivity for partial pressures greater than 10^{-10} atm (Figure 4.19). This increase in conductivity is consistent with p-type conductivity, and the high p_{O_2} region could be fit to a slope of 1/4. This indicates that at least for the titanium-containing samples there is significant electrical conductivity. This is most likely due to the uptake of a small amount of excess oxygen in the material. The oxygen donates electrons to the system, leading to an electronic component in the conductivity.
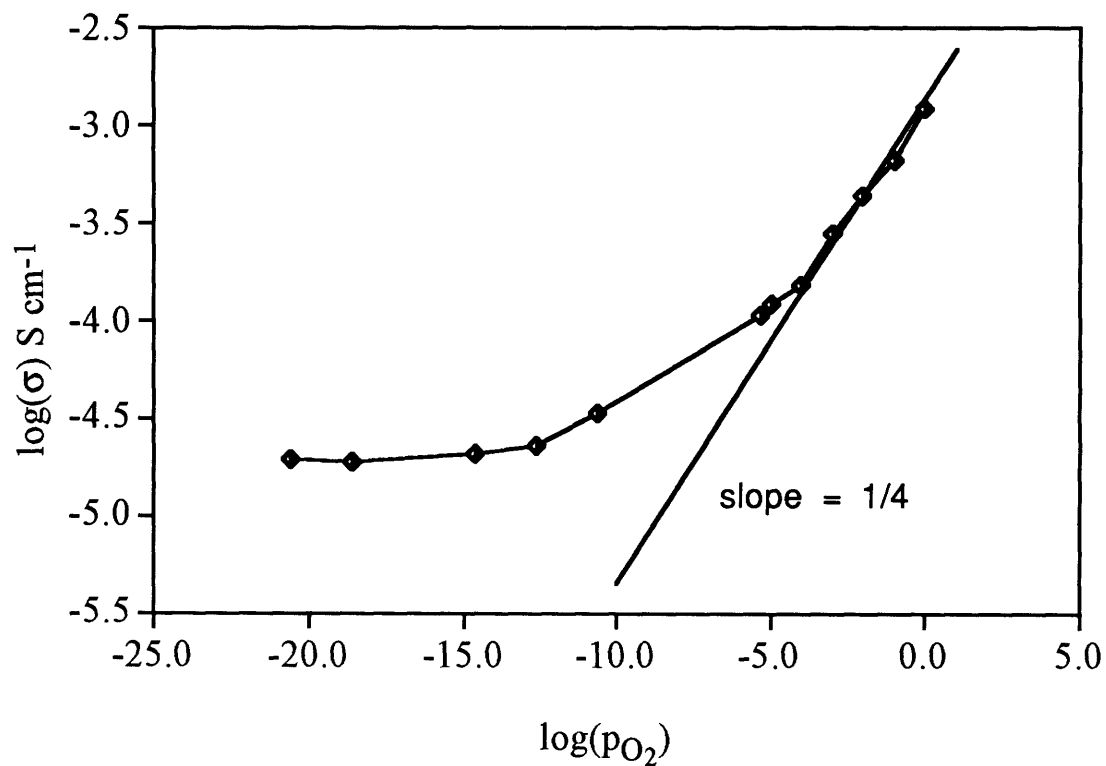
Figure 4.19 Log conductivity versus log oxygen partial pressure for $Ba_3Sc_2TiO_8$ at 800 °C. This displayed a decrease in conductivity at lower oxygen partial pressures. The slope of 1/4 is consistent with p-type conductivity.

4.8 Conclusions

These brownmillerite-perovskite solid-solutions show a wide range of behaviors. No exceptional oxygen ion conductors were found, although some of the activation energies are extremely low. The free volumes were found to correlate well with the high temperature conductivity, as well as with the activation energy. The activation energy, however, seemed to be most affected by specific cation changes, more so than volume changes, since activation energies for different ratios of a set of elements were generally similar. The low temperature protonic conductivity might be useful in high temperature pH sensors or other applications.

References

(1) Goodenough, J. B.; Ruiz-Diaz, J. E.; Zhen, Y. S., Oxide-ion conduction in $Ba_2In_2O_5$ and $Ba_3In_2MO_8$ (M = Ce, Hf, or Zr), **Solid State Ionics** (1990) 44, 21-31.

(2) Goodenough, J. B.; Zhen, Y. S., In *Solid State Ionics II*; G. A. Nazri, D. F. Shriver, R. A. Huggins and M. Balkanski, Ed.; "New Oxide-Ion Electrolytes", Materials Research Society: Pittsburgh, Pennsylvania, 1991, Vol. 210; pp 287-301.

(3) Thomas, J. K.; Krause, W. E.; zur Loye, H.-C., In *Solid State Ionics III*; J.-M. T. G.-A. Nazri M. Armand, Ed.; "Cation Ordering in Brownmillerite-perovskite Intergrowth Structures", Materials Research Society: Pittsburgh, Pennsylvania, 1993, Vol. 293; pp 307-313.

(4) "GSAS: General Structure Analysis System," Larson, A. C.; Von Dreele, R. B., Los Alamos National Laboratory, 1990

(5) Shannon, R. D.; Prewitt, C. T., Effective Ionic Radii in Oxides and Fluorides, **Acta Crystallogr. B-Struct. Sci.** (1969) 25, 925-946.

Chapter 5
Aurivillius-Brownmillerite
Intergrowths

5. AURIVILLIUS-BROWNMILLERITE INTERGROWTHS

From the brownmillerite-perovskite intergrowths described in the previous chapter, it was observed that the intergrowth approach was a viable route to achieve oxygen ion conduction. Since the Aurivillius type layered bismuth oxide materials are among the best low temperature oxygen ion conductors, we set out to modify these compounds through the use of intergrowths. It is known that perovskite layers could be added to some of these materials, for example $Bi_4Ti_3O_{12} + BaTiO_3 \rightarrow BaBi_4Ti_4O_{15}$. Consequently, the addition of brownmillerite-like layers also seemed possible, e.g., $Bi_4Ti_3O_{12} + BaInO_{2.5} \rightarrow BaBi_4Ti_3InO_{14.5}$. From work on the brownmillerite-perovskite intergrowths, it was determined that the Ba-In-Ti and Ba-Sc-Ti systems could be easily prepared and readily formed a disordered solid solution between In and Ti or Sc and Ti. Thus $Bi_4Ti_3O_{12}$ was chosen as the starting Aurivillius phase, and $BaMO_{2.5}$ as the brownmillerite-like series.[1-3]

5.1 Non-oxygen-deficient Materials

Before investigating any of these new materials, several previously known Aurivillius phases were studied for comparison. $BaBi_2Nb_2O_9$ and $BaBi_4Ti_4O_{15}$ were prepared, and their conductivities were measured. $BaBi_4Ti_4O_{15}$ can be viewed as an Aurivillius-perovskite intergrowth: $Bi_4Ti_3O_{12} + BaTiO_3$. XRD patterns for both materials were consistent with previously reported data (JCPDS #40,355 and #35,757). A plot showing the conductivity as a function of 1000/T for both materials is shown in Figure 5.1. Both materials displayed linear behavior indicative of a single conduction mechanism. The activation energy of $BaBi_2Nb_2O_9$ was determined to be quite high, 1.5 eV, while that of $BaBi_4Ti_4O_{15}$ was substantially lower, 0.7 eV. The
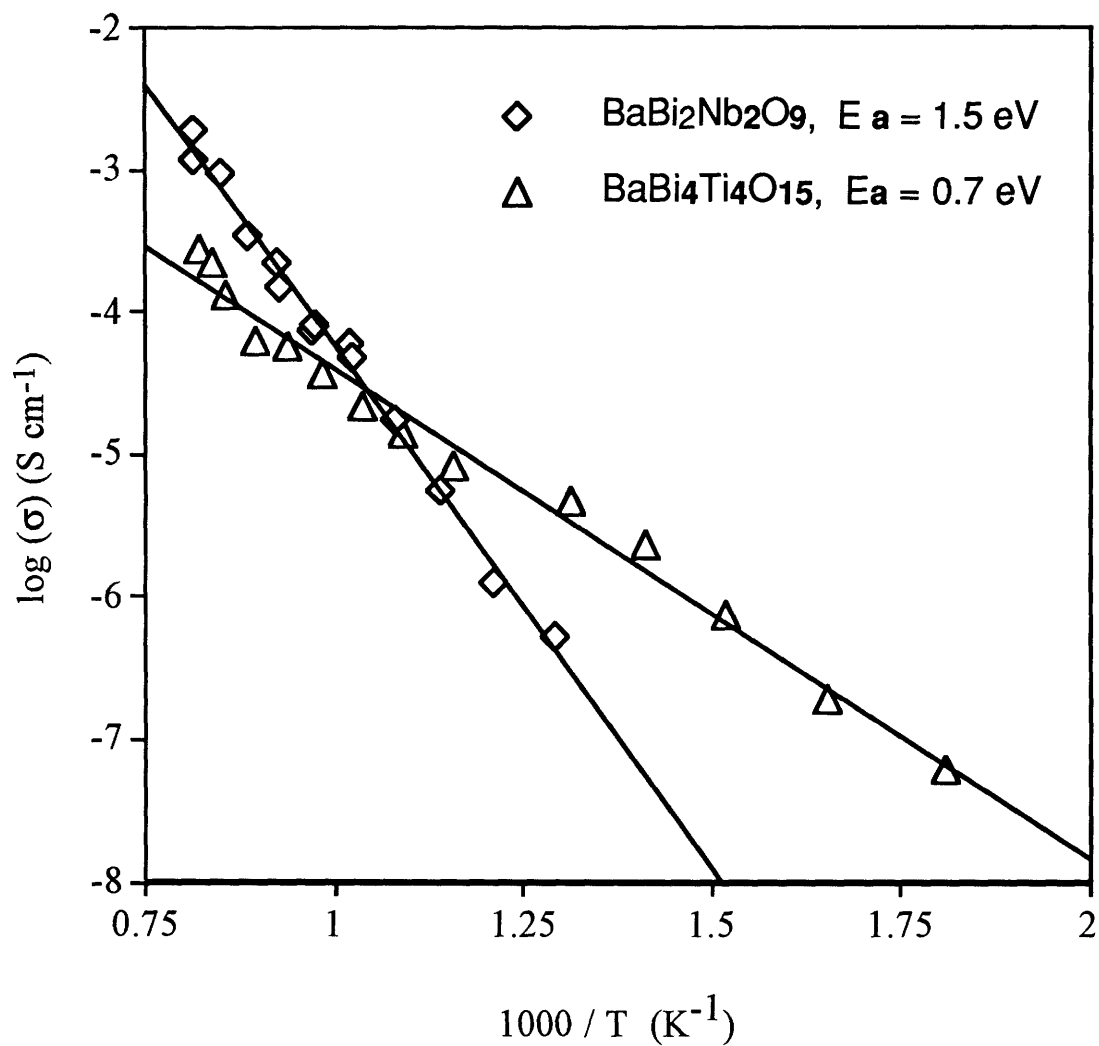
Figure 5.1 Log conductivity versus 1000/T for the non-oxygen deficient Aurivillius phases $BaBi_4Ti_4O_{15}$ and $BaBi_2Nb_2O_9$. These display linear Arrhenius behavior with high activation energies.

overall conductivities are rather low, less than 10^{-2} S cm^{-1} at 950 °C. A typical impedance plot is shown in Figure 5.2. This exhibits a large arc due to the bulk and grain boundary effects. At low frequencies, a small arc due to the electrode is observed. The small electrode resistance may indicate that there is substantial electronic conductivity in these samples. Since there are no vacancies, however, high oxygen conduction was not expected.

5.2 Oxygen Deficient Materials

5.2.1 Structural Characterization

$BaBi_4Ti_3ScO_{14.5}$, $BaBi_4Ti_3InO_{14.5}$, and $BaBi_4Ti_3GaO_{14.5}$, were prepared by solid state reactions and characterized by powder XRD. The powder XRD pattern of $BaBi_4Ti_3GaO_{14.5}$ is shown in Figure 5.3. The XRD patterns of $BaBi_4Ti_3ScO_{14.5}$ and $BaBi_4Ti_3InO_{14.5}$ are almost identical. These can all be indexed to a tetragonal unit cell which represents an additional ordering relative to $BaBi_4Ti_4O_{15}$, $a_M = \sqrt{2}a_{Ti}$, $b_M = \sqrt{2}b_{Ti}$, $c_M = c_{Ti}$. The lattice parameters for all three compounds are listed in Table 5.1 along with the lattice parameters of $BaBi_4Ti_4O_{15}$ indexed to the same cell. Table 5.2 lists the indexing of the powder XRD pattern for $BaBi_4Ti_3GaO_{14.5}$. There are many possible distortions to the idealized structure which could give rise to these lattice parameters including ordering of the oxygen vacancies or, alternatively, ordering of the B-cations in the perovskite layers. The peaks that result from in this extra ordering are very weak, suggesting that they are due to ordering of the oxygen vacancies rather than the B-cations. This is further supported by the fact that all peaks with greater than five percent relative intensity could be indexed to the simpler cell of the parent compound.
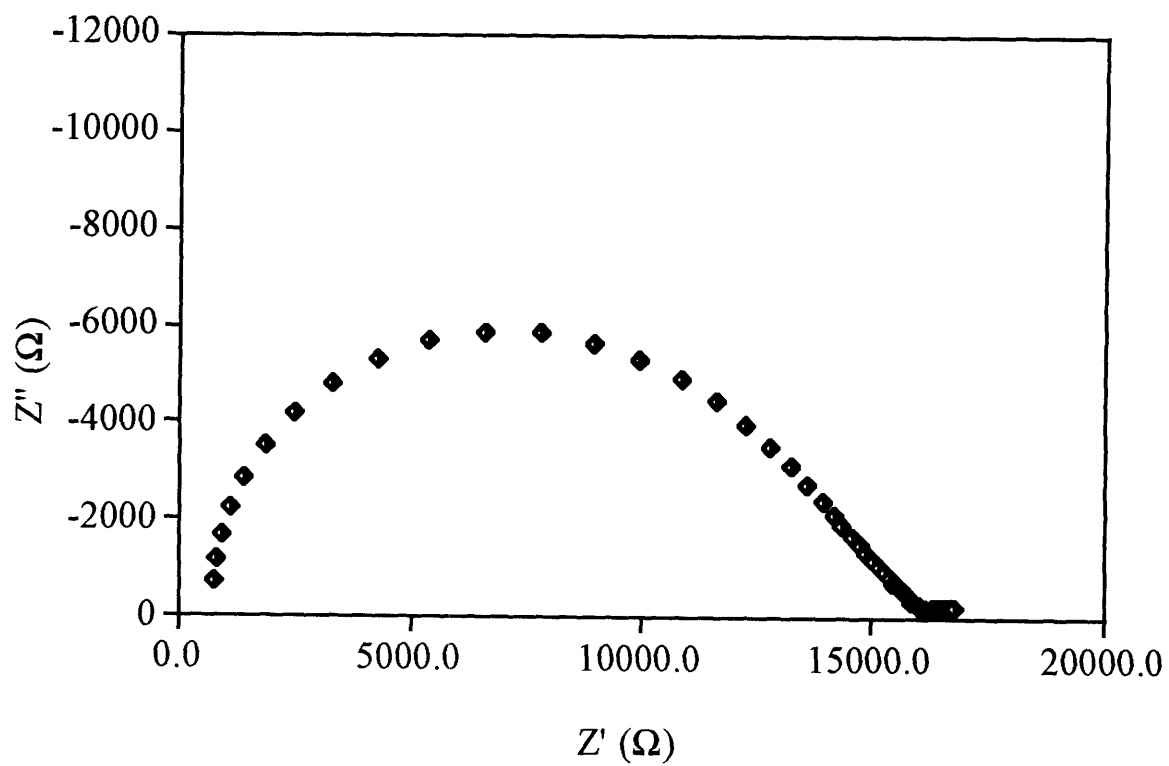
Figure 5.2 Cole-Cole plot for $BaBi_4Ti_4O_{15}$ at 750 °C showing a single arc for the bulk and grain boundary processes. The electrode arc is very small in this material.
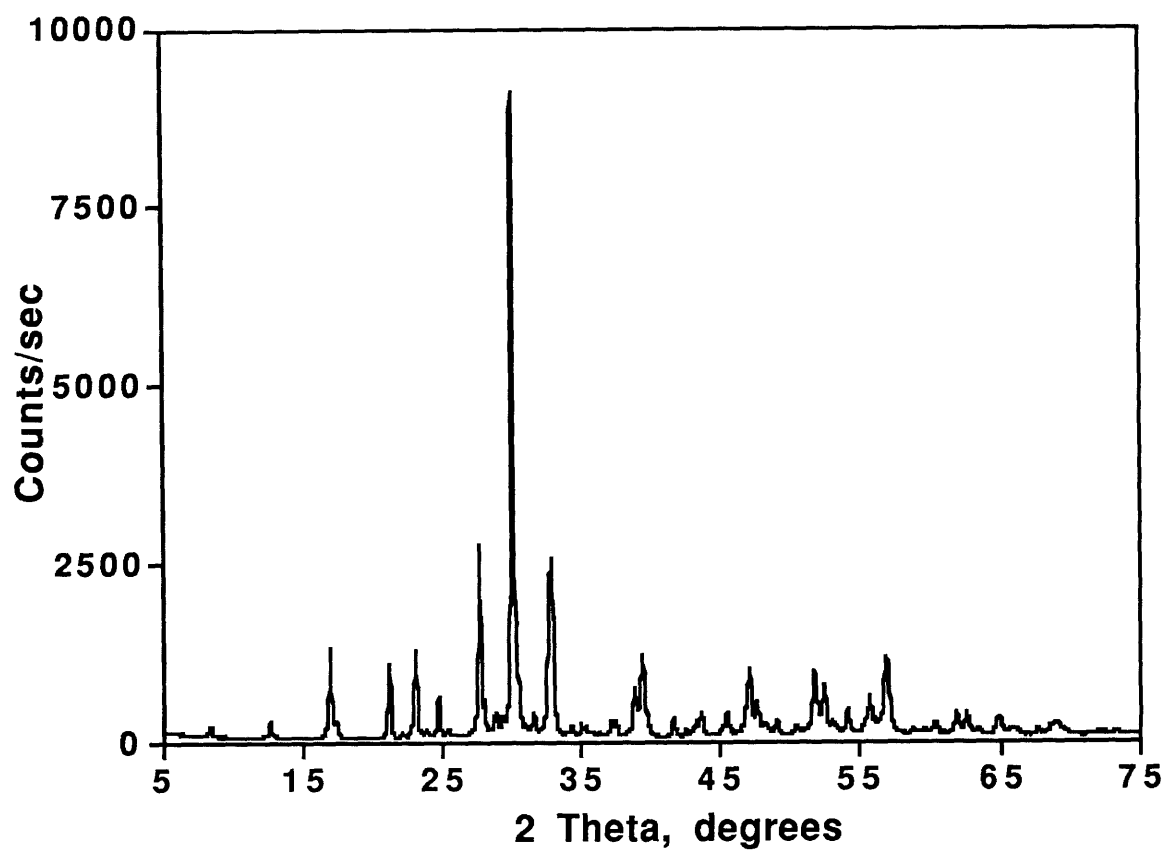
Figure 5.3 XRD pattern of $BaBi_4Ti_3GaO_{14.5}$.

Table 5.1 Lattice Parameters for Aurivillius-brownmillerite Intergrowths

Compound	a (Å)	c (Å)
$BaBi_4Ti_4O_{15}$*	5.462(3)*	41.85(1)
$BaBi_4Ti_3GaO_{14.5}$	5.449(3)	41.81(3)
$BaBi_4Ti_3InO_{14.5}$	5.663(4)	41.91(3)
$BaBi_4Ti_3ScO_{14.5}$	5.682(3)	41.74(3)

*The a parameter for $BaBi_4Ti_4O_{15}$ (3.862 Å) was multiplied by $\sqrt{2}$ for comparison.

Table 5.2 Indexed X-ray diffraction data for $BaBi_4Ti_4GaO_{14.5}$

h	k	l	d_{calc}	d_{obs}	I_{rel}
0	0	4	10.453	10.456	2
0	0	6	6.968	6.976	3
0	0	8	5.226	5.221	14
1	0	3	5.075	5.087	2
0	0	10	4.181	4.182	11
1	1	1	3.837	3.844	13
1	1	4	3.615	3.596	6
1	1	5	3.499	3.500	1
1	1	7	3.238	3.217	30
1	1	8	3.101	3.105	2
1	1	9	2.966	2.966	100
1	0	12	2.935	2.937	11
1	1	10	2.833	2.831	2
2	0	2	2.702	2.723	27
2	0	6	2.537	2.543	1
2	1	3	2.400	2.397	2
0	0	18	2.323	2.320	7
2	0	10	2.283	2.286	12
1	1	15	2.258	2.258	1
2	1	9	2.158	2.168	3
0	0	20	2.091	2.092	2
0	2	13	2.079	2.075	3
1	2	12	1.997	1.994	3
2	2	0	1.927	1.930	9
1	1	19	1.911	1.911	4
0	0	24	1.742	1.744	7
1	1	23	1.644	1.640	1
3	0	12	1.611	1.619	10
1	1	25	1.534	1.533	2
3	1	14	1.493	1.499	3
1	1	26	1.484	1.483	3
1	3	16	1.439	1.437	3
0	4	0	1.362	1.366	2
0	1	34	1.200	1.198	1
2	0	32	1.178	1.179	1
0	3	28	1.153	1.152	1

5.2.2 Conductivity Measurements

Impedance plots for $BaBi_4Ti_3InO_{14.5}$ at low (675 °C) and high (825 °C) temperatures are shown in Figures 5.4 and 5.5. The low temperature plot displays a single arc for bulk and grain boundary effects and a somewhat smaller arc for the electrode. At higher temperatures the conductivity is so high that the sample arc cannot be observed, but the resistance can still be determined from the intercept of the electrode arc. $BaBi_4Ti_3ScO_{14.5}$ and $BaBi_4Ti_3GaO_{14.5}$ behaved similarly.

The results of the conductivity measurements on these samples were very interesting. An Arrhenius plot of conductivity for $BaBi_4Ti_3InO_{14.5}$ is shown in Figure 5.6. It exhibits a region of low conductivity and high activation energy (0.95 eV) at low temperatures, a jump in conductivity of almost two orders of magnitude near 800 °C, followed by a region of high conductivity and low activation energy at high temperatures. The conductivity in the high temperature regime is about 10^{-1} S cm^{-1} with a low activation energy of 0.35 eV. This transition is observed both on heating and cooling. Conductivity jumps such as this are typical for samples which undergo order-disorder transitions.[4]

An Arrhenius plot of conductivity for $BaBi_4Ti_3ScO_{14.5}$ is shown in Figure 5.7. This displays a similar jump in conductivity, but for this sample a hysteresis is observed between the heating and cooling cycles. Low temperature conductivities and activation energy (1.01 eV) in this sample are similar to those observed for $BaBi_4Ti_3InO_{14.5}$. The high temperature conductivities are also similar; however, the activation energy, as calculated from this data, is somewhat higher (0.49 eV). It is not clear, however, that the activation energy is actually higher. Assuming this transition is very slow,
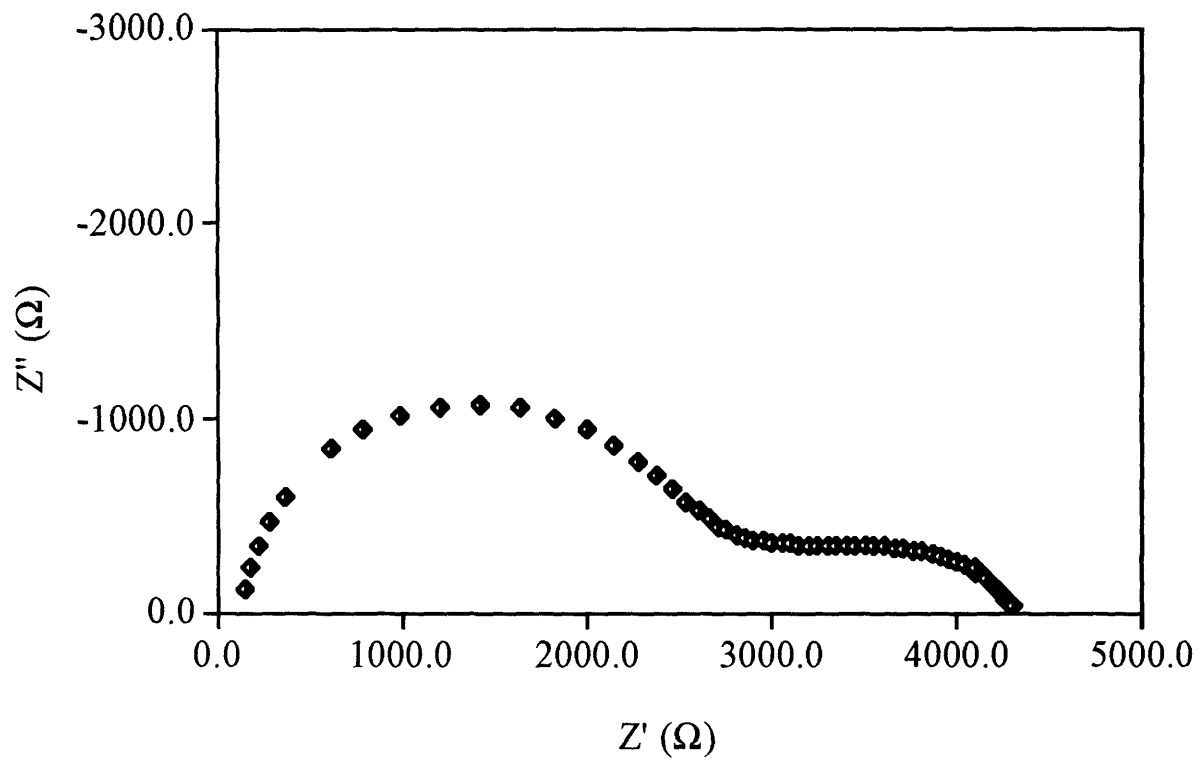
Figure 5.4 The Cole-Cole plot for $BaBi_4Ti_3InO_{14.5}$ at 675 °C displays a single arc for bulk and grain boundary processes and a wide arc for the electrode.
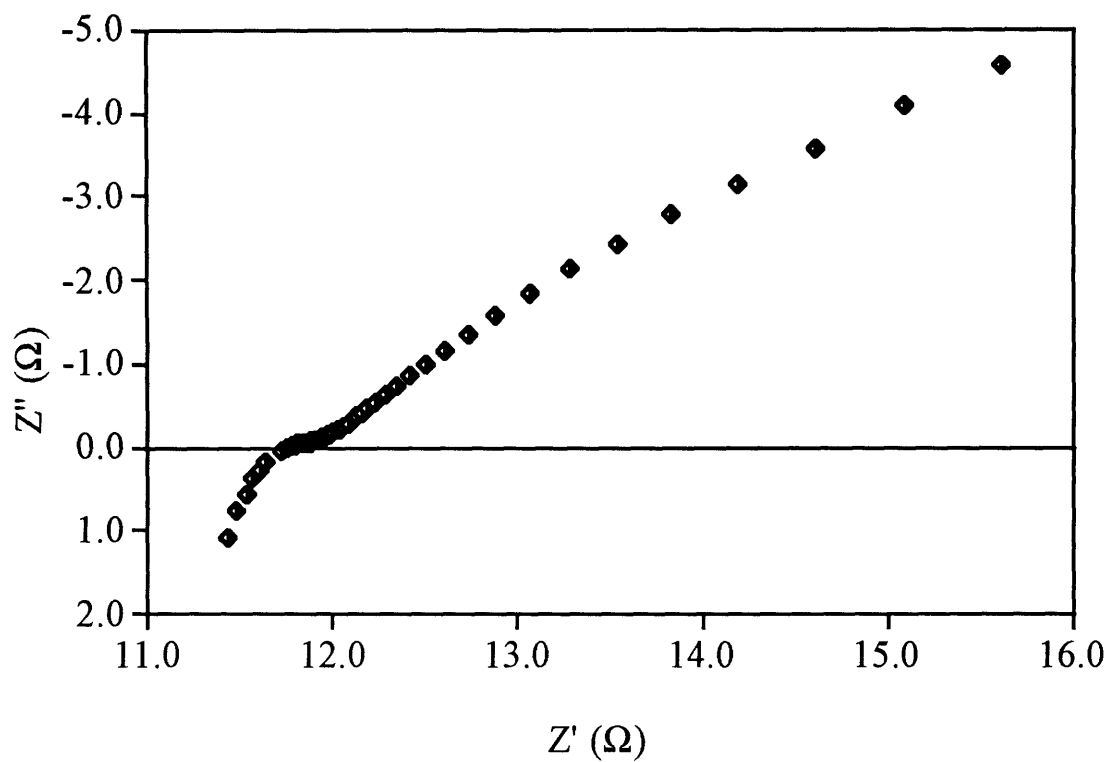
Figure 5.5 The Cole-Cole plot for $BaBi_4Ti_3InO_{14.5}$ at 825 °C contains part of the bulk arc, but predominantly consists of the electrode arc.
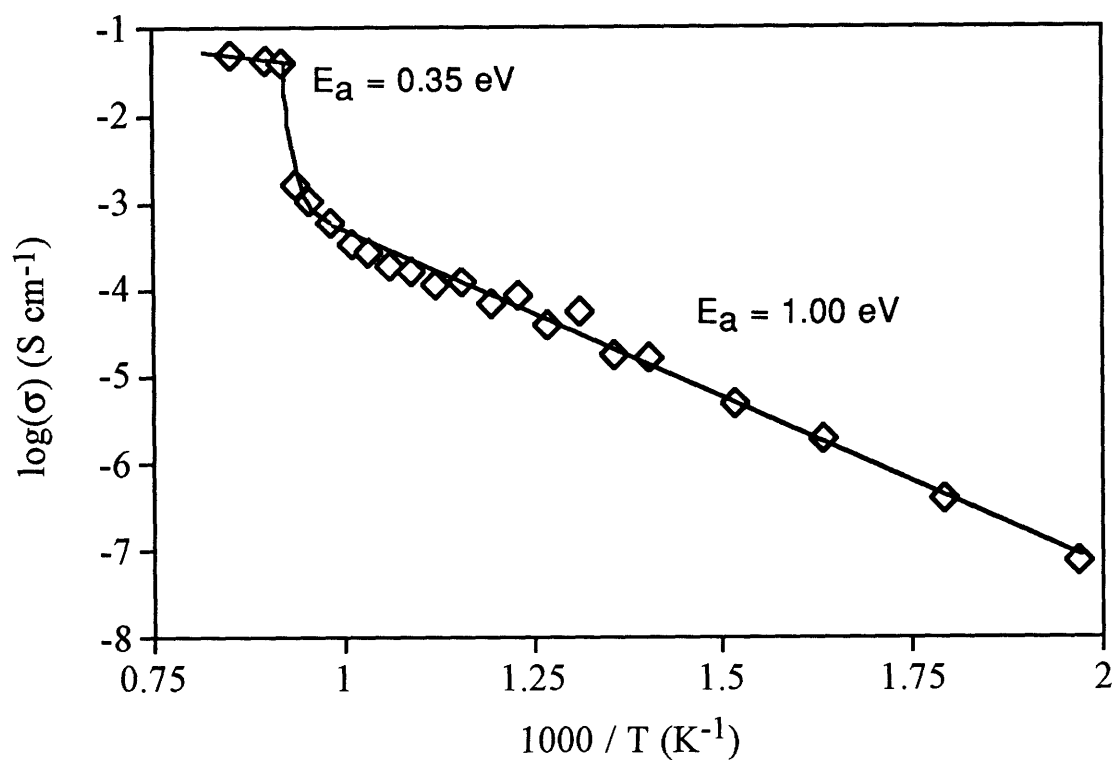
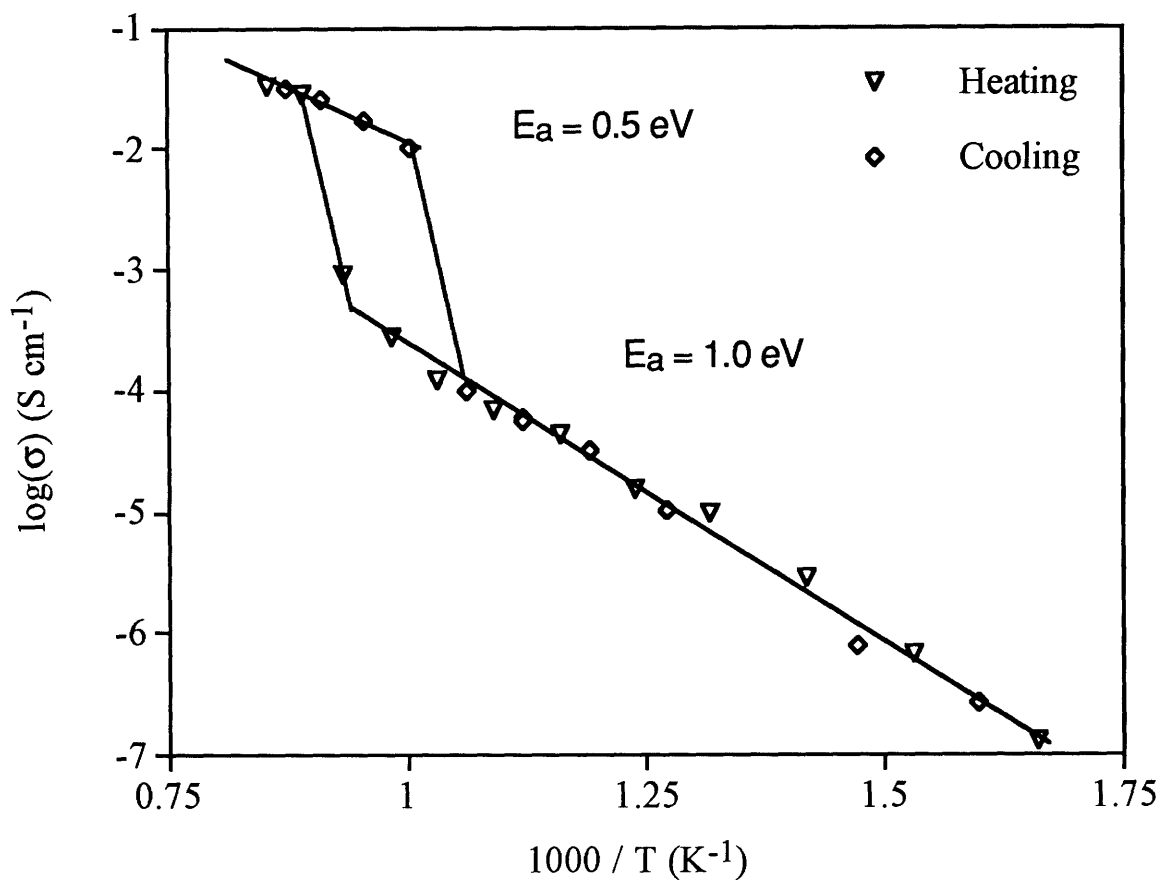Figure 5.6 Arrhenius plot conductivity for $BaBi_4Ti_3InO_{14.5}$ displaying a jump in the conductivity near 800 °C.

Figure 5.7 Log conductivity versus 1000/T for $BaBi_4Ti_3ScO_{14.5}$ displaying a jump in conductivity. A hysteresis is observed between heating and cooling.

some of the points may be taken while the sample has not fully converted to the high temperature phase. Further studies on this sample confirmed that the phase transition is in fact slow. A sample left at 725 °C for one week eventually relaxed to the low temperature phase. Considering a slow phase transition such as this one, it seemed likely that the high conductivity could be retained if the sample were quenched. Cooling the sample from 800 °C by opening the furnace and allowing the sample to cool rapidly did not accomplish this however. The sample still showed low conductivity at 300 to 400 °C. It is not fully clear from this procedure whether the sample ordered too rapidly at low temperatures to be quenched in the disordered state or whether the barriers for conduction at low temperatures are so high that the disordered structure does not give rise to high conductivity.

An Arrhenius plot of conductivity for the third sample, $BaBi_4Ti_3GaO_{14.5}$, is shown in Figure 5.8. It exhibits a less abrupt transition than the previous two samples when measurements are taken at the same rate (three to four points per day at 50 degree intervals). When measured at a slower rate (two points per day at 50 degree intervals), the curvature in this plot is lessened. This is shown in Figure 5.9 and indicates that the disordering process in these materials on heating may also be slow. Based on the information from Figure 5.9, it is also possible that there is a third conductivity process at lower temperatures; however, too few points were collected to prove or disprove this possibility. Alternatively, this might be low temperature protonic conduction as shown for the brownmillerite-perovskite materials in Chapter 4 or possibly another low temperature phase transition, as seen in $Bi_4V_2O_{11}$.[5]
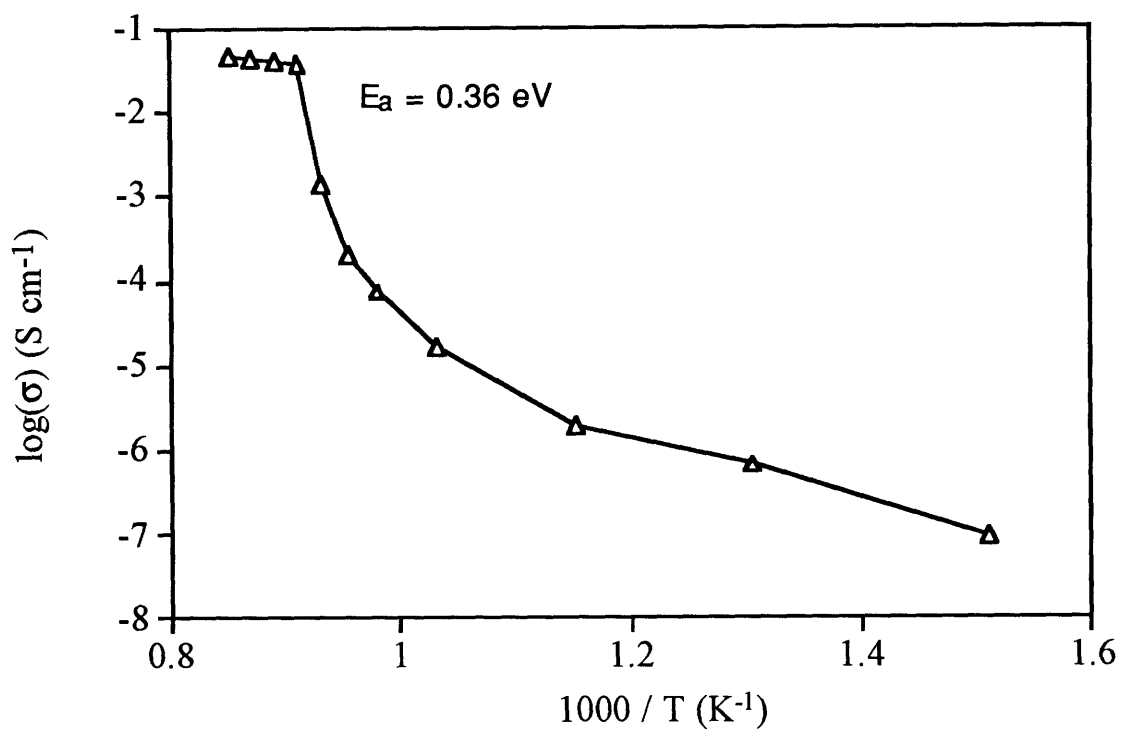
Figure 5.8 Log conductivity versus 1000/T for $BaBi_4Ti_3GaO_{14.5}$ taken with 6 to 8 hour equilibration times displaying significant curvature.

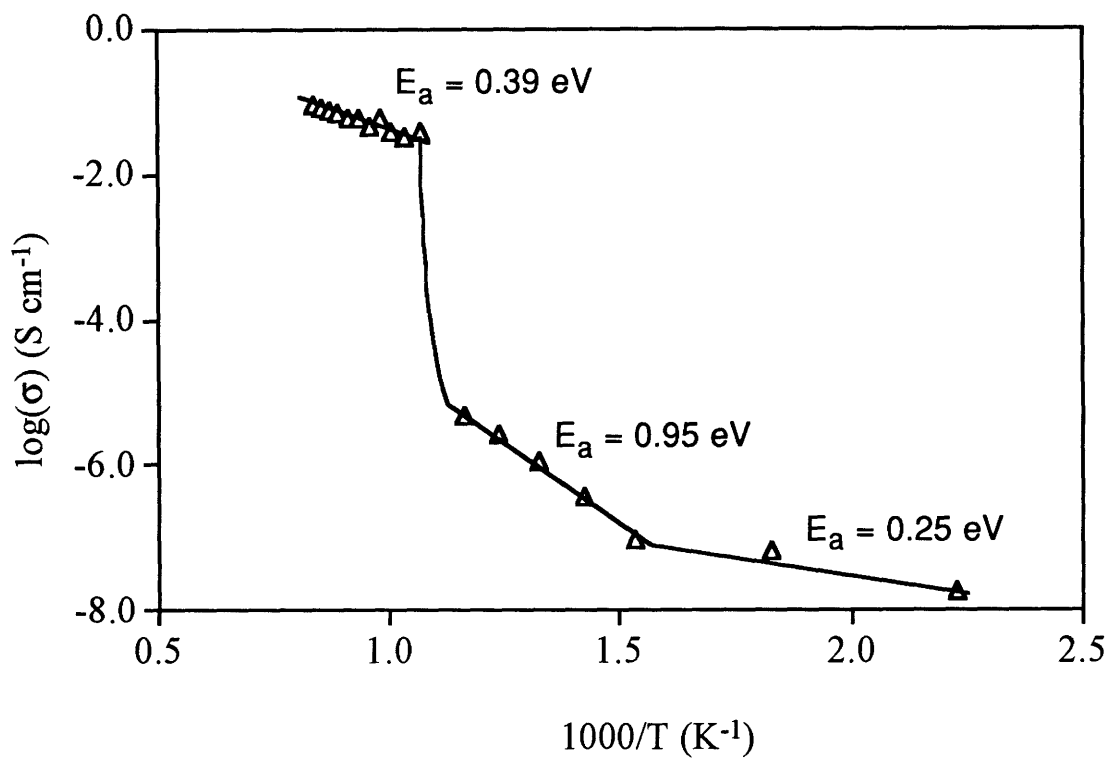Figure 5.9 Arrhenius plot of conductivity for $BaBi_4Ti_3GaO_{14.5}$ taken with 12 hour equilibration times. The curvature in the plot is reduced from that shown in Figure 5.8, but more than two conductivity regions are still present.

5.2.3 Differential Thermal Analysis

Differential Thermal Analysis was used to investigate these phase transitions. Figure 5.10 shows a DTA plot for $BaBi_4Ti_3InO_{14.5}$. This exhibits a phase transition above 800 °C. All three samples display similar DTA behavior. No transition is observed on cooling, but based on the conductivity data, abrupt transitions would not be expected on the time scale of DTA runs (30 minutes). These transitions are relatively weak in the DTA on heating, and if less abrupt on cooling, might be too small to notice. The same sample can be cycled through the DTA multiple times, and in this case, the later signals are decreased relative to the first run. This could indicate that the sample does not fully re-order on the short time scale of a DTA run. In the case of the $BaBi_4Ti_3GaO_{14.5}$ no second phase transition was observed at low temperatures, suggesting that the change in conductivity at low temperatures is most likely not due to a phase change, but rather a change in the conduction process. The simultaneous TGA measurement showed no detectable weight loss below 1100 °C for any of the samples confirming that the observed order-disorder transitions are an intrinsic property rather than externally induced by oxygen loss.

5.2.4 Conductivity as a Function of Oxygen Partial Pressure

A plot of log conductivity at 700 °C versus log p_{O_2} for $BaBi_4Ti_3GaO_{14.5}$ is shown in Figure 5.11. This displays no dependence on oxygen partial pressure to 10^{-18} atm O_2. Below this value the sample apparently decomposes as the conductivity change was not reversible. No conductivity increase was observed when the decomposed sample was re-exposed to oxygen. On removal from the sample holder, the pellet had flattened and densified. The
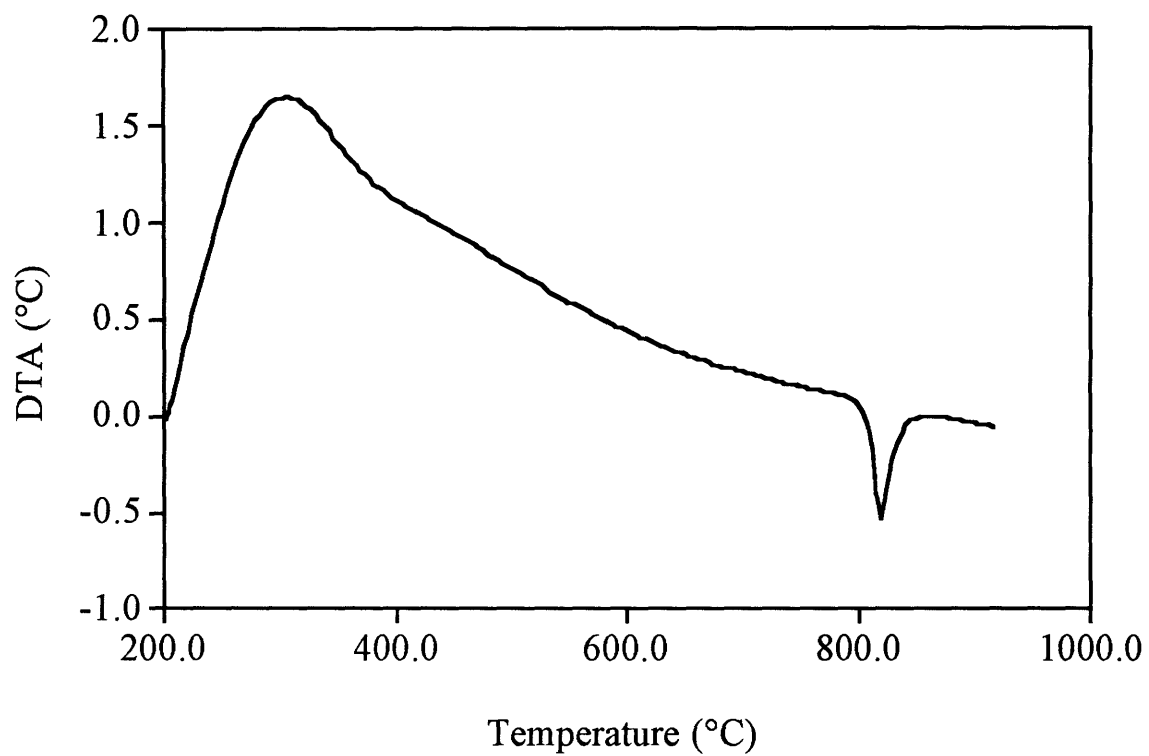
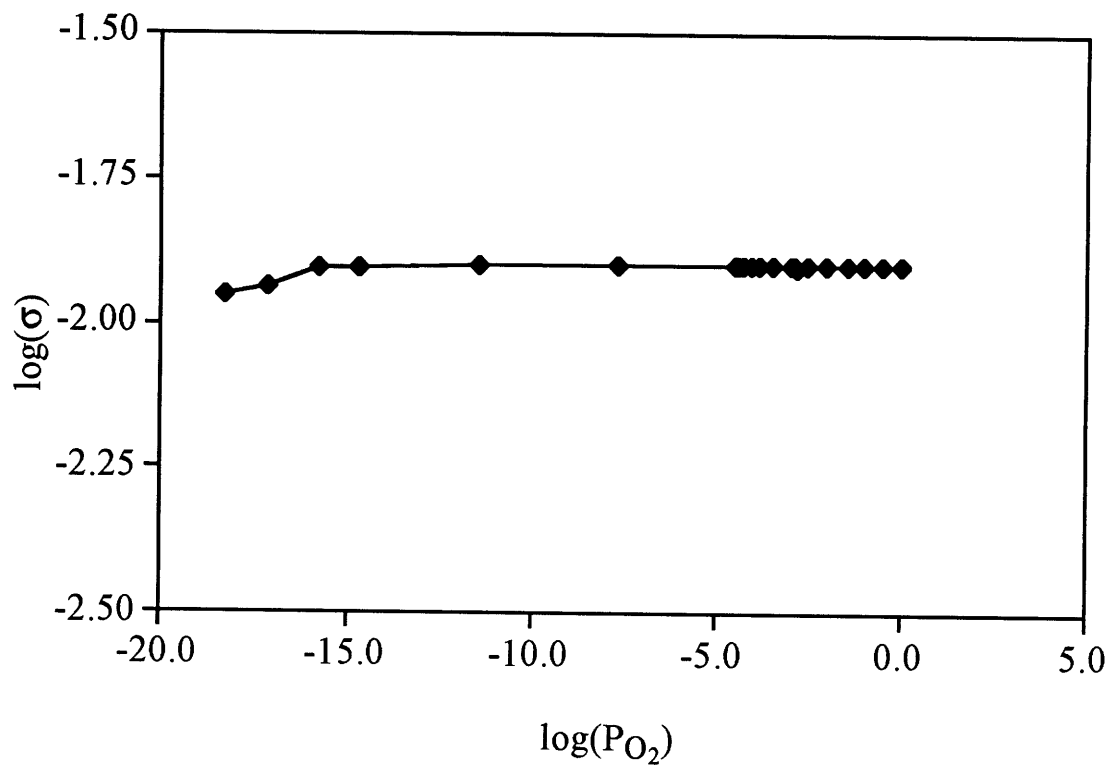Figure 5.10 DTA plot of $BaBi_4Ti_3GaO_{14.5}$ displaying a transition above 800 °C.

Figure 5.11 Log conductivity at 700 °C versus log p_{O_2} for $BaBi_4Ti_3GaO_{14.5}$.

The conductivity remains constant down to 10^{-17} atm. At lower p_{O_2} sample decomposition is observed.

electrodes were significantly attacked, but there was no evidence of bismuth metal. This result indicates that the sample has an unusually high tolerance to reduction, considering that it contain bismuth. The lack of dependence on oxygen partial pressure indicates that the conductivity is predominantly ionic over a wide range of oxygen partial pressures which is important for some applications.

5.2.5 Measurement of Transference Numbers using a Concentration Cell

A concentration cell was constructed in a manner similar to that of the oxygen sensors. A sample of $BaBi_4Ti_3GaO_{14.5}$ was sealed between two mullite tubes using light pressure at 800 °C. Air was used for the reference electrode, while oxygen and mixtures of oxygen in argon were used at the other electrode. The pellet had a thickness of approximately 5 mm, which is actually thicker than desired for such a measurement. However, this thickness minimizes oxygen diffusion through pores in the pellet. The transference numbers were calculated by measuring the oxygen content using the zirconia sensors and calculating the voltage expected at the sample temperature for each oxygen pressure. The transference number is simply the ratio between the observed and expected voltages, as any electronic conductivity present in the sample reduces the voltage. At 800 °C all measurements indicated transference numbers greater than 0.90. The data are shown in Figure 5.12. In Figure 5.12 it appears that the transference number decreases with oxygen concentration; however, the observed voltages fluctuated, so associated error bars are shown in Figure 5.13 to represent the confidence interval of each measurement. The large error bars for 0.5 atm p_{O_2} are due to limitations in the accuracy of the voltmeter in measuring very low voltage. It is, therefore, likely that the transference number here is
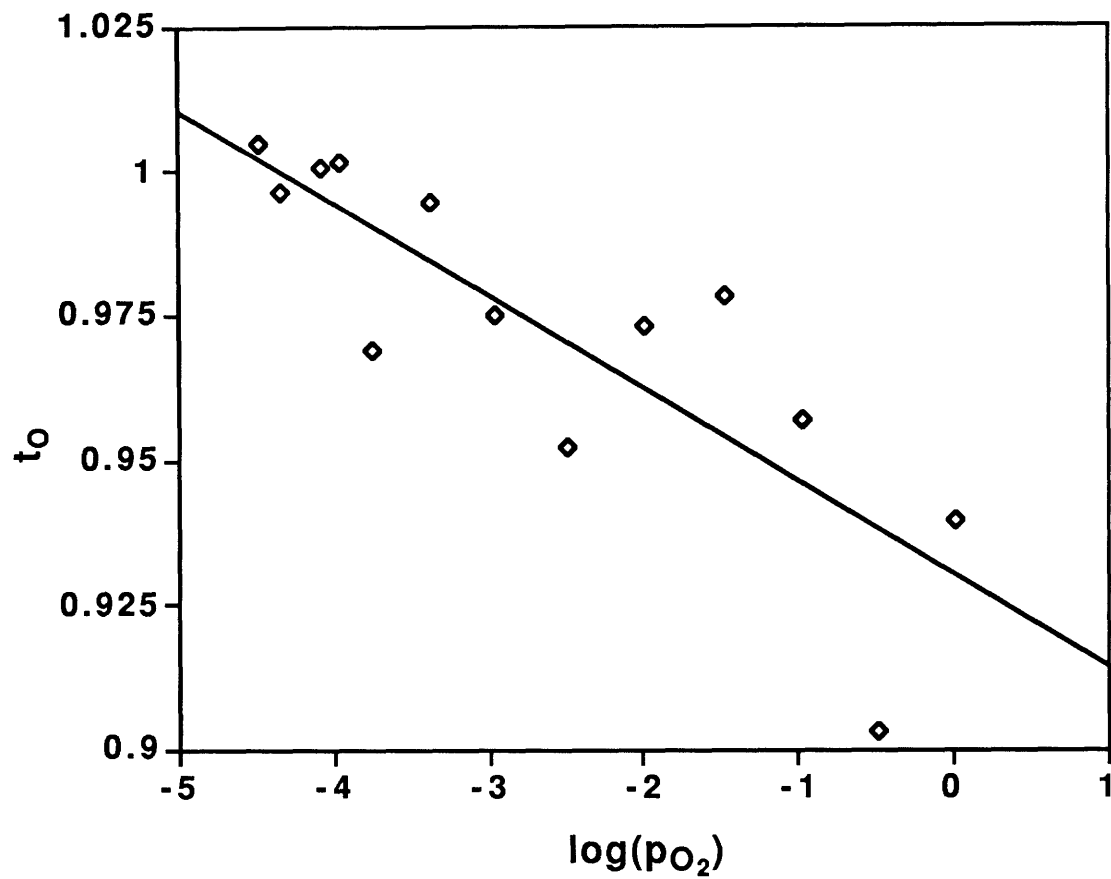
Figure 5.12 Transference numbers for $BaBi_4Ti_3GaO_{14.5}$ as a function of oxygen partial pressure at 800 °C. This data displays an apparent decrease in transference numbers at higher oxygen partial pressures.
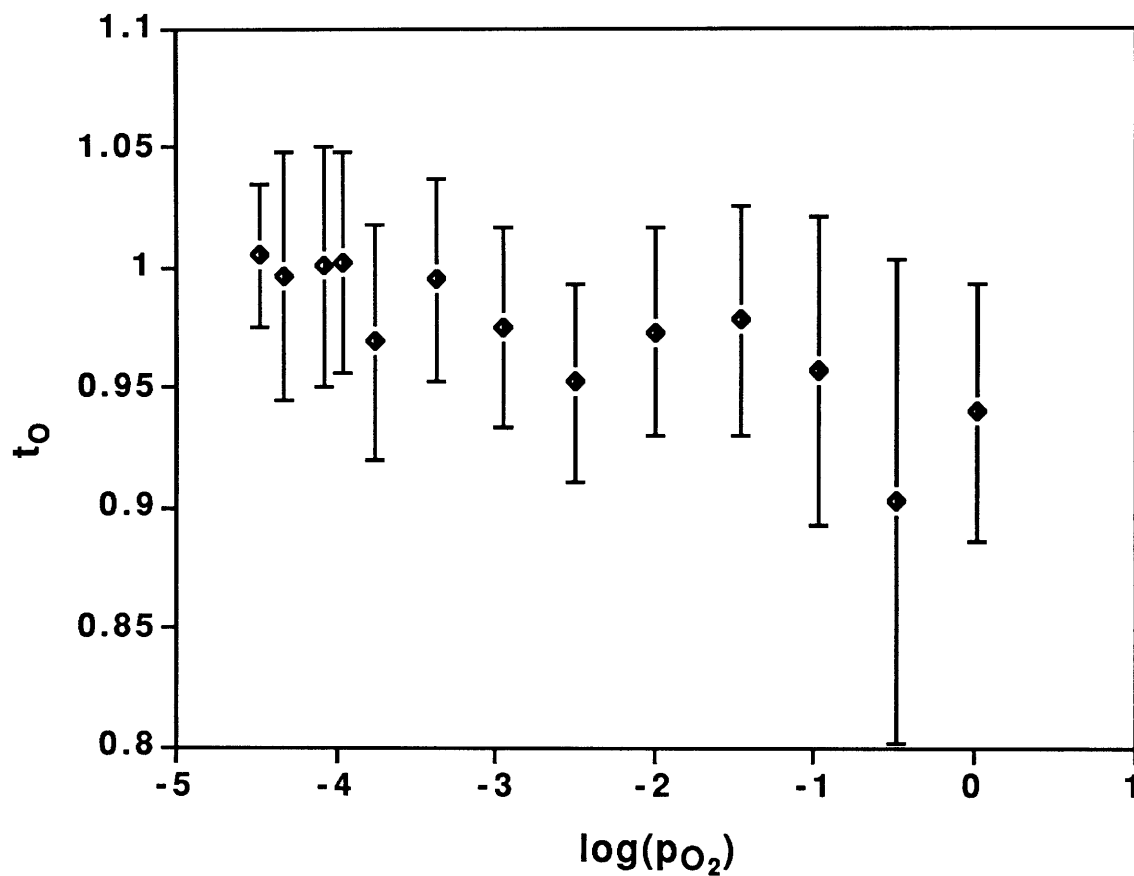
Figure 5.13 Transference numbers for $BaBi_4Ti_3GaO_{14.5}$ at 800 °C as a function of oxygen partial pressure showing error bars. The wide error bars indicate that while the transference number is generally high, and trends may be present, it is difficult to draw firm conclusions about any trends.

actually closer to 0.95. At lower oxygen partial pressures, the calculated transference number is sometimes greater than unity. Since the error bars extend below one, it is possible that this is simply within the error of the measurement, but it is also possible that this material has a higher transference number than the YSZ sensors. The observed decrease in transference number would, however, be consistent with the observation that $CaTiO_3$ displayed ideal oxygen ion conduction under fuel cell conditions (high oxygen gradients) but not under atmospheric conditions.[6] Due to the thickness of the sample, the large resistance made it difficult to take measurements at lower temperatures, but at low p_{O_2} (5×10^{-6} atm) the voltage was large enough to compensate. At 650 °C and p_{O_2} of 5×10^{-6} atm a transference number of 0.85 was obtained. This indicates that there is some electronic conductivity present in the low temperature, ordered region, but the conductivity is still largely ionic.

5.3 Conclusions

These materials display transitions in plots of oxygen ion conductivity versus reciprocal temperature which are consistent with a phase transition in the materials. Above the transition temperature the conductivity is high enough to be used in many applications. Few materials with such high conductivity possess the same stability to the range of oxygen partial pressures exhibited by $BaBi_4Ti_3GaO_{14.5}$. The high transference numbers observed in the concentration cell indicate that this material may have some possible uses in devices.

Based on the transitions observed in these materials, it seems likely that at low temperatures the oxygen vacancies order or that a large attraction exists between the trivalent cation and the oxygen vacancies. Such an

interaction should result in an increase in the activation energy and a decrease in the conductivity, which is observed. At higher temperatures the interaction between the trivalent cations and vacancies can be readily overcome by the entropy of the system, leading to some degree of disorder in the oxygen vacancies. Thus, extremely low activation energies are observed and conductivities are high.

5.4 Future Work

Several other composition in this series seem possible, although many have already been tried unsuccessfully. The addition of a second brownmillerite layer to these materials, for instance, was not successful in initial attempts, although different heating cycles or starting from ternary rather than binary oxides might give different results. Substitution of strontium for barium yielded a mixture of the three layer phase, $Bi_4Ti_3O_{12}$, and a five layer phase, presumably $Sr_2Bi_4Ti_3Ga_2O_{17}$. In the non-oxygen deficient Aurivillius compounds several Sr-Bi-Ti-O phases are known to exist. $SrBi_4Ti_4O_{15}$, $Sr_2Bi_4Ti_5O_{18}$, and $SrBi_8Ti_7O_{27}$, have all been previously prepared; and it, therefore seems likely that several phases might be prepared in the Sr-Bi-Ti-Ga-O system if the proper conditions are found.

In this work, the use of transition metal ions with multiple oxidation states was avoided, but the addition of such ions can create a system which has mixed electronic/ionic conductivity. Such a material could be as for an electrode material in various devices or for catalysis.

In order for these materials to be of commercial use, different preparation techniques such as solution or sol-gel precursor methods need to be investigated. These methods allow the fabrication of samples of different shapes and generally greater densities. The use of such precursors might also

facilitate the preparation of some of the compounds which could not be successfully prepared by solid state reaction. Once such methods are worked out, the material should be tested for viability in devices or application in catalysis.

References

(1)   Kendall, K. R.; Thomas, J. K.; zur Loye, H.-C., Oxygen Ion Conductivity in a New Class of Layered Bismuth Oxides, (1994) **in press**.

(2)   Thomas, J. K.; Anderson, M. E.; Krause, W. E.; zur Loye, H.-C., In *Solid State Ionics III*; J.-M. T. G.-A. Nazri M. Armand, Ed.; "Oxygen Ion Conductivity in a New Class of Layered Bismuth Oxide Compounds", Materials Research Society: Pittsburgh, Pennsylvania, 1993, Vol. 293; pp 295-300.

(3)   Thomas, J. K.; Kendall, K. R.; zur Loye, H.-C., Oxygen Ion Conductivity in a New Class of Layered Bismuth Oxide Materials, (1994) **in press**.

(4)   Dell, R. M.; Hooper, A., In *Solid Electrolytes*; P. Hagenmuller and W. van Gool, Ed.; "Oxygen Ion Conductors", Academic Press: New York, 1978; pp 291-312.

(5)   Mairesse, In *Fast Ion Transport in Solids*; B. Scrosati, Ed.; "Bismuth-based Oxide Conductors: Novel Structure and Electrical Features", Kluwer: The Netherlands, 1993; pp 271-290.

(6)   Iwahara, H., Oxide-ionic and Protonic Conductors based on Perovskite-type Oxides and Their Possible Applications, **Solid State Ionics** (1992) **52**, 99-104.